Supporting information

Deep-red photoluminescent mechanoresponsive polymers with dynamic Cu^I-arylamide mechanophores

Tatiana Gridneva,[a] Ayumu Karimata,[a] Richa Bansal,[a] Robert R. Fayzullin,[b] Serhii Vasylevskyi
Andrew Bruhacs,[a] and Julia R. Khusnutdinova*[a]

[a]Okinawa Institute of Science and Technology Graduate University, Coordination Chemistry and Catalysis Unit, 1919-1 Tancha, Onna-son, Okinawa, Japan, 904-0495

[b]Arbuzov Institute of Organic and Physical Chemistry, FCR Kazan Scientific Center, Russian Academy of Sciences, 8 Arbuzov Street, Kazan 420088, Russian Federation

Email : juliak@oist.jp

Table of Contents

I. General Specifications

Materials. All reactions were performed using nitrogen or argon glovebox unless stated otherwise. All reactions and measurements were performed at room temperature unless stated otherwise. Anhydrous solvents were dispensed from an MBRAUN solvent purification system. Unless noted otherwise, all chemicals and deuterated solvents were purchased from major commercial suppliers (TCI, Sigma-Aldrich, and Nacalai Tesque) and used without further purification.

Compound **11**, **12**, **13** and **L2** were prepared by methods based on the previous report[1] with modifications (see below). The compounds were characterized by ^{1}H NMR spectroscopy, and the chemical shifts were found to be consistent with the reported values.

NMR spectroscopy. NMR spectra were measured on JEOL ECZ400S 400MHz or JEOL ECZ600R 600 MHz. The following abbreviations are used for describing NMR spectra: s (singlet), d (doublet), t (triplet), dd (doublet of doublets), m (multiplet), br (broad peak).

FT-IR spectroscopy. FT-IR spectra were measured using an Agilent Cary 630 with an ATR module in an argon-filled glovebox.

Photophysical properties. UV-vis spectra were recorded on an Agilent Cary 60 spectrophotometer. Photoluminescence spectra and photoluminescence quantum yields (PLQYs) were recorded by Hamamatsu Quantaurus-QY Plus (excitation wavelength is 380 nm). The polystyrene (PS) films containing 1 wt% of physically-blended Cu complexes **1**-**6** were prepared in a glovebox by dissolving 99 mg of PMMA (Aldrich, average Mw ~350,000 by GPC) in around 5 mL of DCM, then adding 1 mg of the complexes, stirring to form a uniform mixture and slowly evaporating the solvent, followed by drying under vacuum for 1 day. For PLQY measurements, a solid sample placed on a quartz dish was purged with nitrogen gas for 30 minutes and measured under nitrogen gas flow inside an integrating sphere. The photoluminescence lifetime measurements were conducted using a second harmonic excitation source with a wavelength of 380 nm, generated by a tunable Spectra Physics Mai Tai mode-locked Ti-Sapphire femtosecond pulsed laser oscillator. The pulse repetition rate was set to 20-50 kHz, allowing sufficient time for the luminescence signal to decay to background levels. Furthermore, a high-pass optical filter was employed to prevent any fundamental 760 nm pump leakage from entering the excitation path. Data acquisition was performed using a Hamamatsu Photonics Streak scope camera, which had a sweep time of 10-50 microseconds (adjusted for each sample individually). The camera was coupled with a Czerny-Turner type Princeton Instruments spectrometer featuring a grating with a blazing angle of 500 nm and a groove density of 40 gr/mm. This configuration allowed for both time- and spectrally resolved data acquisition. Fitting curves of emission decay were obtained as single exponential or biexponential fits, and for biexponential fits the emission lifetimes were obtained as intensity-weighted average estimated by $(A_1\tau_1^2 + A_2\tau_2^2)/(A_1\tau_1 + A_2\tau_2)$.

Powder X-ray diffraction analysis. The powder X-ray diffraction studies were performed on an automated Bruker D8 Discover diffractometer equipped with an EIGER R 500K detector. The CuKα1 radiation was used. All experiments were carried out at room temperature (293(2) K). Before measurements, crystals were carefully ground. Samples were placed in an airtight low background holder. Patterns were recorded in the 2θ range starting from 6°, in 0.015° steps, with an exposure time of 0.50 s. Simulated PXRD patterns were obtained by Mercury (version 3.8) using structural models based on single-crystal XRD data collected at low temperatures.

Transmittance analysis. A CRAIC 20/30 PV micro-confocal spectrophotometer was utilized to collect transmission data on the crystalline samples κ^3-**4** and κ^4-**4** in the UV and visible ranges, using a diffuse Xe light source. The κ^4-**4** sample was examined with a 40x objective (Zeiss Ultrafluar NA=0.6) with an integration time of 8 ms for the UV/VIS spectrometer, averaging over 15 spectra. The κ^3-**4** sample showed optimal results under a 10x objective (Zeiss Ultrafuar NA=0.2) with an integration time of 8 ms, averaging over 200 spectra.

Luminescence imaging during film stretching. All stretching tests were performed inside an argon glove box using a compact uniaxial tensile testing machine manufactured by Acroedge Co. Strain is defined as $100 \times (L - L_0)/L_0$ (L_0 is initial length) Photoluminescence spectra of the films during stretching were obtained by monitoring emission of the central area of the film using a Reflection/Backscattering Probe R600-7 and recorded by a QE-Pro 6200 spectrometer manufactured by Ocean optics Co. The photographs and movies of luminescence imaging were taken by a CCD camera manufactured by Thorlabs equipped with a 400 nm long pass filter. The photographs and movies were analyzed by the free software Image J.[2] The supplementary video shows the emission intensity change on the first 10 cycles of continuous stretching and releasing of film **PBA1** out of 30 cycles shown in Figure 4 of the main paper. The image is shown in pseudocolor based on grayscale pixel intensity. Excitation = 365 nm, speed of stretching = 10 mm per second, camera : 4.5 fps, speed of video = $\times 1$.

Mechanical properties. All tensile tests were performed inside an argon glove box. Films of the size 25 mm [L] × 10 mm [W] × 1.5 mm [T] were used. Strain-Stress curves were recorded with a compact uniaxial tensile testing machine manufactured by Acroedge Co with speed of 10 mm per second. Stress and strain at break were estimated as an average of measurements of 4 samples. Strain was defined as $100 \times (L - L_0)/L_0$ (L_0 is initial length) and stress (MPa) was calculated as dividing load (N) with cross-section area of the film.

Cyclic voltammetry. Cyclic voltammetry was performed inside glovebox, using ALS/CHI 660E electrochemical analyzer. 0.3 M solution of $^nBu_4NBF_4$ as a supporting electrolyte in anhydrous THF was used. Pt disk electrode (d = 1.6 mm) as the working electrode, a platinum wire as the auxiliary electrode, and non-aqueous silver wire reference electrode assembly filled with a 0.01 M AgNO$_3$/0.1 M /MeCN solution were used. All potentials were referenced against ferrocene (Fc/Fc$^+$).
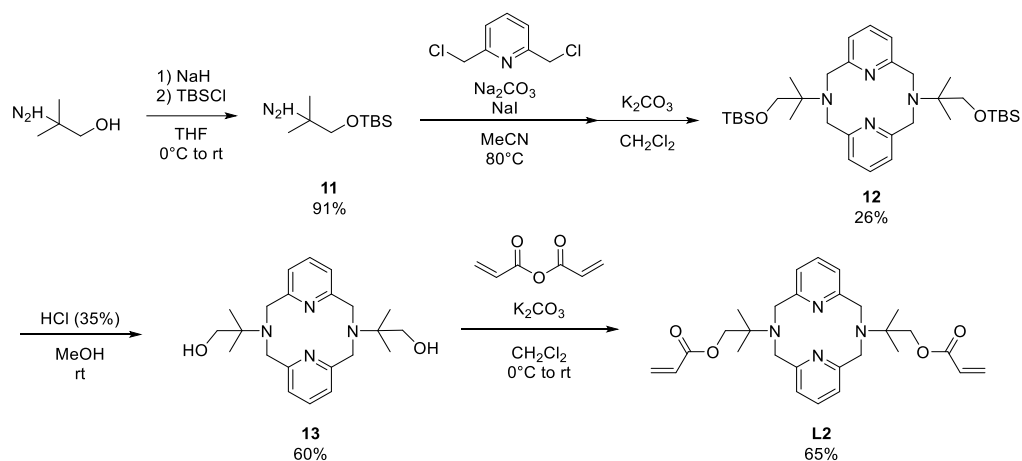
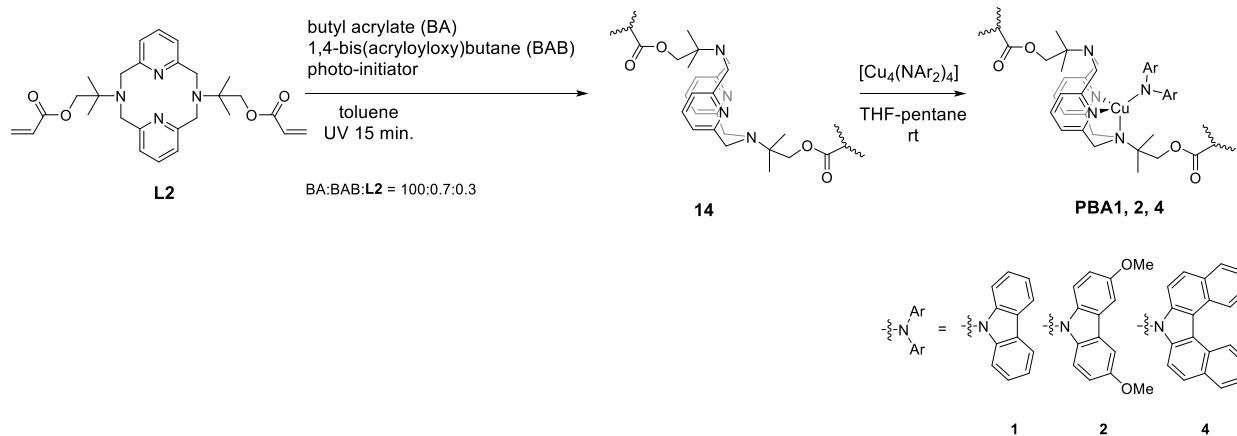## II. Synthesis of ligands, metal complexes and polymers
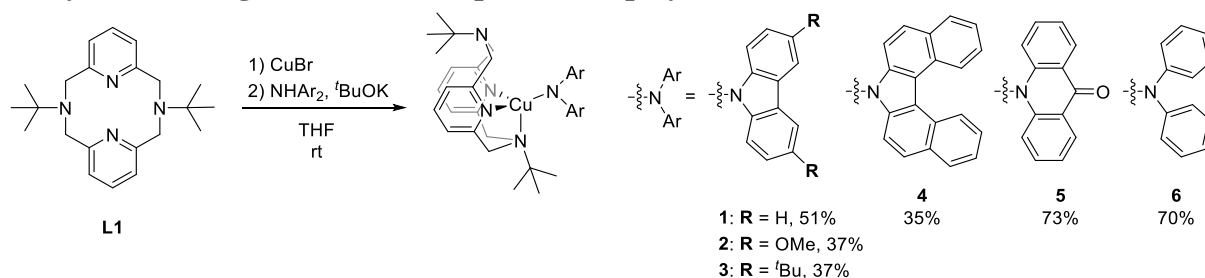
Scheme S1. Synthesis of complexes **1-6**.
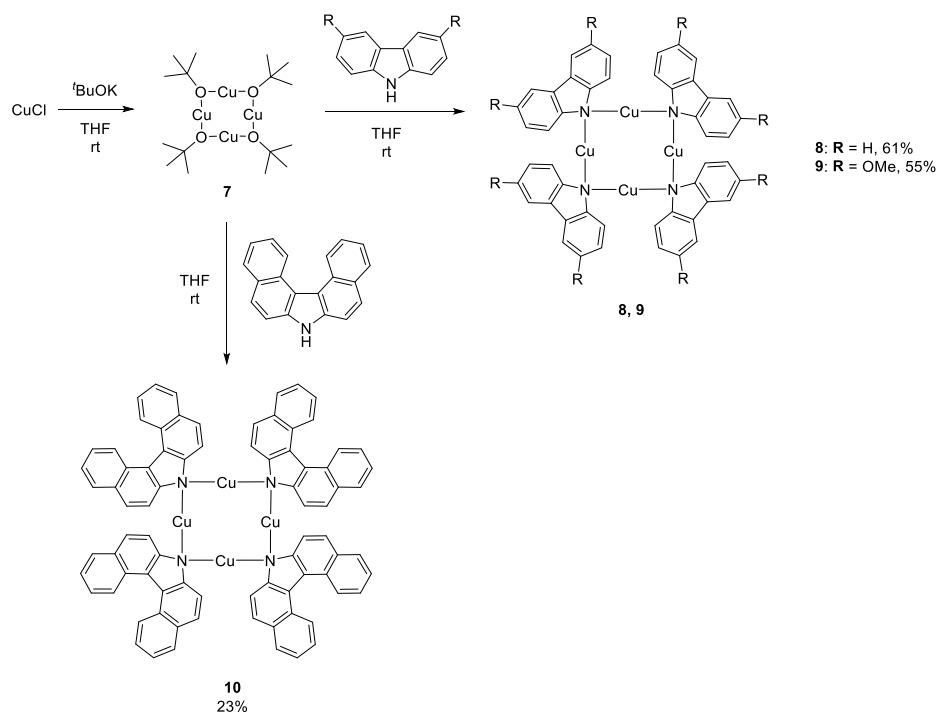
Scheme S2. Synthesis of copper clusters **8**-**10**.
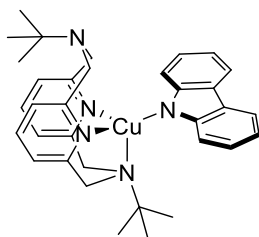

Scheme S3. Synthesis of **L2**.

Scheme S4. Synthesis of cross-liked poly(butyl acrylate) films **PBA1, 2, 4**.

The pyridinophane macrocycle ligand **L1** was prepared by the previously reported method.[3]

Synthesis of [(*tBu*N4)Cu(carbazole)] (1)

1

Method 1. Copper bromide (30.8 mg, 0.215 mmol) and **L1** (71.1 mg, 0.201 mmol) were suspended in the mixture of THF (3 mL) and acetonitrile (1 mL). The mixture was stirred for 1 hour at room temperature to give an orange solution. Carbazole (32.9 mg, 0.197 mmol), then potassium *tert*-butoxide (22.2 mg, 0.198 mmol) were added and the mixture was left stirring overnight at room temperature. The mixture was filtered through celite to remove potassium bromide. After reducing the amount of solvent under vacuum, orange crystals were grown by vapor diffusion with diethyl ether to the solution and subsequently keeping the vial at -30 °C in a refrigerator to obtain orange crystalline product. 58.8 mg, 0.101 mmol, 51% yield. Crystals suitable for X-ray analysis were obtained by vapor diffusion of the compound with acetone/diethyl ether.

Method 2. **L1** (9.6 mg, 0.027 mmol) and [Cu$_4$(Cbz)$_4$] (**8**) (6.1 mg, 0.027 mmol) were mixed in 1 mL of THF, and stirred at room temperature for 1 h. The mixture was filtered through celite and the set for vapor diffusion with diethyl ether to give the product as orange crystals. 9.0 mg, 0.015 mmol, 58%.

^{1}H NMR (600 MHz, -30 °C, CD$_2$Cl$_2$), δ: 8.05 (d, $^3J_{HH}$ = 7.5 Hz, 2H, C^4-H (Cz)), 7.55 (d, $^3J_{HH}$ = 8.0 Hz, 2H, C^1-H (Cz)), 7.34 (t, $^3J_{HH}$ = 7.6 Hz, 2H, *p*-H$_{py}$), 7.13 (t, $^3J_{HH}$ = 7.2 Hz, 2H, C^2-H (Cz)), 6.93 (d, $^3J_{HH}$ = 7.8 Hz, *m*-H$_{py}$, 2H), 6.89 (t, $^3J_{HH}$ = 7.2 Hz, 2H, C^3-H (Cz)), 6.78 (d, $^3J_{HH}$ = 7.6 Hz, 2H, *m*-H$_{py}$), 4.79 (d, $^2J_{HH}$ = 14.9 Hz, 2H, CH$_2$), 4.30 (d, $^2J_{HH}$ = 12.9 Hz, 2H, CH$_2$), 4.21 (d, $^2J_{HH}$ = 12.9 Hz, 2H, CH$_2$), 3.51 (d, $^2J_{HH}$ = 15.0 Hz, 2H, CH$_2$), 1.27 (s, 9H, H$_{tBu}$), 1.00 (s, 9H, H$_{tBu}$).

^{13}C{1H} NMR (151 MHz, -30 °C, CD$_2$Cl$_2$): δ 160.0 (quat. C$_{Ar}$), 155.5 (quat. C$_{Ar}$), 151.0 (quat. C$_{Ar}$), 136.3 (*p*-C$_{py}$), 124.0 (quat. C$_{Ar}$), 123.7 (*m*-C$_{py}$), 122.6 (C^2 (Cz)), 121.2 (*m*-C$_{py}$), 119.2 (C^4 (Cz)), 115.1 (C^1 (Cz)), 113.5 (C^3 (Cz)), 59.2 (CH$_2$), 58.3 (CH$_2$), 58.1 (CH$_2$), 56.3 (quat. C(CH$_3$)$_3$), 27.5 (C(CH$_3$)$_3$).

UV-Vis (THF), λ, nm (ε, M^{-1}×cm^{-1}): 243 (43000), 247 (43000), 288 (40000), 305(15000), 315(8700), 386(4000), 399(3800), 449(960).

Anal. Found (calcd for C$_{34}$H$_{40}$Cu$_1$N$_5$): C, 69.84 (70.13), H, 6.83 (6.92), N, 11.83 (12.03).

FT-IR (ATR, solid): υ 713, 732, 752, 777, 804, 844, 861, 891, 912, 923, 993, 1008, 1059, 1072, 1086, 1110, 1139, 1159, 1192, 1231, 1271, 1292, 1327, 1347, 1366, 1392, 1440, 1459, 1572, 1597, 1616, 2921, 2957, 3038, 3061.
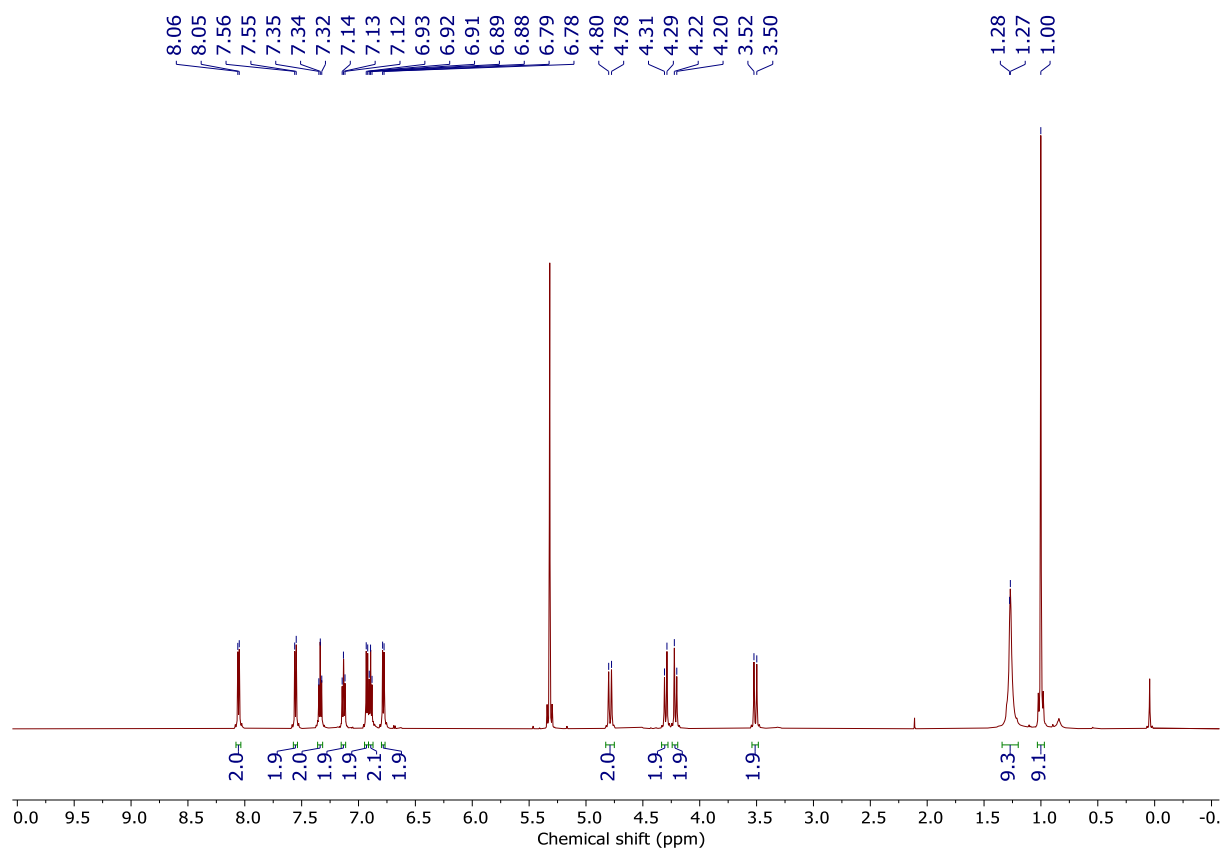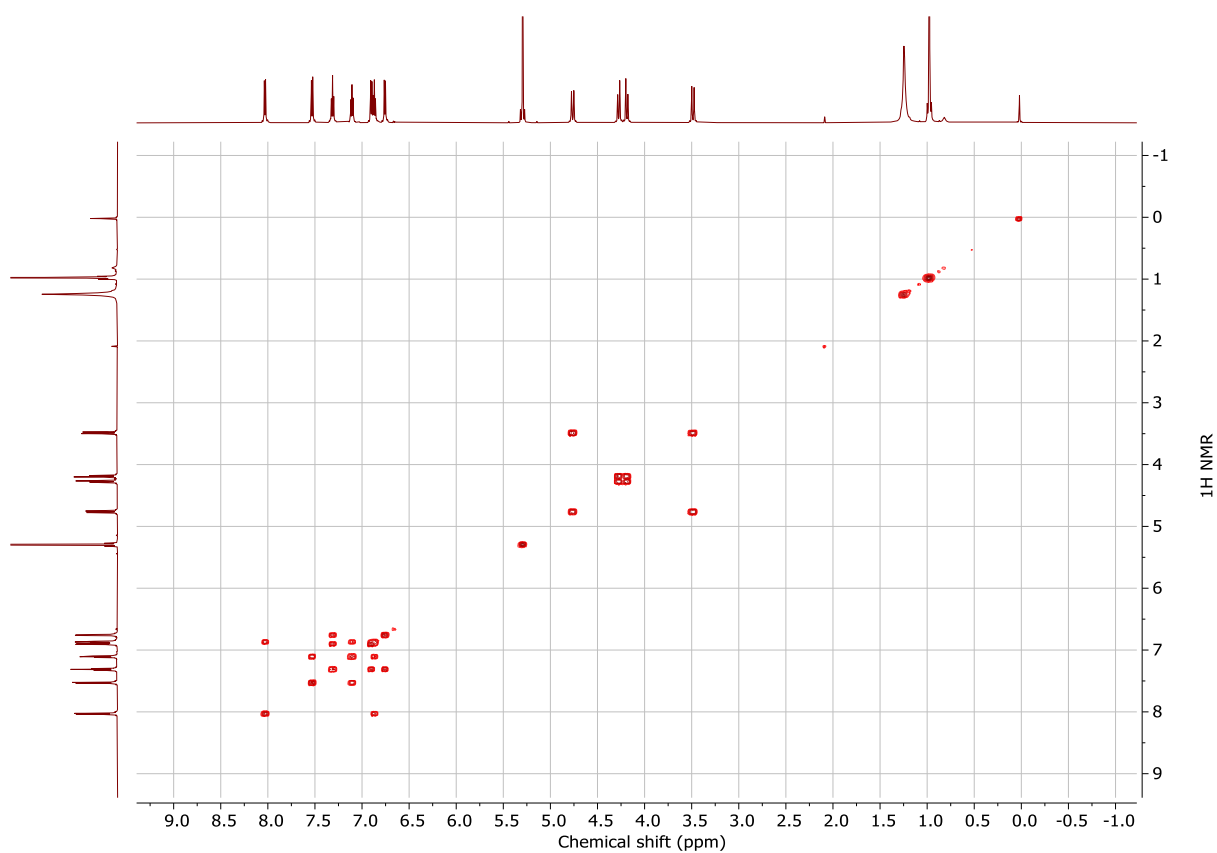
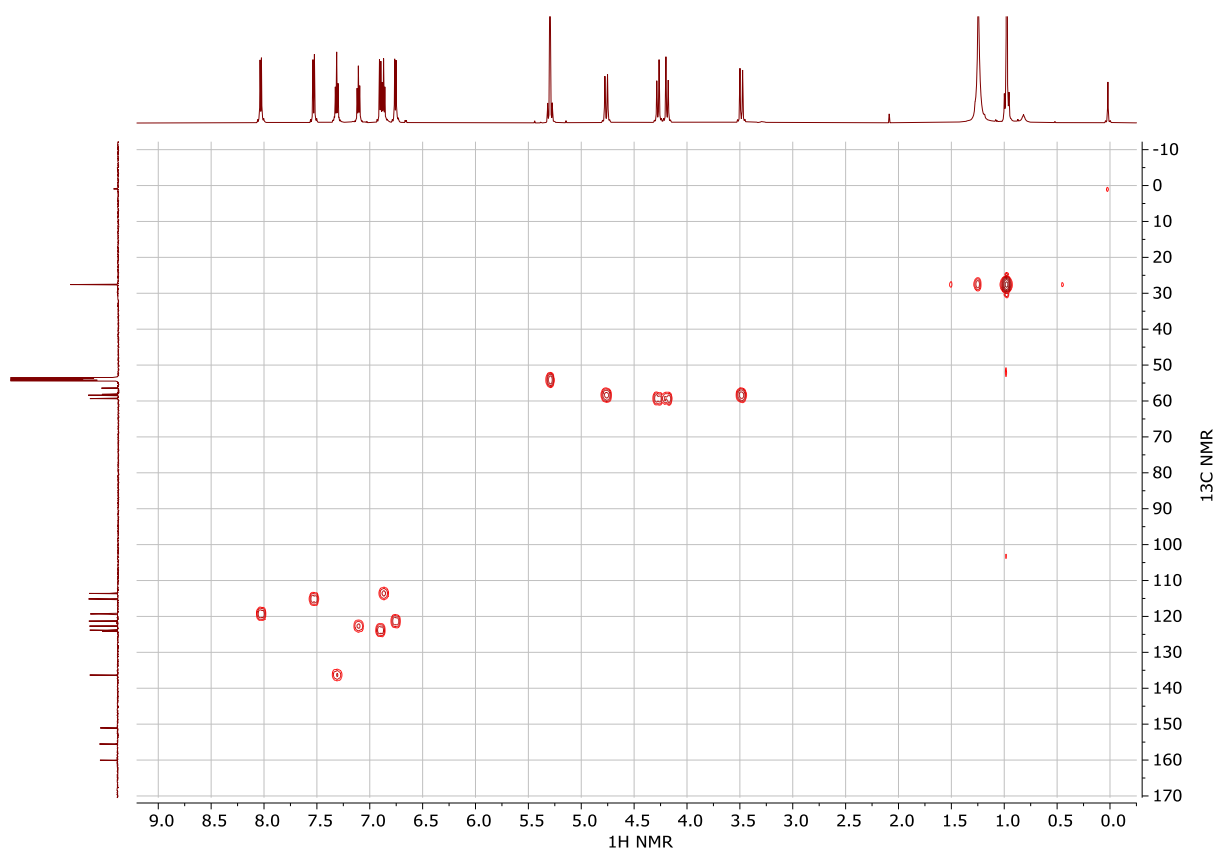**Figure S1**. ^{1}H NMR (600 MHz) spectrum of complex **1** in CD$_2$Cl$_2$ at -30 °C.
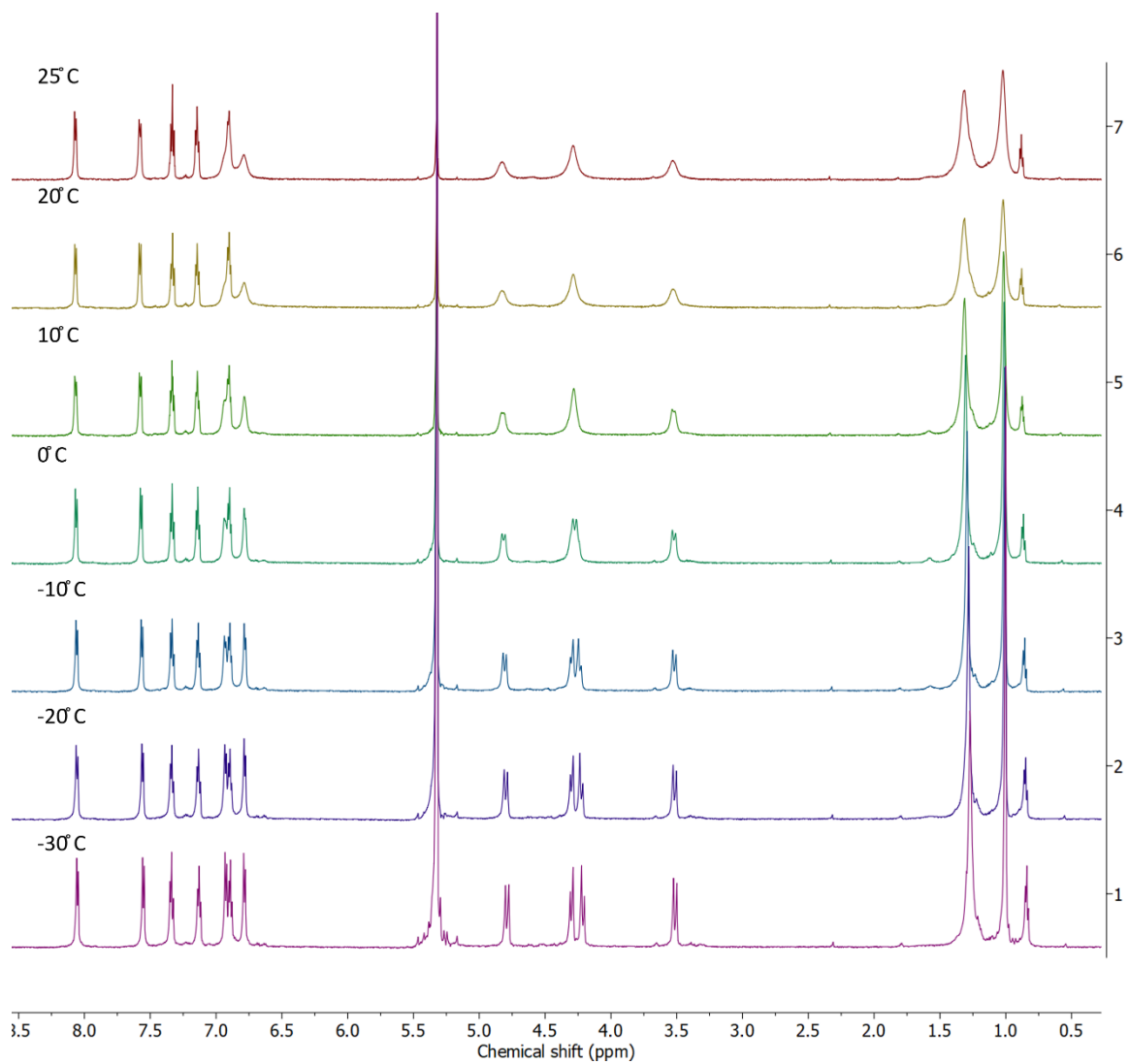
Figure S2. Variable temperature ^1H NMR (600 MHz) spectra of complex **1** in CD_2Cl_2.
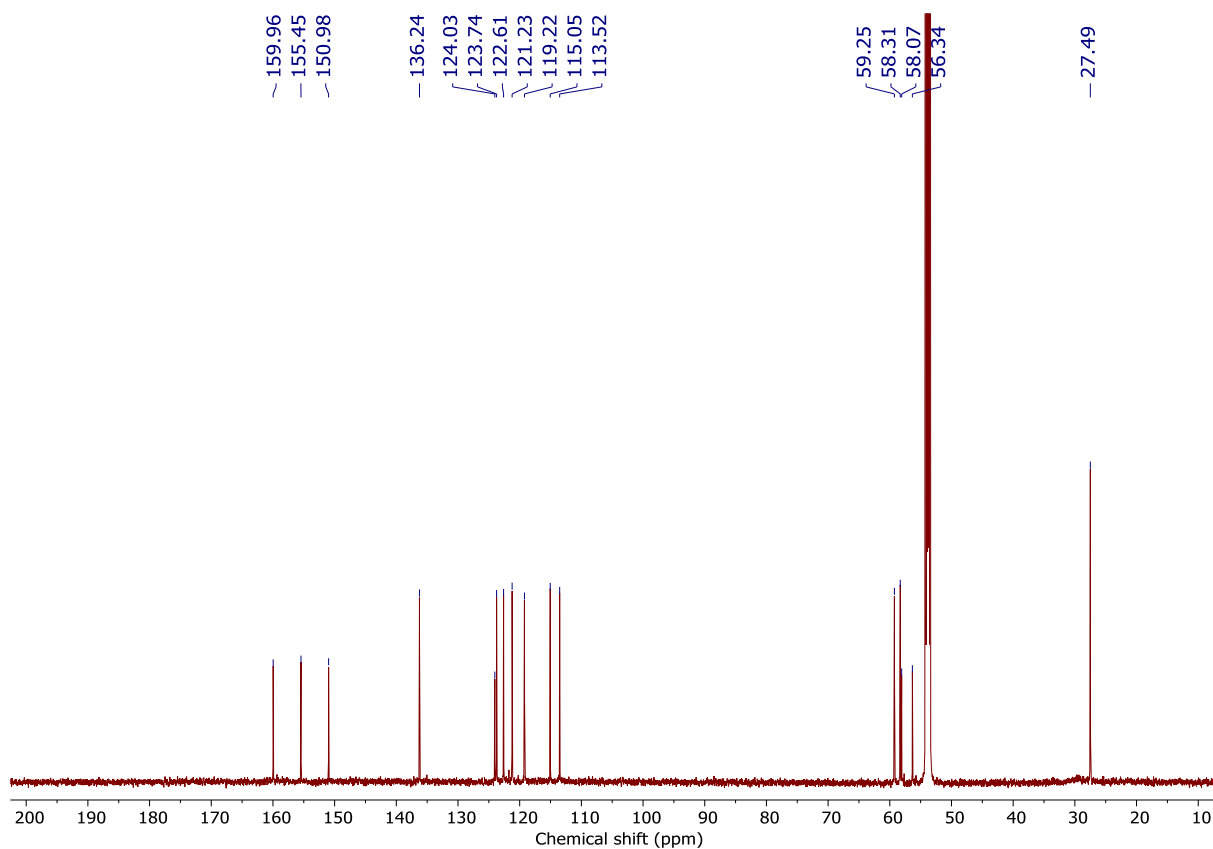
Figure S3. $^{13}C\{^1H\}$ (151 MHz) NMR spectrum of complex **1** in CD_2Cl_2 at -30 °C.

Figure S4. ^1H-^1H COSY spectrum of complex **1** in CD_2Cl_2 at -30 °C.

Figure S5. ^1H-^{13}C HMQC spectrum of complex **1** in CD_2Cl_2 at -30 °C.
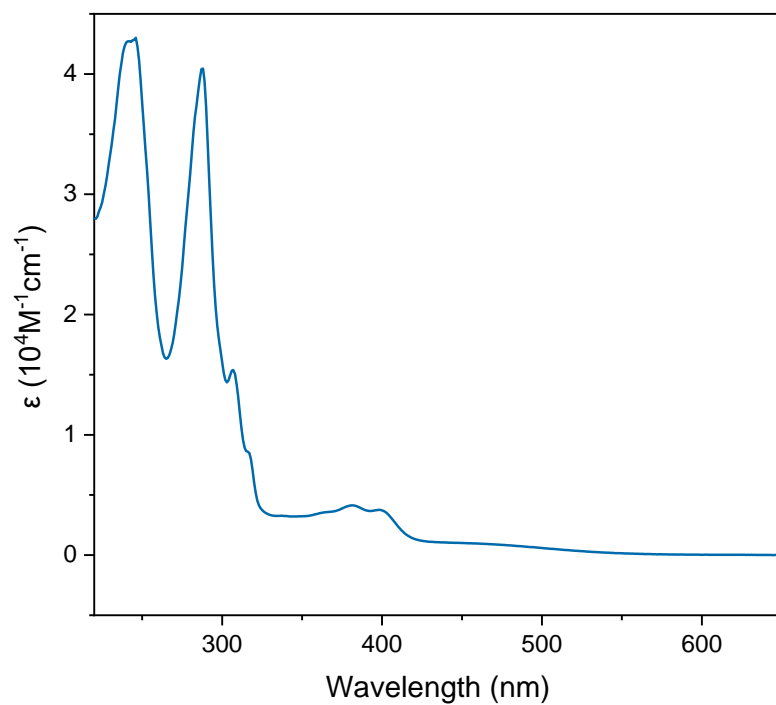
Figure S6. UV-Vis absorption spectrum of **1** in THF.
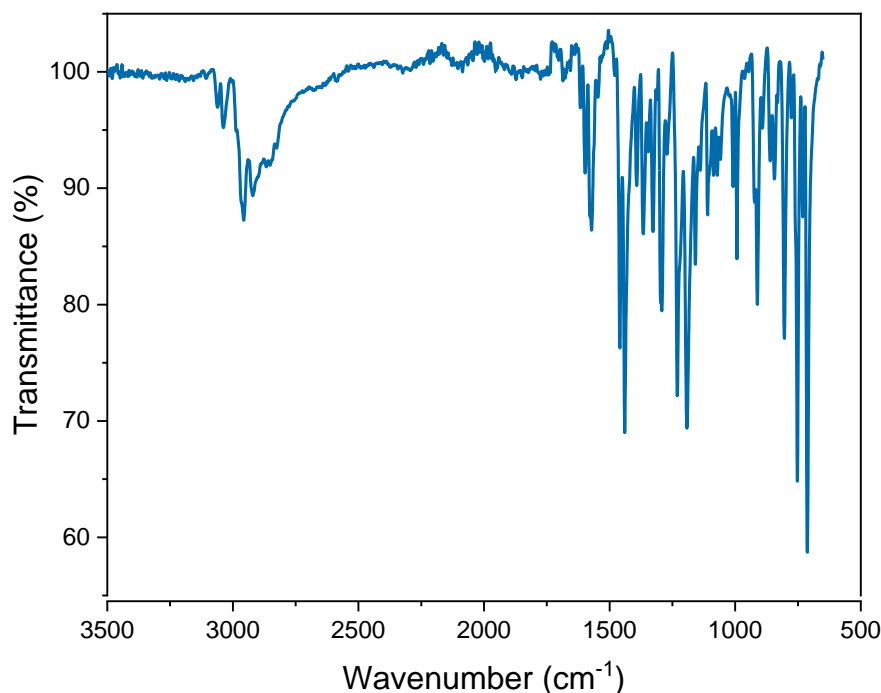
Figure S7. FT-IR spectrum of complex **1**.

Synthesis of [(^{tBu}N4)Cu(MeO$_2$-carbazole)] (2)
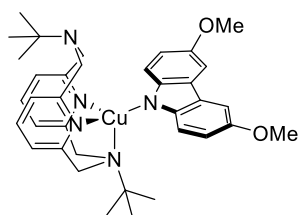
2

Method 1. Copper bromide (31.9 mg, 0.222 mmol) and **L1** (76.9 mg, 0.218 mmol) were suspended in 10 mL of THF. The mixture was stirred for 1 hour at room temperature to give an orange solution. 3,6-dimethoxy-9H-carbazole (54.5 mg, 0.239 mmol), then potassium *tert*-butoxide (25.7 mg, 0.229 mmol) were added and the mixture was left stirring overnight at room temperature. The mixture was filtered through celite to remove the remaining potassium bromide. The resulting solution was dried to give red-orange powder, which was crystallized by vapor diffusion with pentane to the THF two times to give orange crystals. 51.7 mg, 37% yield.

Method 2. **L1** (16.5 mg, 0.0468 mmol) and [Cu$_4$(^{MeO2}Cbz)$_4$] (**9**) (13.2 mg, 0.0455 mmol)were mixed in 4 mL of THF, and stirred at room temperature for 1 h. The mixture was filtered through celite and the set for vapor diffusion with diethyl ether to give orange crystals. 19.6 mg, 0.0305 mmol, 67%.

^{1}H NMR (600 MHz, -30 °C, CD$_2$Cl$_2$), δ: 7.52 (d, $^4J_{HH}$ = 2.5 Hz, 2H, C^4-H (Cz)), 7.43 (d, $^3J_{HH}$ = 8.8 Hz, 2H, C^1-H (Cz)), 7.32 (t, $^3J_{HH}$ = 7.7 Hz, 2H, p-H$_{py}$), 6.91 (d, $^3J_{HH}$ = 7.7 Hz, m-H$_{py}$, 2H), 6.78-6.74 (m, 4H, H$_{Ar}$), 4.76 (d, $^2J_{HH}$ = 15.2 Hz, 2H, CH$_2$), 4.28 (d, $^2J_{HH}$ = 12.8 Hz, 2H, CH$_2$), 4.20 (d, $^2J_{HH}$ = 12.9 Hz, 2H, CH$_2$), 3.87 (s, 6H, OCH$_3$), 3.49 (d, $^2J_{HH}$ = 15.1 Hz, 2H, CH$_2$), 1.26 (s, 9H, H$_{tBu}$), 1.00 (s, 9H, H$_{tBu}$).

^{13}C{1H} NMR (151 MHz, -30 °C, CD$_2$Cl$_2$): δ 160.0 (quat. C$_{Ar}$), 155.5 (quat. C$_{Ar}$), 149.7 (quat. C$_{Ar}$), 146.7 (quat. C$_{Ar}$), 136.2 (p-C$_{py}$), 123.7 (m-C$_{py}$), 122.9 (quat. C$_{Ar}$), 121.2 (m-C$_{py}$), 115.9 (C$_{Cz}$), 112.6

(C_{Cz}), 100.4 (C_{Cz}), 59.2 (CH_2), 58.3 (CH_2), 58.1 (CH_2), 56.3 (quat. $C(CH_3)_3$), 55.6 (OCH_3), 27.5 ($C(CH_3)_3$).
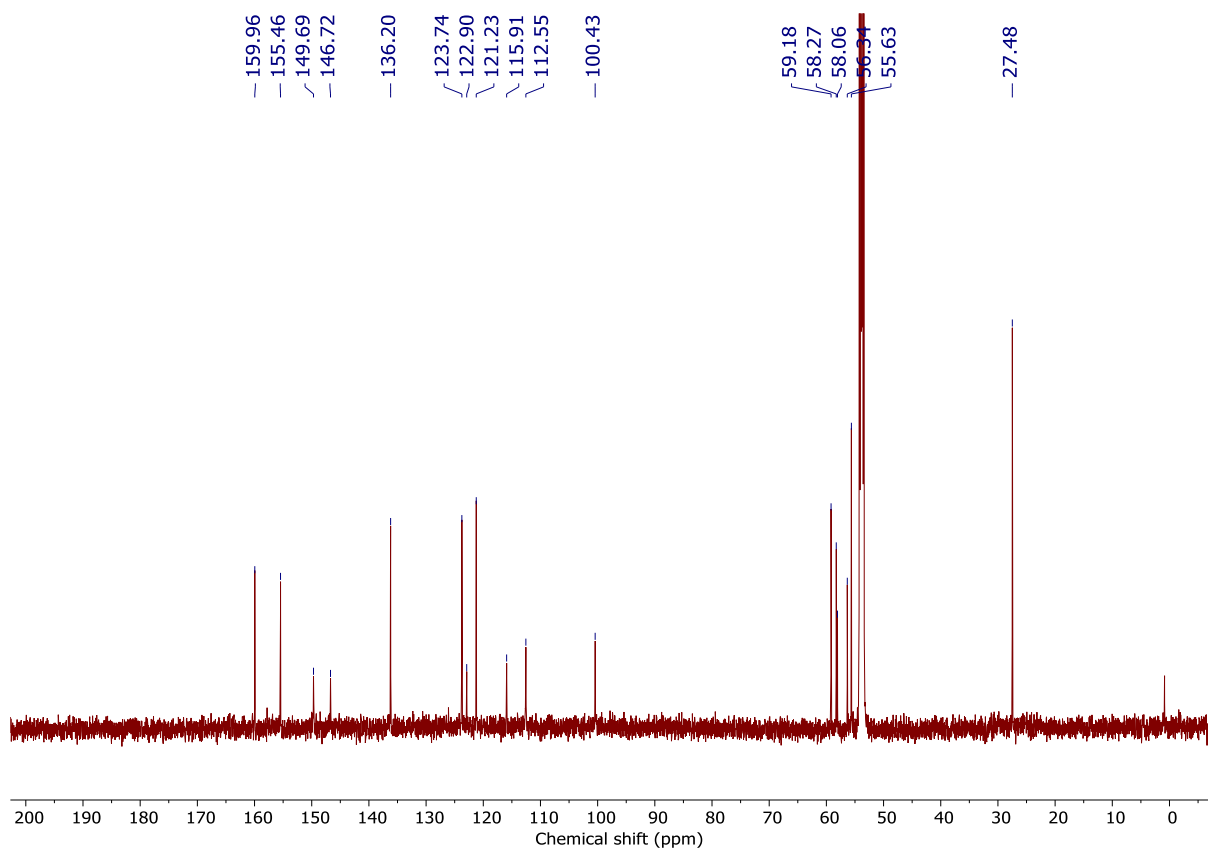
UV-Vis (THF), λ, nm (ε, $M^{-1} \times cm^{-1}$): 300(21000), 318(14000), 332(19000), 408(4000), 430(3800), 481(870).

Anal. Found (calcd for $C_{36}H_{44}Cu_1N_5$): C, 66.86 (67.32), H, 6.67 (6.90), N, 10.64 (10.90).
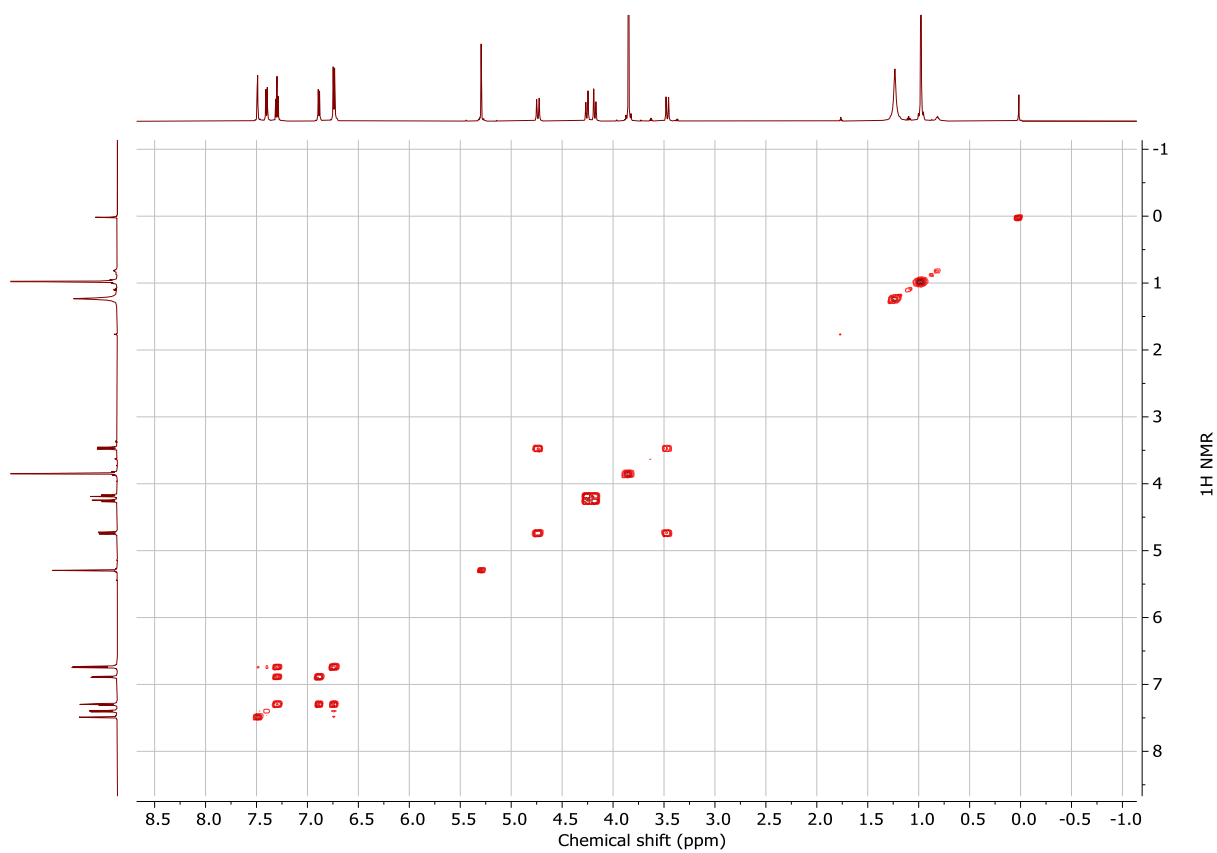
FT-IR (ATR, solid): υ 722, 731, 757, 789, 807, 851, 898, 915, 924, 1036, 1058, 1071, 1085, 1101, 1125, 1145, 1166, 1193, 1203, 1243, 1283, 1315, 1343, 1367, 1393, 1430, 1456, 1563, 1574, 1598, 2822, 2971.
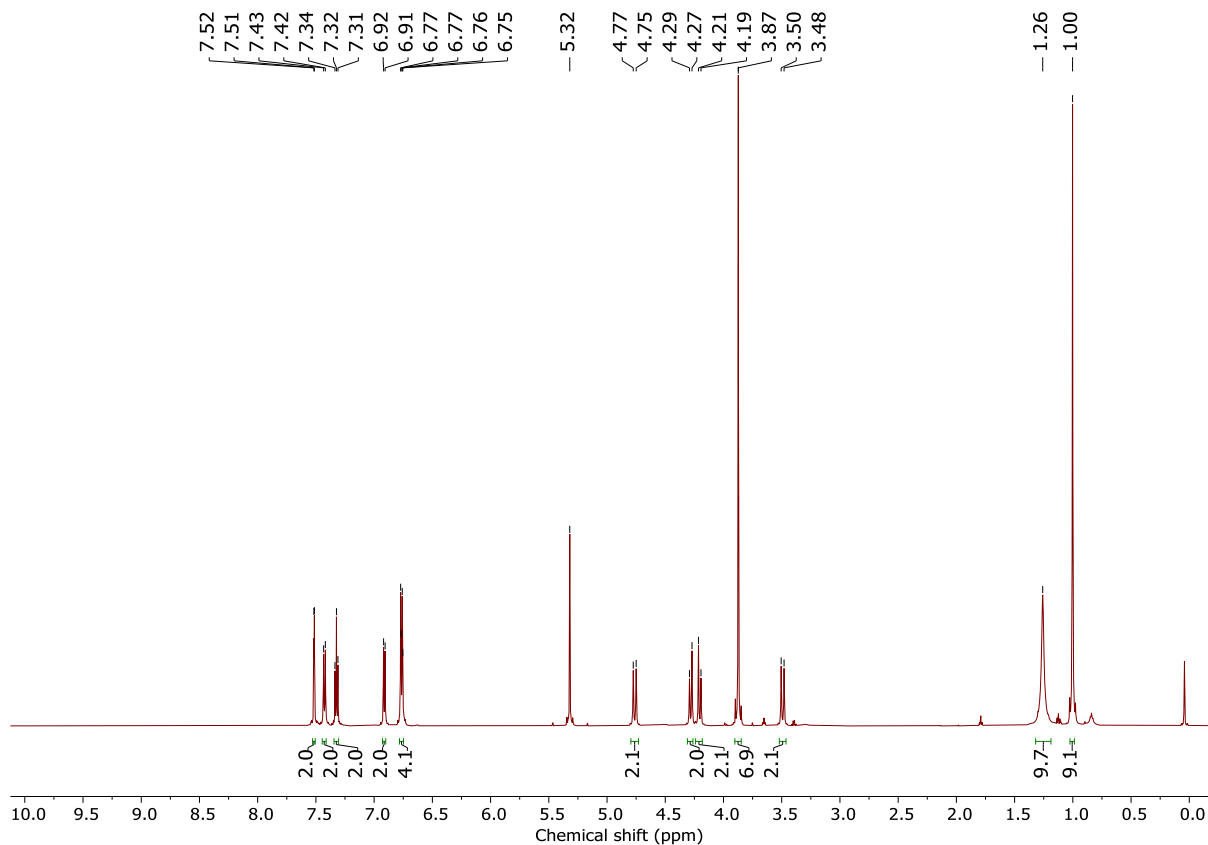
Figure S8. ^1H NMR (600 MHz) spectrum of complex **2** in CD_2Cl_2 at -30 °C.

Figure S9. $^{13}C\{^1H\}$ NMR . (151 MHz) spectrum of complex **2** in CD_2Cl_2 at -30 °C.

Figure S10. ^1H-^1H COSY spectrum of complex **2** in CD_2Cl_2 at -30 °C.
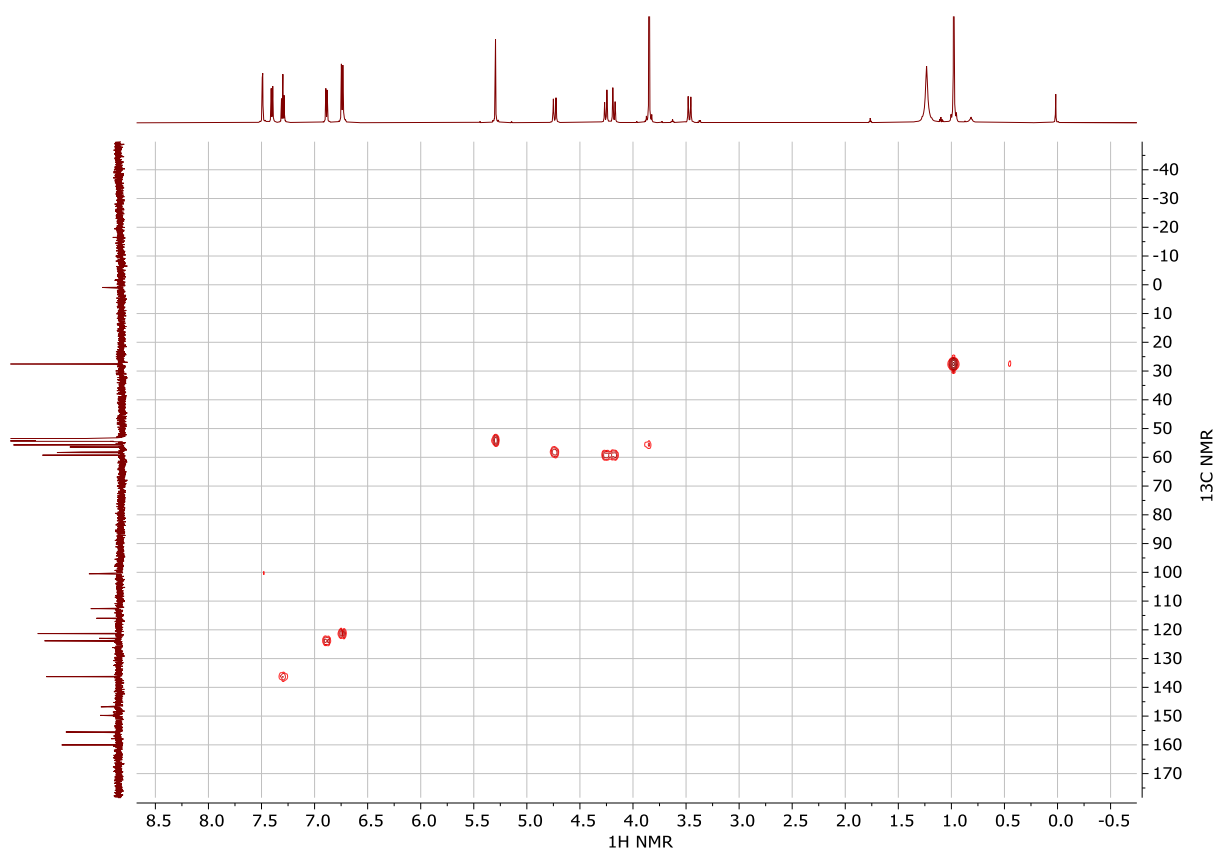
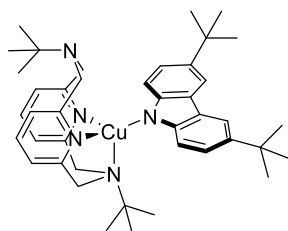**Figure S11**. ^{1}H-^{13}C HMQC spectrum of complex **2** in CD$_2$Cl$_2$ at -30 °C.
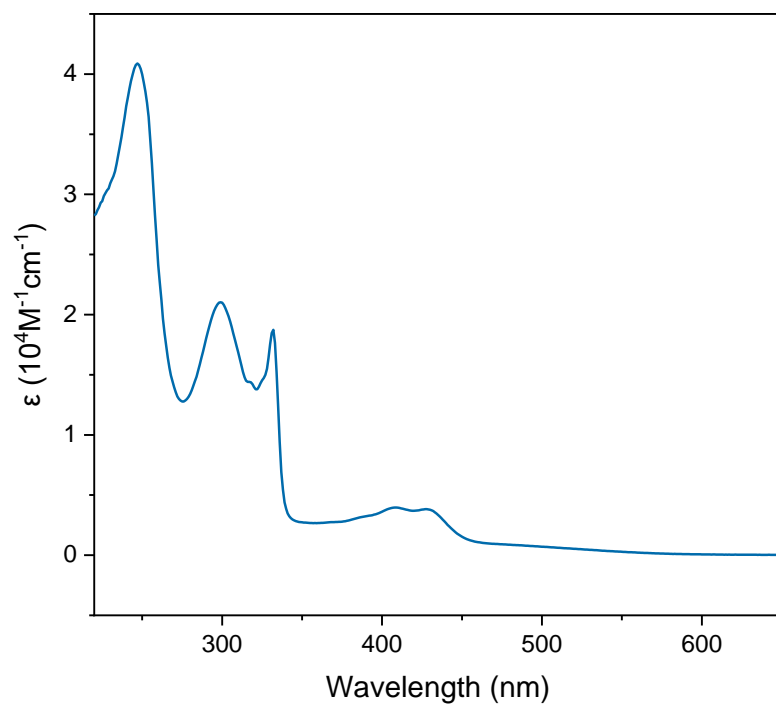
Figure S12. UV-Vis absorption spectrum of complex **2** in THF.
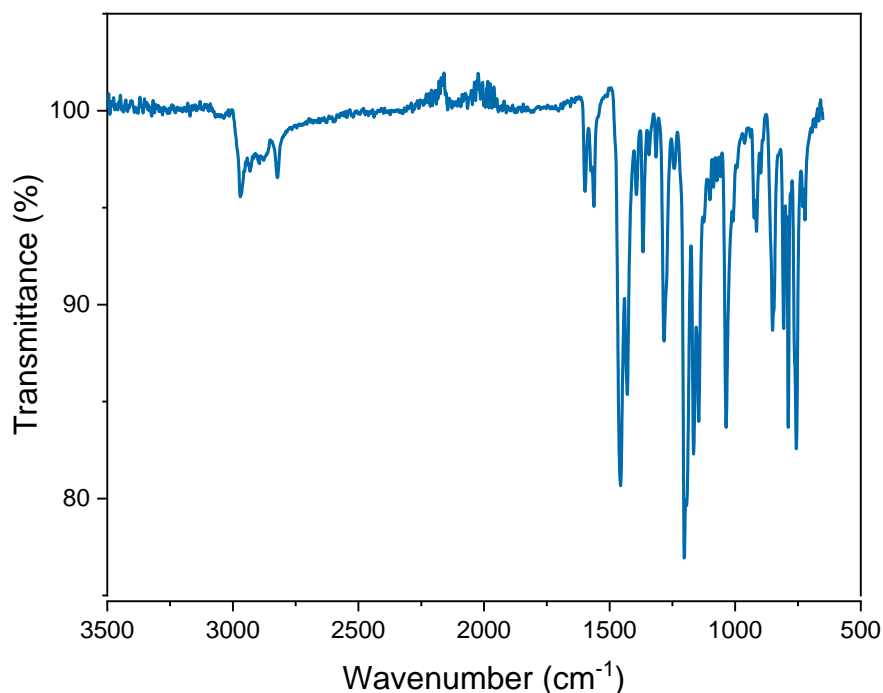
Figure S13. FT-IR spectrum of complex **2**.

Synthesis of [(^{tBu}N4)Cu(^{t}Bu$_2$-carbazole)] (3)

3

Copper bromide (26.0 mg, 0.181 mmol) and **L1** (63.1 mg, 0.179 mmol) were suspended in 7.5 mL of THF. The mixture was stirred for 3 hours at room temperature to give an orange solution. 3,6-di-*tert*-butylcarbazole (53.2 mg, 0.190 mmol), then potassium *tert*-butoxide (20.0 mg, 0.178 mmol) were added and the mixture was left stirring overnight at room temperature. Since the NMR of the mixture at this point contained peaks ascribed to [(^{t}BuN$_4$)CuBr] complex, additional portion of potassium *tert*-butoxide (5.8 mg, 0.052 mmol) was added. After stirring overnight, the reaction was confirmed to be complete by NMR, and the mixture was filtered through celite to remove the remaining potassium bromide. The resulting solution was dried to give red powder, which was crystallized by vapor diffusion with pentane to THF two times to give red crystals. 45.2 mg, 0.0651 mmol, 37% yield.

^{1}H NMR (600 MHz, -30 °C, CD$_2$Cl$_2$): δ 8.05 (d, $^4J_{HH}$ = 1.9 Hz, 2H, C^4-H (Cz)), 7.38 (d, $^3J_{HH}$ = 8.6 Hz, 2H, C^1-H (Cz)), 7.35 (t, $^3J_{HH}$ = 7.7 Hz, 2H, *p*-H$_{py}$), 7.17 (dd, $^3J_{HH}$ = 8.5 Hz, $^4J_{HH}$ = 2.0 Hz, 2H, C^2-H (Cz)), 6.94 (d, $^3J_{HH}$ = 7.6 Hz, 2H, *m*-H$_{py}$), 6.80 (d, $^3J_{HH}$ = 7.6 Hz, 2H, *m*-H$_{py}$), 4.77 (d, $^2J_{HH}$ = 15.1 Hz, 2H, CH$_2$), 4.33 (d, $^2J_{HH}$ = 13.0 Hz, 2H, CH$_2$), 4.25 (d, $^2J_{HH}$ = 13.0 Hz, 2H, CH$_2$), 3.51 (d, $^2J_{HH}$ = 15.2 Hz, 2H, CH$_2$), 1.42(s, 18H, Ar-C(CH$_3$)$_3$), 1.27 (s, 9H, N-C(CH$_3$)$_3$), 1.04 (s, 9H, N-C(CH$_3$)$_3$).

^{13}C{1H} NMR (151 MHz, -30 °C, CD$_2$Cl$_2$): δ 160.0 (quat. C$_{Ar}$), 155.5 (quat. C$_{Ar}$), 149.7 (quat. C$_{Ar}$), 136.3 (*p*-C$_{py}$), 135.6 (quat. C$_{Ar}$), 123.7 (*m*-C$_{py}$), 123.6 (*m*-C$_{py}$), 121.2 (*m*-C$_{py}$), 120.5 (C^2 (Cz)), 115.1

$(C^4 (Cz))$, 114.1 $(C^1 (Cz))$, 59.5 (CH_2), 58.1 (CH_2), 58.0 (CH_2), 56.5 (quat. $C(CH_3)_3$), 34.4 (quat. $C(CH_3)_3$), 32.1 $(Ar-C(CH_3)_3)$, 27.7 $(N- C(CH_3)_3)$.

UV-Vis (THF), λ, nm (ε, $M^{-1} \times cm^{-1}$): 246 (44000), 250 (43000), 290 (38000), 310(15000), 320 (10000), 385 (3800), 404, (3400), 470 (850).

Anal. Found (calcd for $C_{42}H_{56}Cu_1N_5$): C, 72.53 (72.64), H, 8.37 (8.13), N, 10.03 (10.08).
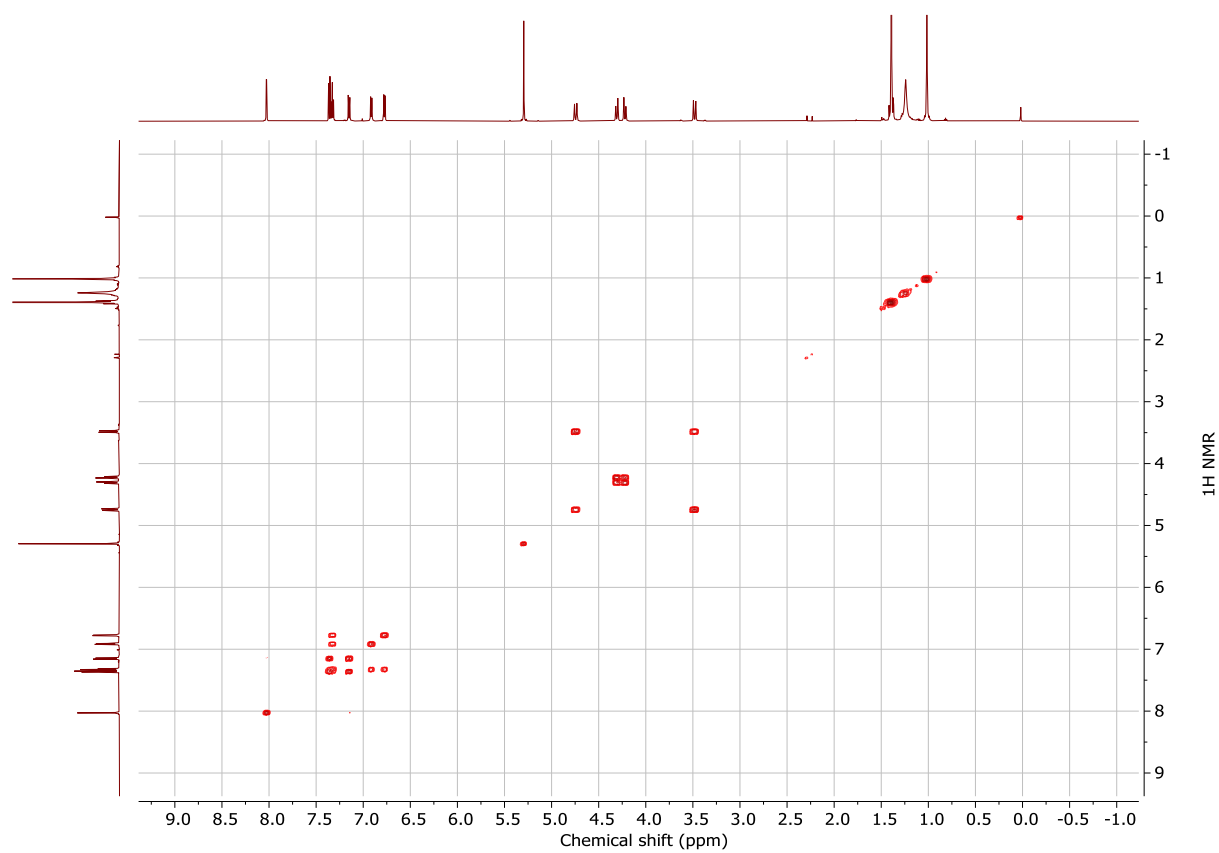
FT-IR (ATR, solid): υ 690, 731, 754, 805, 836, 850, 870, 913, 924, 1007, 1027, 1058, 1073, 1083, 1099, 1136, 1157, 1192, 1236, 1256, 1291, 1359, 1391, 1449, 1474, 1460, 1572, 1595, 1625, 2862, 2898, 2948.
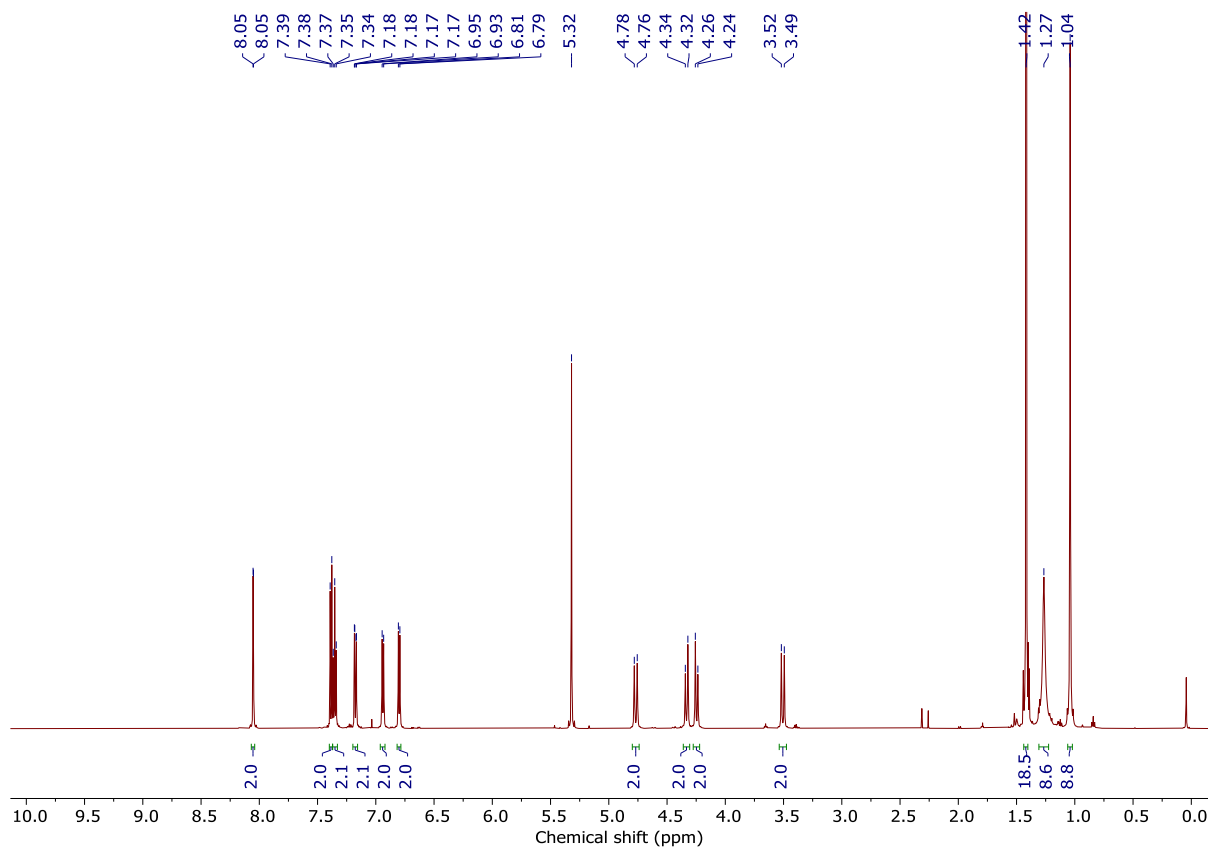
Figure S14. ^{1}H NMR (600 MHz) spectrum of complex **3** in CD_2Cl_2 at -30 °C.
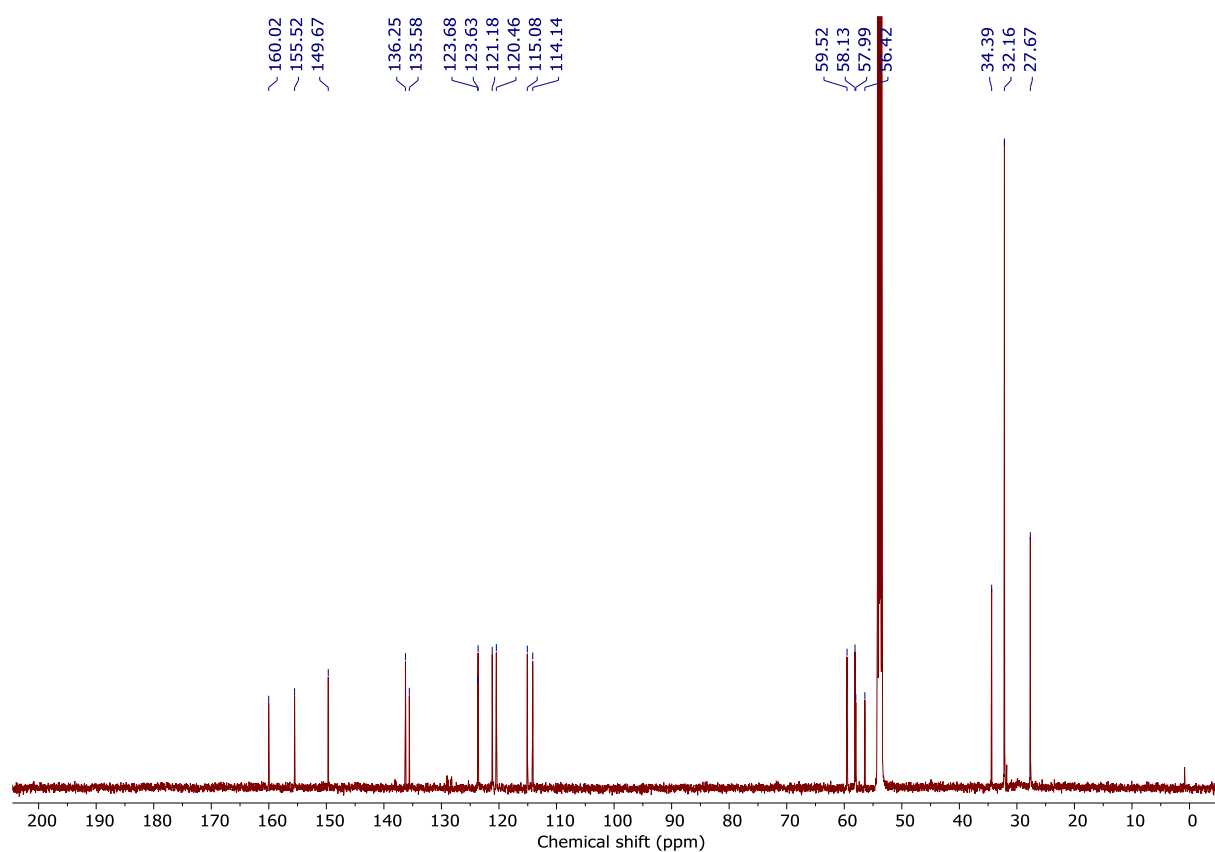
Figure S15. $^{13}C\{^1H\}$ NMR (151 MHz) spectrum of complex **3** in CD_2Cl_2 at -30 °C.

Figure S16. ^1H-^1H COSY spectrum of complex **3** in CD_2Cl_2 at -30 °C.
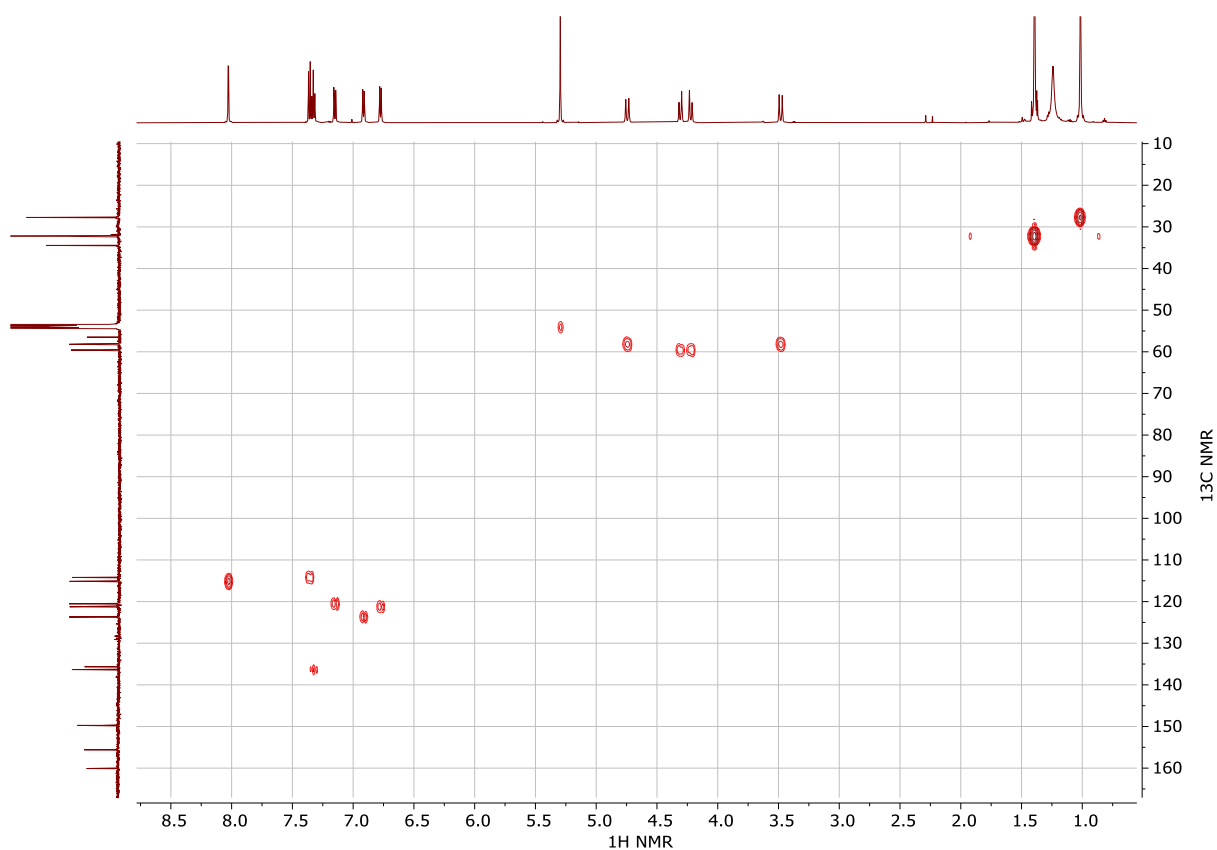
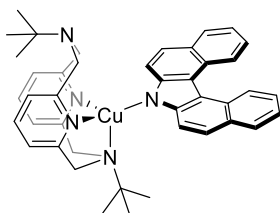**Figure S17**. ^1H-^{13}C HMQC spectrum of complex **3** in CD_2Cl_2 at -30 °C.
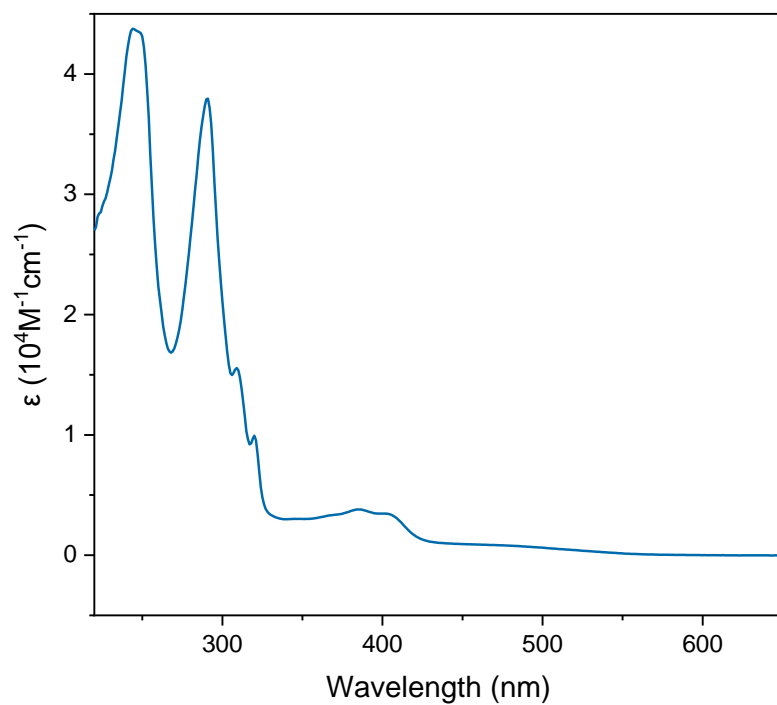
Figure S18. UV-Vis absorption spectrum of complex **3** in THF.
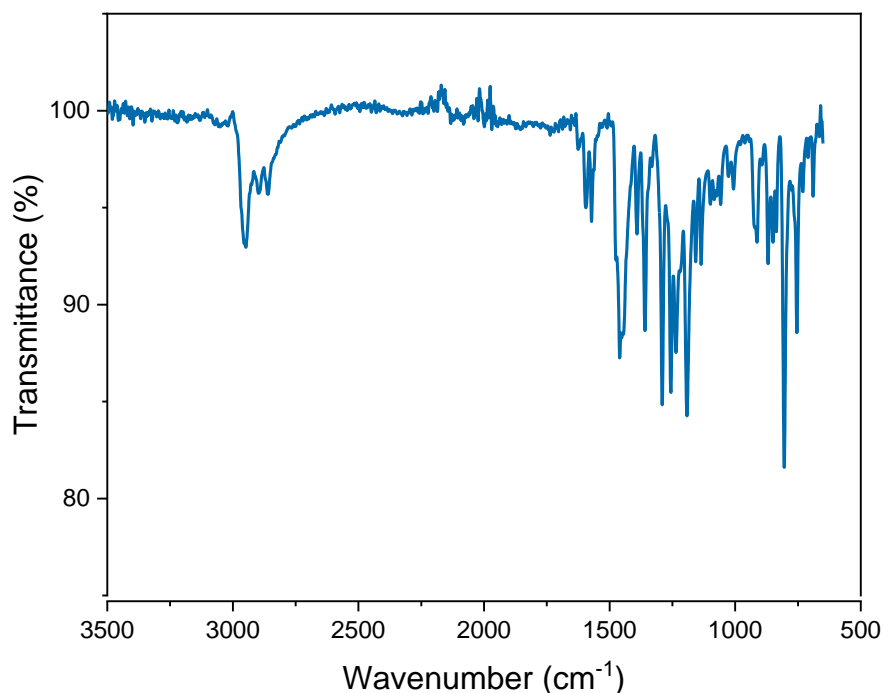
Figure S19. FT-IR spectrum of complex **3**.

Synthesis of [(^{tBu}N4)Cu(dibenzocarbazole)] (4)

4

Copper bromide (40.7 mg, 0.284 mmol) and **L1** (100.1 mg, 0.284 mmol) were suspended in 10 mL of THF. The mixture was stirred for 1 hour at room temperature to give an orange solution. 7H-dibenzo[c,g]carbazole (76.1 mg, 0.285 mmol), then potassium *tert*-butoxide (32.1 mg, 0.286 mmol) were added and the mixture was left stirring overnight at room temperature. The mixture was filtered through celite to remove the remaining potassium bromide. The resulting solution was dried to give red-orange powder, which was crystallized by vapor diffusion with diethyl ether to the THF two times. (68.0 mg, 0.0996 mmol, 35%). The first crystallization gave orange plate crystals which were confirmed to be the product with a κ^3 coordinating pyridinophane ligand and one diethyl ether molecule (κ^3-**4**) (Figure S75). The second crystallization gave red crystals which were confirmed to be the product with a κ^4-coordinated pyridinophane ligand without solvent molecules (κ^4-**4**) (Figure S77). The homogeneity of both crystalline samples was confirmed by powder XRD analysis.

Method 2. **L1** (10.4 mg, 0.0295 mmol) and [Cu$_4$(^{Bn2}Cbz)$_4$] (**10**) (9.6 mg, 0.029 mmol) were mixed in 2 mL of THF, and stirred at room temperature for 1 h. The mixture was filtered through celite and the set for vapor diffusion with diethyl ether to give red crystals. 15.4 mg, 0.023 mmol, 79%.

Cooling the solution of complex **4** in THF : diethyl ether 1 : 2 mixture at -30°C was found to be an effective way to obtain the orange crystals of κ^3-**4** selectively. Photophysical properties of the crystalline

samples of κ^3-**4** were measured for the crystals obtained by this method and containing diethyl ether molecule in a unit cell as confirmed by SC-XRD and comparison of PXRD of a bulk sample with a simulated pattern for this crystal modification.

On the other hand, vapor diffusion of the THF solution of the complex with pentane selectively gave red crystals of, κ^4-**4**. The photophysical properties for κ^4-**4** were measured for red-crystalline sample of κ^4-**4**; the purity of the bulk sample was confirmed by comparison of PXRD results with simulated pattern for this crystal structure. Sometimes a small amount of yellow crystals were present, which could be easily separated and analyzed by SC-XRD showing another crystalline modification of κ^3-**4** which contained no diethyl ether in a unit cell (κ^3-**4**-2, Figure S76). The properties of κ^3-**4**-2 could not be measured due to the difficulty of getting a sufficient amount.

For characterization by NMR, UV-Vis, FT-IR spectroscopy and elemental analysis, the red crystals of κ^4-**4** were used.

^{1}H NMR of κ^3-**4** (600 MHz, -30 °C, CD$_2$Cl$_2$), δ: 9.21 (d, J_{HH} = 7.9 Hz, 2H, H$_{Ar}$), 8.03 (d, J_{HH} = 8.5 Hz, 2H, H$_{Ar}$), 7.92 (d, J_{HH} = 7.8 Hz, 2H, H$_{Ar}$), 7.58-7.50 (m, 4H, H$_{Ar}$) 7.36 (t, $^3J_{HH}$ = 7.5 Hz, 2H, p-H$_{py}$), 7.32 (t, J_{HH} = 6.6 Hz, 2H, H$_{Ar}$), 6.95 (d, $^3J_{HH}$ = 7.7 Hz, 2Hz, m-H$_{py}$), 6.81 (d, $^3J_{HH}$ = 7.4 Hz, 2H, m-H$_{py}$), 4.85 (d, $^2J_{HH}$ = 15.2 Hz, 2H, CH$_2$), 4.30 (d, $^2J_{HH}$ = 12.8 Hz, 2H, CH$_2$), 4.20 (d, $^2J_{HH}$ = 13.0 Hz, 2H, CH$_2$), 3.55 (d, $^2J_{HH}$ = 15.2 Hz, 2H, CH$_2$),1.28 (s, 9H, H$_{tBu}$), 0.95 (s, 9H, H$_{tBu}$).

Peaks at 4.57, 3.34 ppm (doublets, J = 15.0 Hz, geminally coupled CH$_2$) and 0.82 ppm (singlet, ^{t}Bu) are assigned to a symmetrical (κ^4-N4)Cu(dibenzocarbazole); the estimated ratio of κ^3 : κ^4 isomers of 20 : 1 at -30 °C.

The fluxional behavior of two isomers of **4** was confirmed by variable temperature NMR measurements (see below) and it is consistent with the previous studies.[1, 4]

^{13}C{^{1}H} NMR of κ^3-**4** (151 MHz, -30 °C, CD$_2$Cl$_2$): δ 160.0 (quat. C$_{Ar}$), 155.4 (quat. C$_{Ar}$), 147.6 (quat. C$_{Ar}$), 136.4 (p-C$_{py}$), 130.1 (quat. C$_{Ar}$), 128.6 (C$_{Ar}$), 128.5 (C$_{Ar}$), 124.3 (C$_{Ar}$), 123.9 (m-C$_{py}$), 123.5 (quat. C$_{Ar}$), 122.5 (C$_{Ar}$), 121.4 (m-C$_{py}$), 120.5 (C$_{Ar}$), 120.2 (C$_{Ar}$), 117.2 (quat. C$_{Ar}$), 59.2 (CH$_2$), 58.5 (CH$_2$), 58.3 (quat. C(CH$_3$)$_3$), 56.4 (CH$_2$), 27.4 (C(CH$_3$)$_3$).

UV-Vis (THF), λ, nm (ε, M^{-1}×cm^{-1}): 237 (20000), 254 (10000), 264 (10000), 286 (9000), 314 (13000), 339 (12000), 390 (5000), 398 (5000), 462 (540).
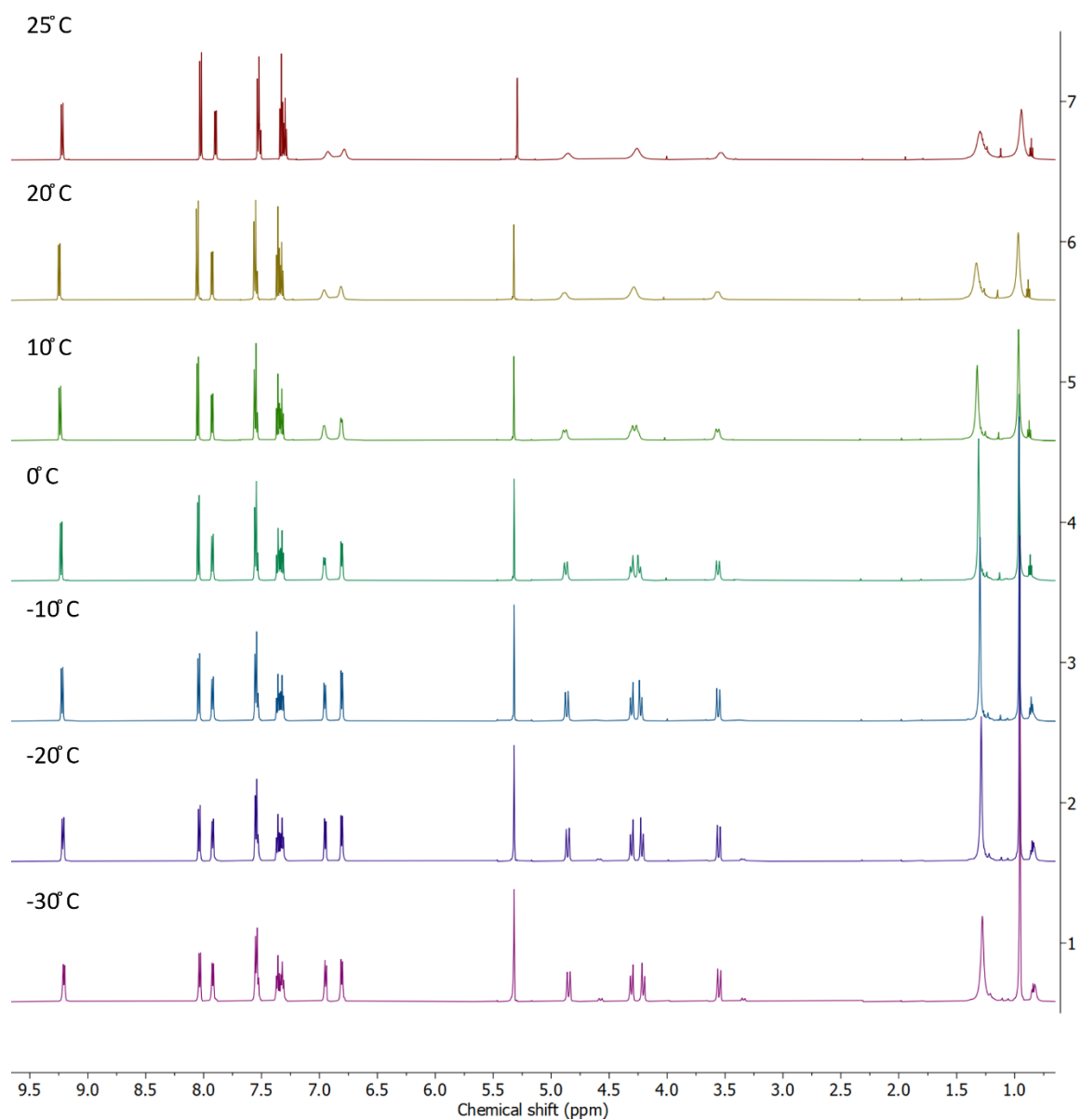
Anal. Found (calcd for C$_{42}$H$_{44}$Cu$_1$N$_5$): C, 73.51 (73.93), H, 6.33 (6.50), N, 10.32 (10.26).

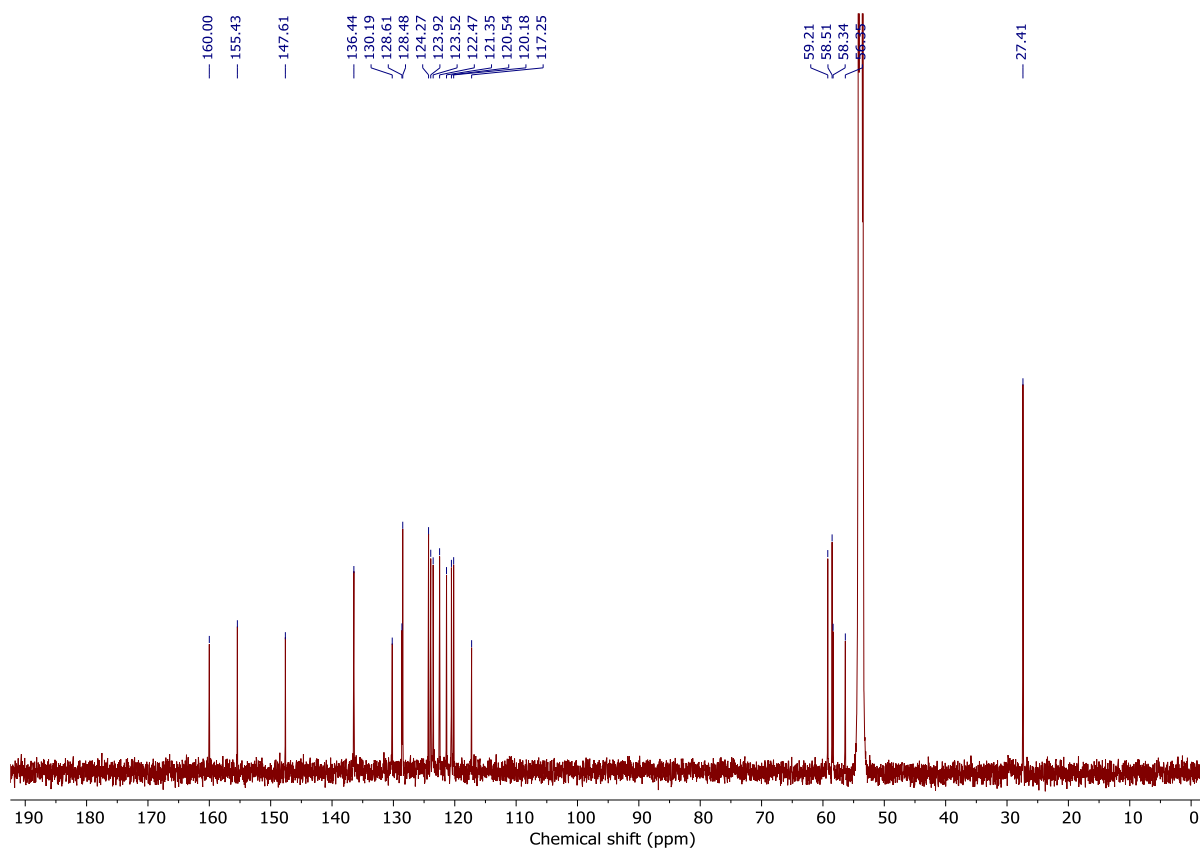FT-IR (ATR, solid): υ 740, 808, 856, 931, 1012, 1131, 1194, 1246, 1297, 1326, 1371, 1434, 1523, 1571, 1599, 2963.
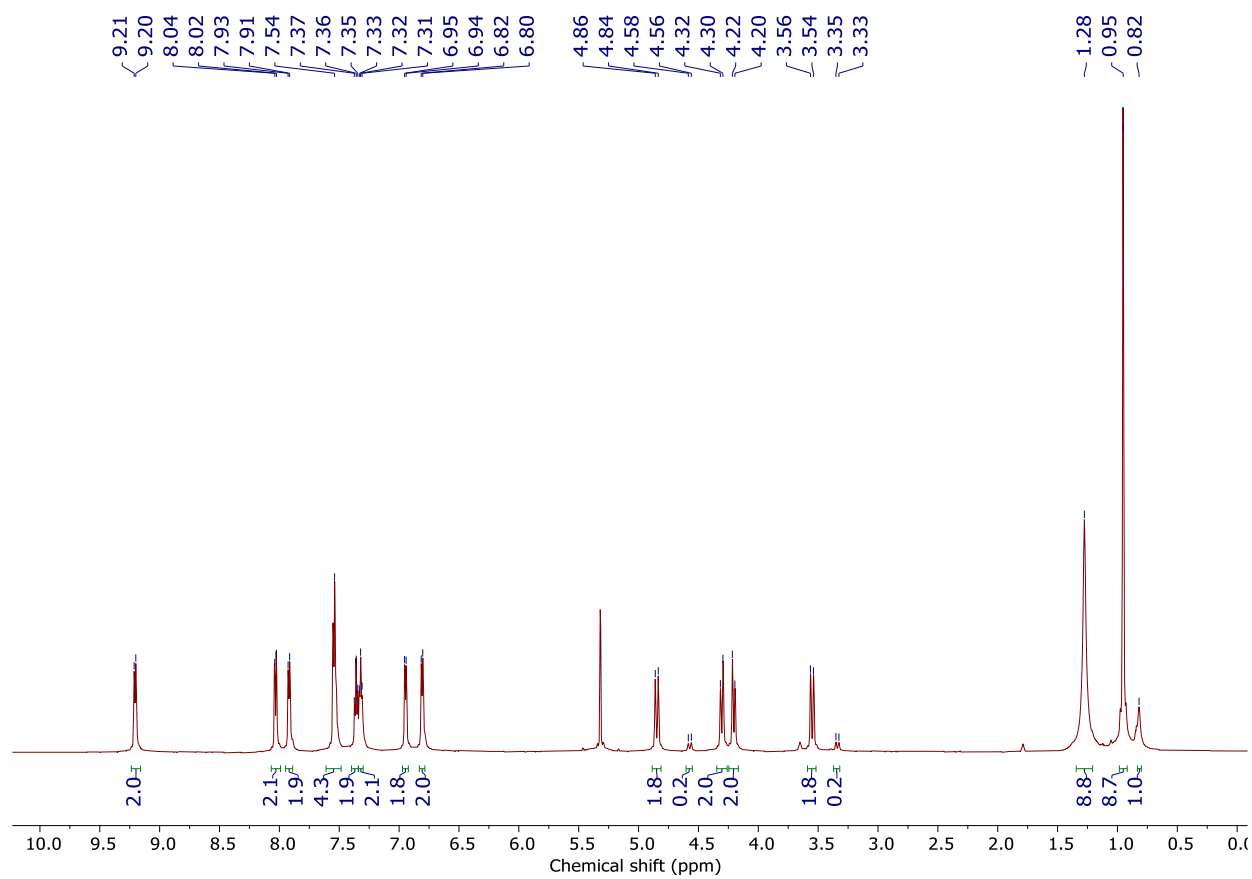
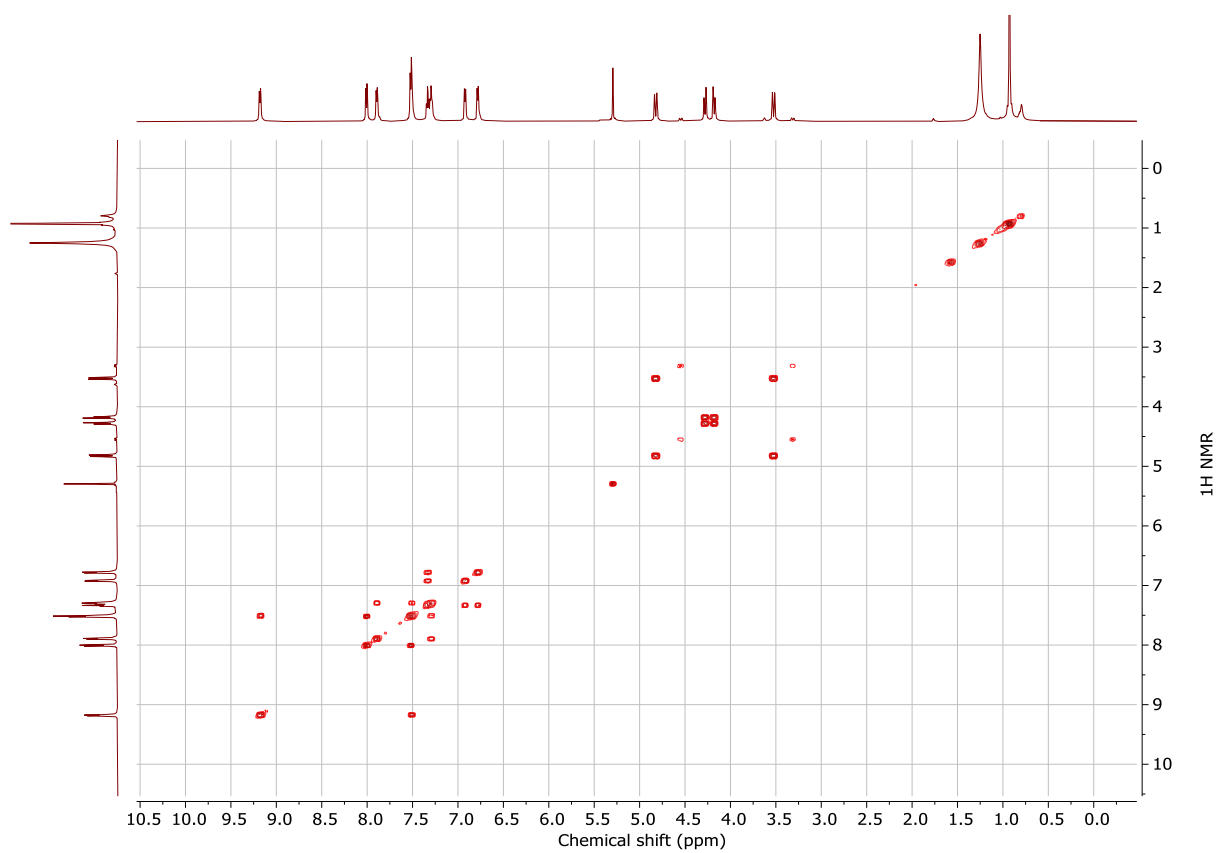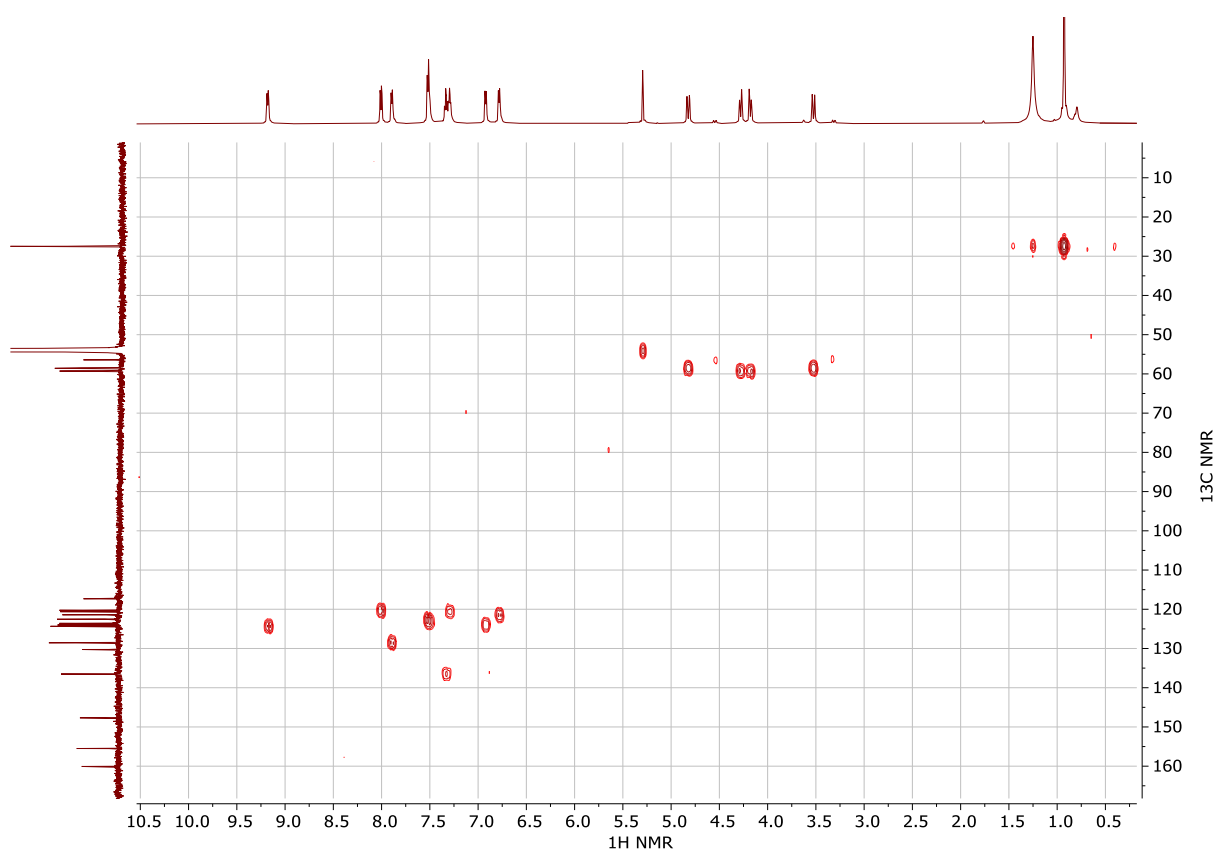**Figure S20.** ^{1}H NMR (600 MHz) spectrum of complex **4** in CD_2Cl_2 at -30 °C.

Figure S21. Variable temperature ^{1}H NMR (600 MHz) spectra of complex **4** in CD_2Cl_2.

Figure S22. $^{13}C\{^1H\}$ NMR (151 MHz) spectrum of complex **4** in CD_2Cl_2 at -30 °C.

Figure S23. ^1H-^1H COSY spectrum of complex **4** in CD_2Cl_2 at -30 °C.

Figure S24. ^1H-^{13}C HMQC spectrum of complex **4** in CD_2Cl_2 at -30 °C.
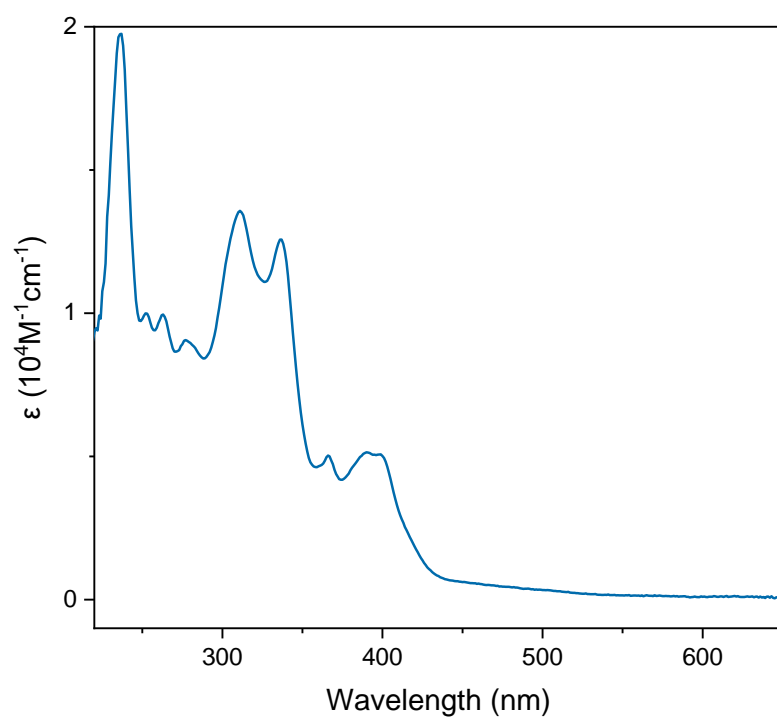
Figure S25. UV-Vis absorption spectrum of complex **4** in THF.
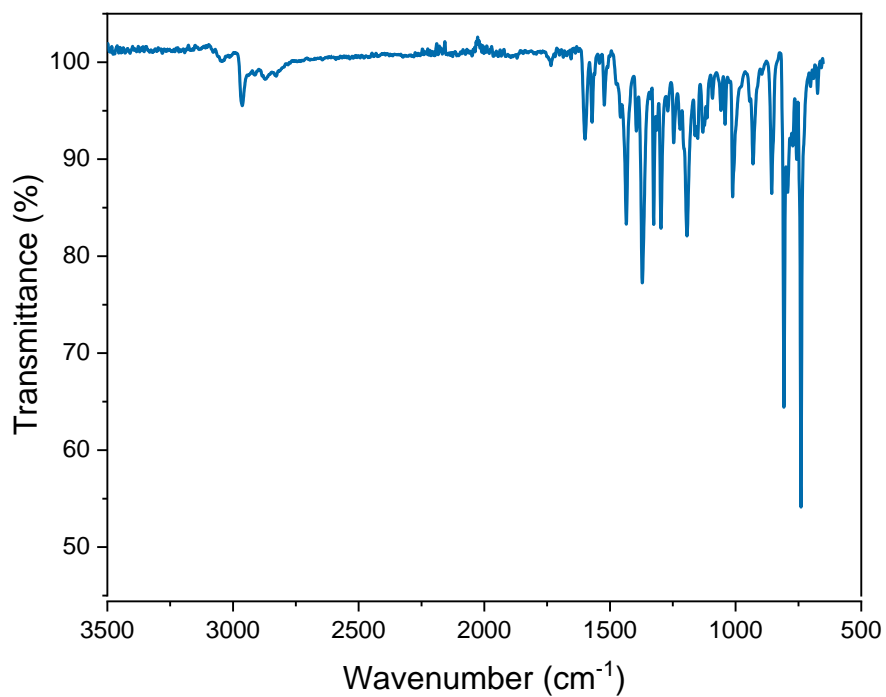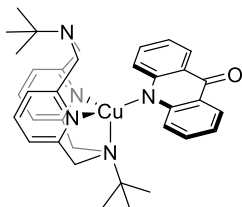
Figure S26. FT-IR spectrum of complex **4**.
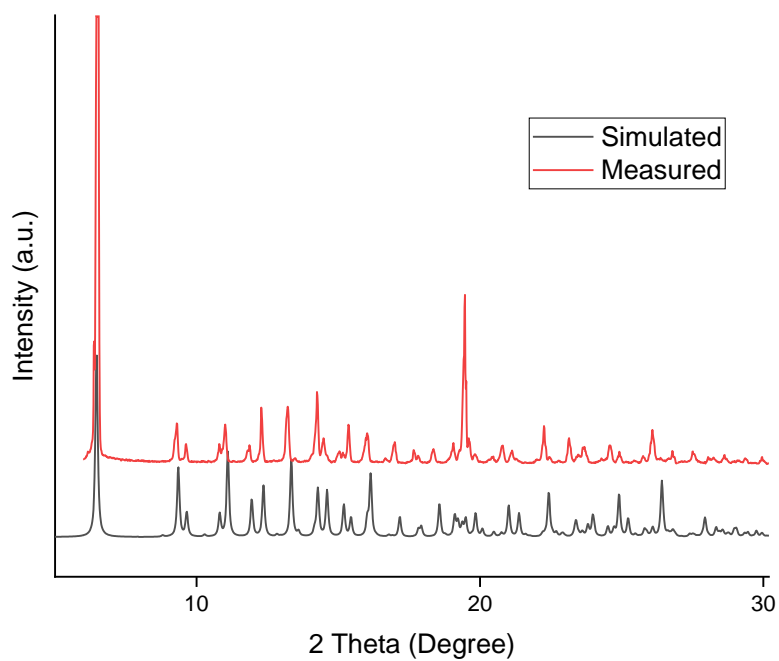
Figure S27. Powder X-ray diffraction patterns of κ^3-**4** (simulated from XRD structure shown in Figure S75).
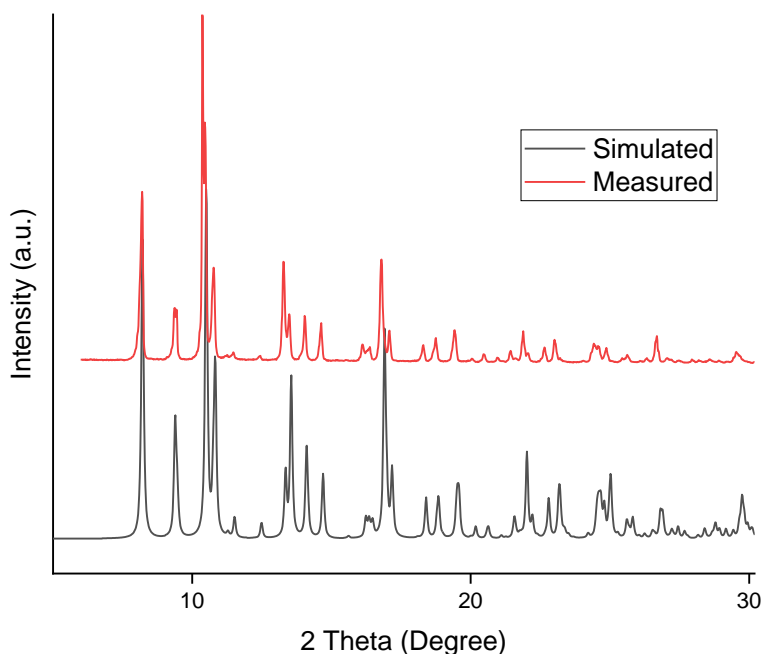
Figure S28. Powder X-ray diffraction patterns of κ^4-**4** (simulated from XRD structure shown in Figure S76).

Synthesis of [(^{tBu}N4)Cu(acridone)] (5)

5

Copper bromide (19.2 mg, 0.134 mmol) and **L1** (41.8 mg, 0.119 mmol) were suspended in 2.5 mL of THF. The mixture was stirred for 1.5 hours at room temperature to give an orange solution. Acridone (24.1 mg, 0.123 mmol), then potassium *tert*-butoxide (14.1 mg, 0.126 mmol), and 6 mL of THF were added and the mixture was left stirring overnight at room temperature. The mixture was filtered through celite to remove the remaining potassium bromide. The resulting solution was concentrated under reduced pressure, and orange crystals were grown by vapor diffusion with diethyl ether to the THF solution of the product, then the crystals were further grown in refrigerator at -30 °C. 53.3 mg, 0.0873 mmol, 73% yield.

^{1}H NMR of κ^3-**5** (600 MHz, -30 °C, CD$_2$Cl$_2$), δ: 8.42 (dd, J_{HH} = 8.3 Hz, 1.6 Hz, 2H, C^1-H (Acrd)), 8.34 (d, $^3J_{HH}$ = 8.8 Hz, 2H, C^4-H (Acrd)), 7.37-7.32 (m, 4H),7.01 (t, $^3J_{HH}$ = 7.3 Hz, 2H, C^2-H (Acrd)), 6.92 (d, $^3J_{HH}$ = 7.7 Hz, 2H, *m*-H$_{py}$), 6.79 (d, $^3J_{HH}$ = 7.6 Hz, 2H, *m*-H$_{py}$), 4.83 (d, $^3J_{HH}$ = 14.8 Hz, 2H, CH$_2$), 4.28 (d, $^3J_{HH}$ = 12.5 Hz, 2H, CH$_2$), 3.92 (d, $^3J_{HH}$ = 12.5 Hz, 2H, CH$_2$ CH$_2$), 3.55 (d, $^3J_{HH}$ = 14.8 Hz, 2H, CH$_2$), 1.27 (s, 9H, H$_{tBu}$), 0.99 (s, 9H, H$_{tBu}$).

Peaks at 7.29 ppm (triplet, $J = 7.7$ Hz), 6.75 ppm (doublet, $J = 7.6$ Hz), 4.53, 3.32 ppm (doublets, $J = 14.8$ Hz) and 0.84 ppm (singlet) are assigned to a symmetrical (κ^4-N4)Cu(acridonate); the estimated ratio of $\kappa^3 : \kappa^4$ isomers is 14 : 1 at -30 °C.

^{13}C{^{1}H} NMR of κ^3-**5** (151 MHz, -30 °C, CD$_2$Cl$_2$): δ 176.9 (quat. C$_{Ar}$), 159.8 (quat. C$_{Ar}$), 155.0 (quat. C$_{Ar}$), 150.6 (quat. C$_{Ar}$), 136.7 (p-C$_{py}$), 130.1 (C^3 (Acrd)), 126.7 (C^4 (Acrd)), 126.1 (C^1 (Acrd)), 124.2 (m-C$_{py}$), 121.5 (m-C$_{py}$), 117.8 (C^2 (Acrd)), 59.1 (CH$_2$), 58.7 (CH$_2$), 56.3 (quat. C(CH$_3$)$_3$), 27.3 (C(CH$_3$)$_3$).

UV-Vis (THF), λ, nm (ε, M$^{-1}\times$cm^{-1}): 225 (23000), 252 (27000), 274(26000), 304(7500), 336(7400), 334(11000), 434(6500), 453(6900).

Anal. Found (calcd for C$_{35}$H$_{40}$Cu$_1$N$_5$O$_1$): C, 68.64 (66.88), H, 6.63 (6.61), N, 11.34 (11.48).
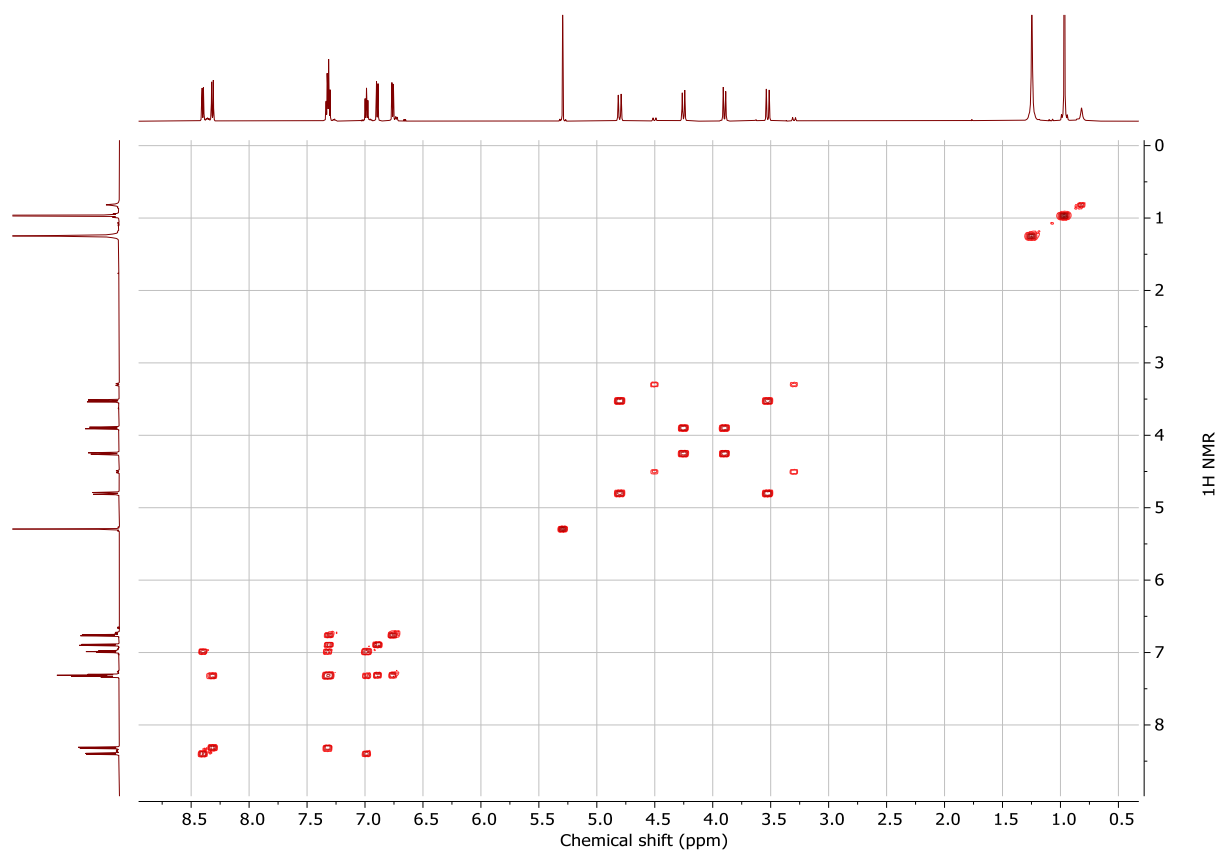
FT-IR (ATR, solid): υ 662, 678, 730, 757, 800, 812, 853, 890, 900, 923, 939, 1006, 1021, 1055, 1074, 1094, 1150, 1191, 1244, 1347, 1369, 1397, 1439, 1468, 1485, 1548, 1576, 1599, 2953, 2965, 3044, 3058.
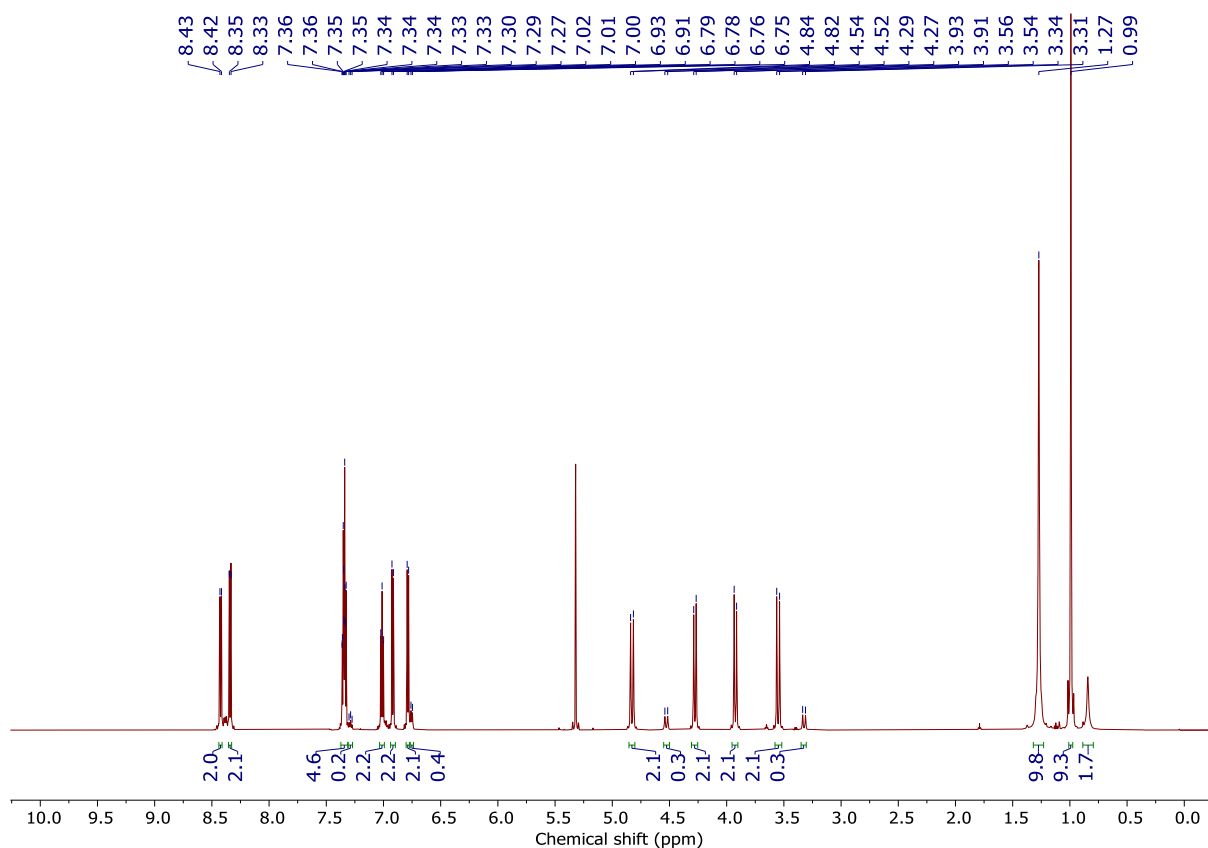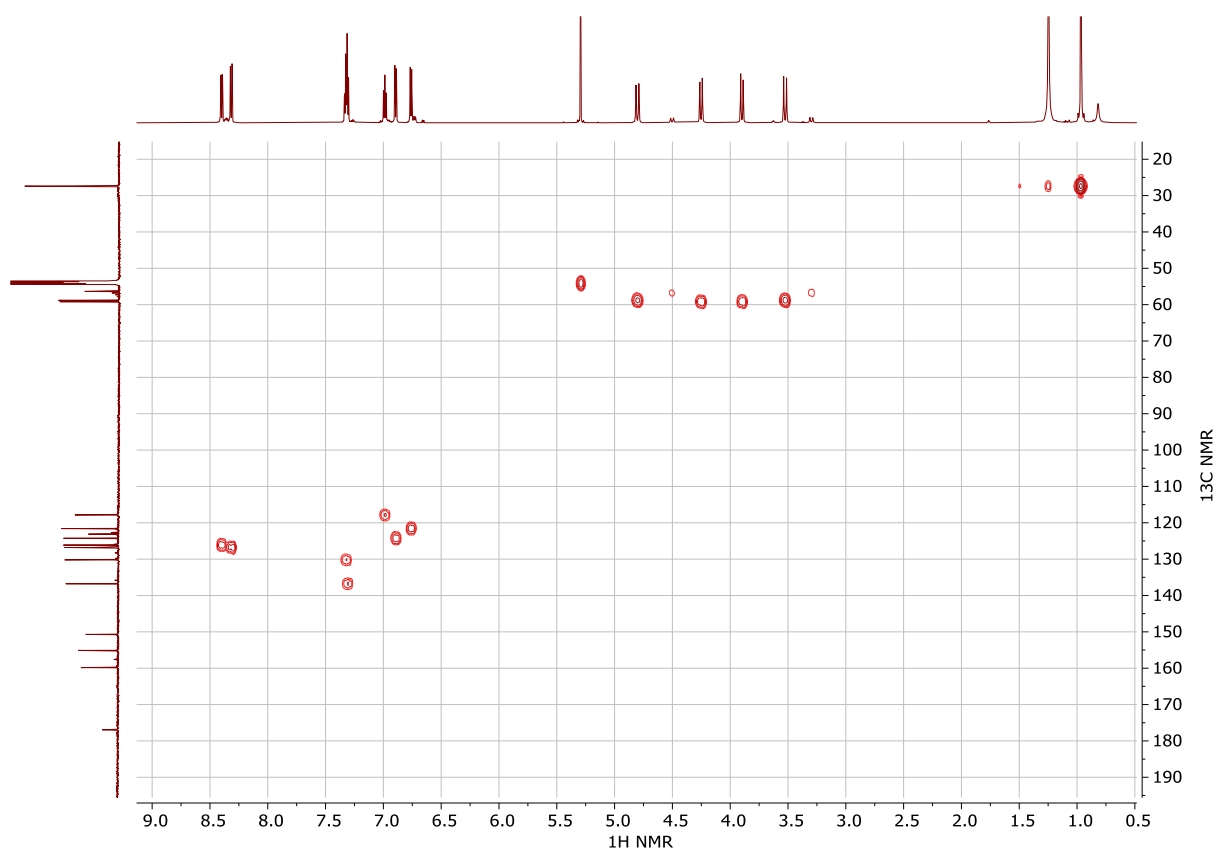

Figure S29. ^{1}H NMR (600 MHz) spectrum of complex **5** in CD$_2$Cl$_2$ at -30 °C.
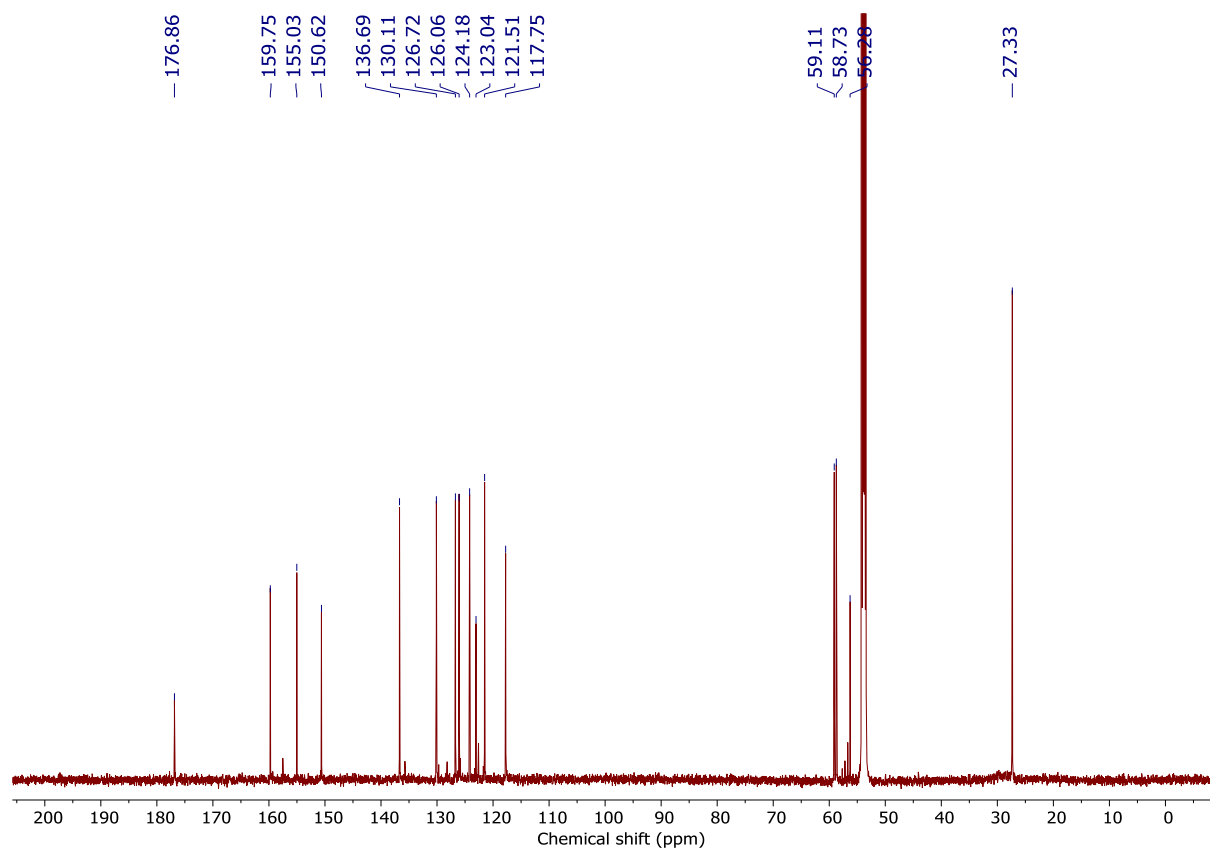
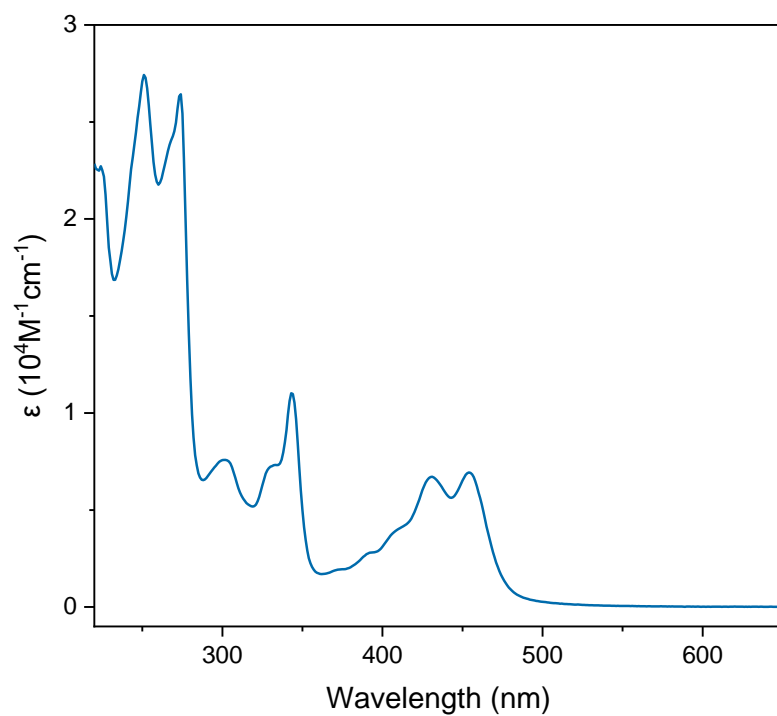**Figure S30**. $^{13}C\{^1H\}$ NMR (151 MHz) spectrum of complex **5** in CD_2Cl_2 at -30 °C.

Figure S31. ^1H-^1H COSY spectrum of complex **5** in CD_2Cl_2 at -30 °C.

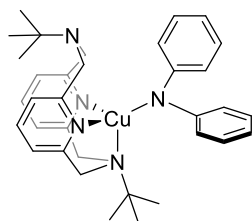**Figure S32**. ^1H-^{13}C HMQC spectrum of complex **5** in CD_2Cl_2 at -30 °C.

Figure S33. UV-Vis absorption spectrum of **5** in THF.
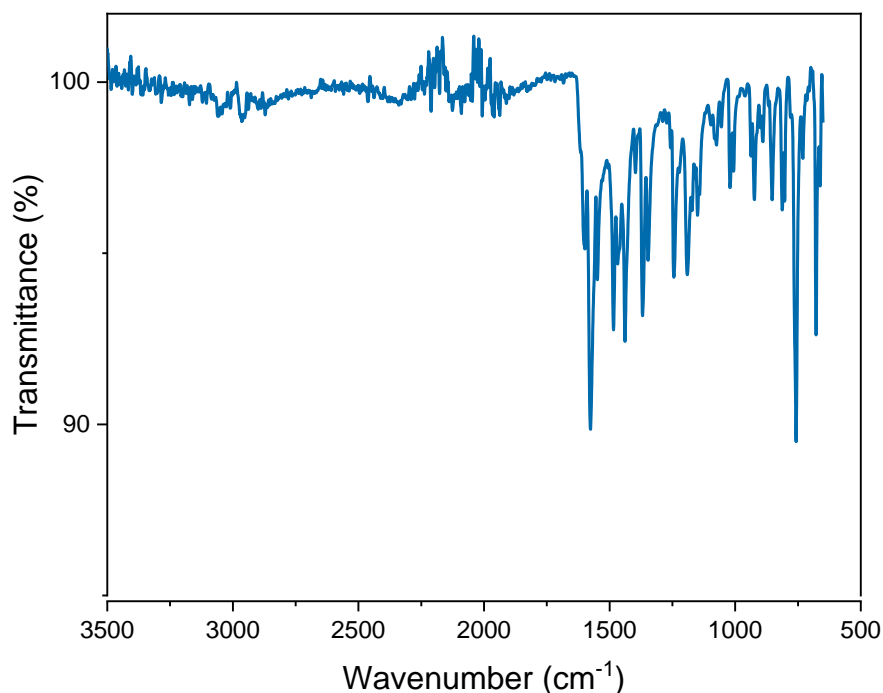
Figure S34. FT-IR spectrum of complex **5**.

Synthesis of [(^{tBu}N4)Cu(NPh$_2$)] (6)

6

Inside a glove box, copper bromide (41.0 mg, 0.286 mmol) and **L1** (101.3 mg, 0.287 mmol) were suspended in 7.5 mL of THF. The mixture was stirred overnight at room temperature to give an orange solution. Diphenylamine (48.2 mg, 0.285 mmol) then potassium *tert*-butoxide (31.9 mg, 0.287 mmol) were added, and the mixture was stirred overnight at room temperature. The mixture was filtered through celite to remove the remaining potassium bromide. After reducing the amount of solvent under vacuum, red crystals were grown by vapor diffusion with diethyl ether to the solution, and subsequently keeping the vial at -30 °C. 116 mg, 0.199 mmol, 70%.

^{1}H NMR (600 MHz, -30 °C, CD$_2$Cl$_2$), δ: 7.22 (t, J_{HH} = 7.6 Hz, 2H, *p*-H$_{py}$), 6.83 (br, 2H, *m*-H$_{py}$), 6.68 (br, 2H, *m*-H$_{py}$), 4.68 (br, 2H, CH$_2$), 4.07 (br, 4H, CH$_2$), 1.44 (s, 9H, H$_{tBu}$), 1.12 (s, 9H, H$_{tBu}$).

*The peaks of phenyl groups and one of the bridging CH$_2$ could not be resolved at this condition.

^{13}C{^{1}H} NMR (151 MHz, -30 °C, CD$_2$Cl$_2$): δ 159.8 (C$_{Ar}$), 159.3 (C$_{Ar}$), 155.0 (C$_{Ar}$), 142.8 (C$_{Ar}$), 135.9 (C$_{Ar}$), 135.0 (C$_{Ar}$), 129.3 (C$_{Ar}$), 128.2 (C$_{Ar}$), 123.8 (C$_{Ar}$), 121.7 (C$_{Ar}$), 121.2 (C$_{Ar}$), 117.3 (C$_{Ar}$), 58.2 (*C*H$_2$), 57.7 (*C*H$_2$), 56.2 (*C*H$_2$), 55.7 (quat. *C*(CH$_3$)$_3$), 27.6 (C(*C*H$_3$)$_3$).

UV-Vis (THF), λ, nm (ε, M^{-1}×cm^{-1}): 256 (17000), 284(18000), 367(21000), 531(440).

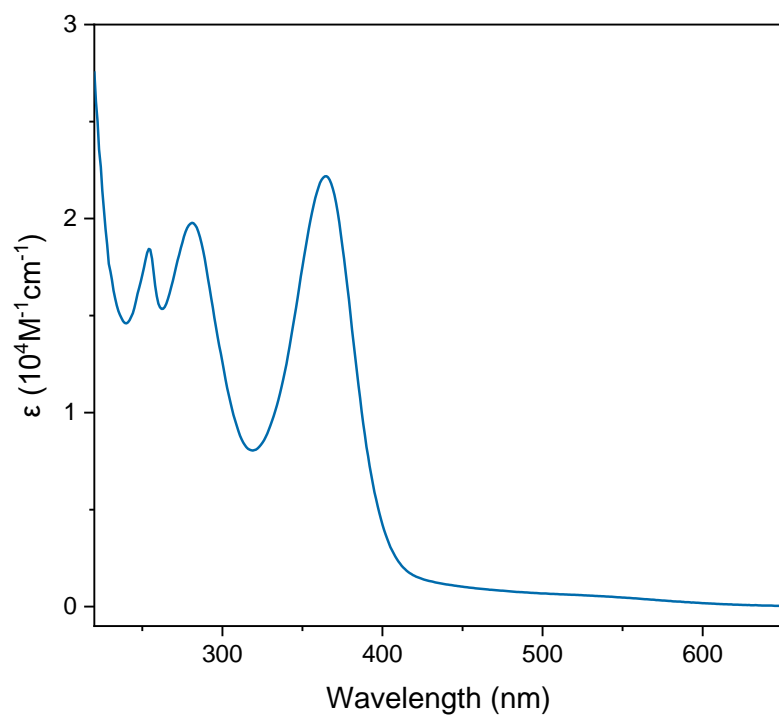Anal. Found (calcd for $C_{42}H_{56}Cu_1N_5$): C, 69.68 (69.89), H, 7.50 (7.25), N, 11.86 (11.99).

FT-IR (ATR, solid): υ 691, 741, 756, 805, 846, 860, 887, 913, 924, 985, 1006, 1022, 1058, 1069, 1080, 1080, 1149, 1163, 1176, 1190, 1214, 1265, 1294, 1319, 1329, 1366, 1392, 1460, 1570, 1594.
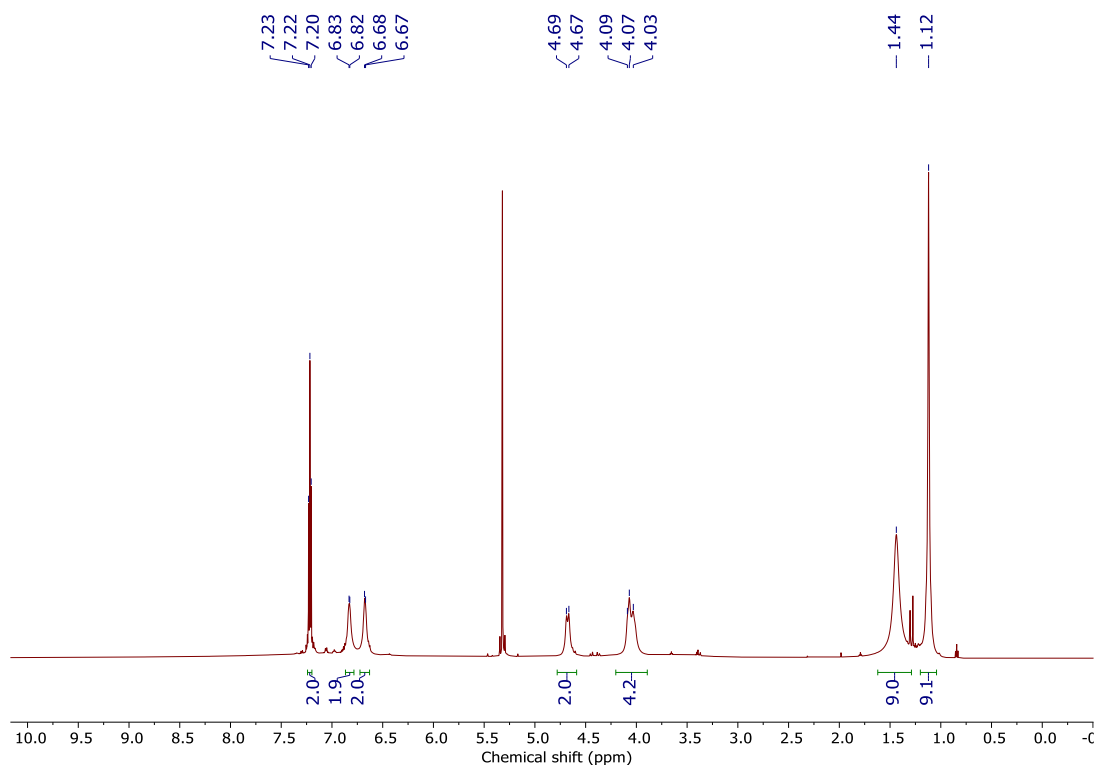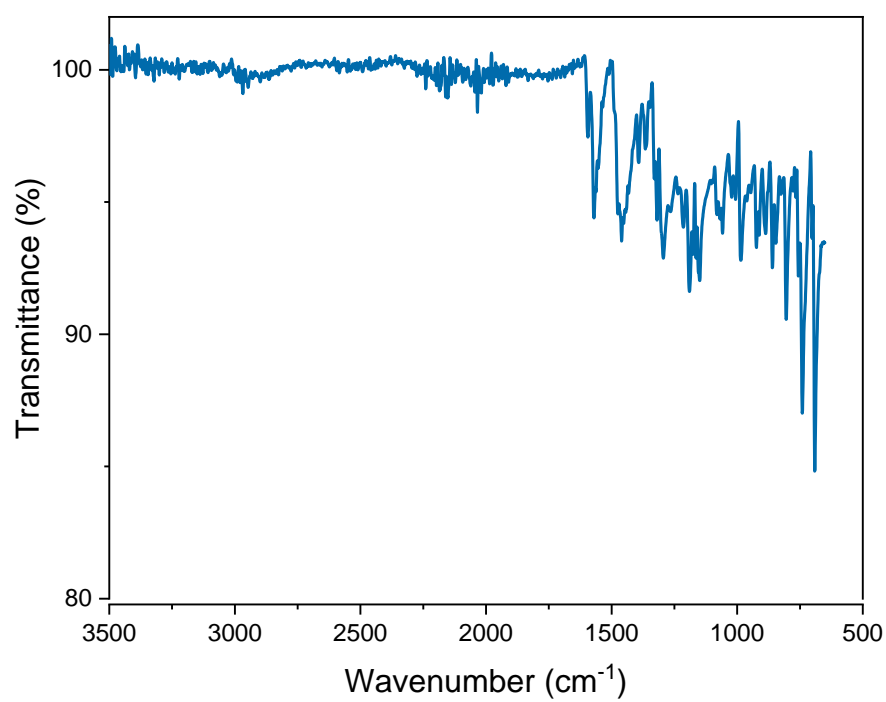

Figure S35. ^{1}H NMR (600 MHz) spectrum of complex **6** in CD_2Cl_2 at -30 °C.
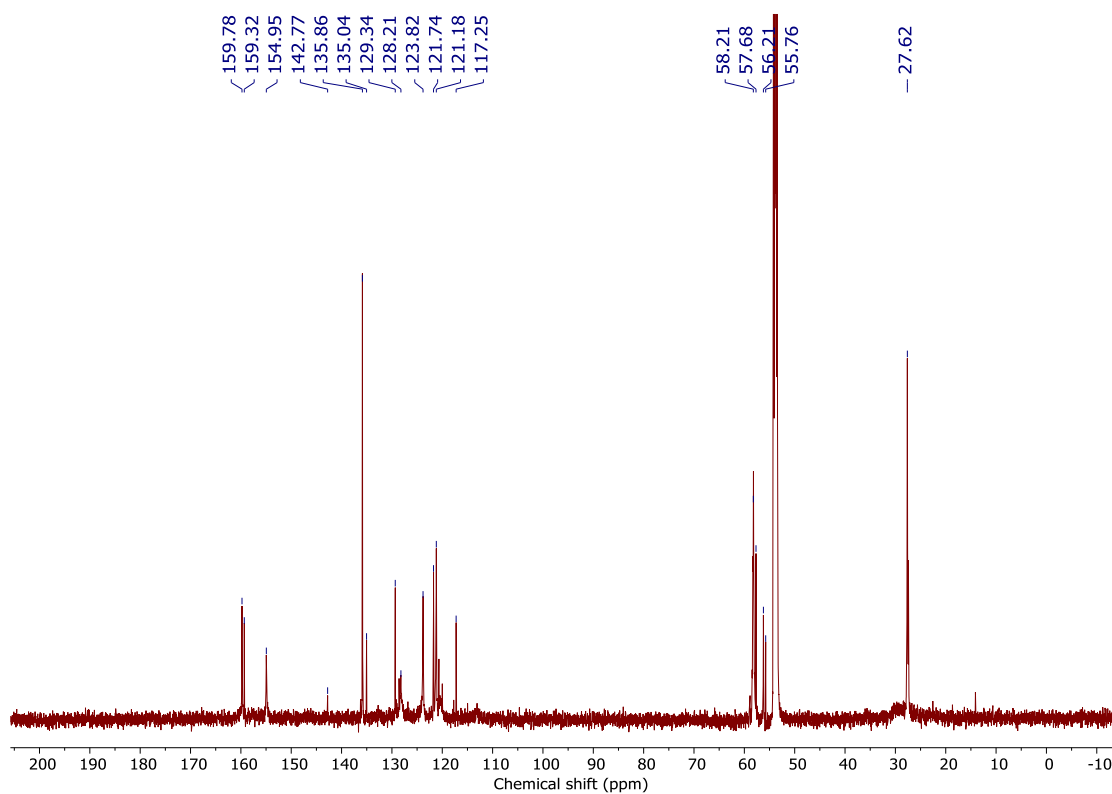
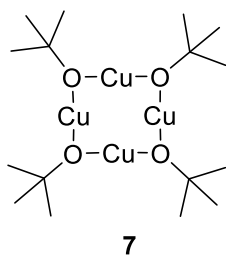**Figure S36**. ^{13}C{^{1}H} NMR (151 MHz) spectrum of complex **6** in CD_2Cl_2 at -30 °C.

Figure S37. UV-Vis absorption spectrum of **6** in THF (10^{-5} M).

Figure S38. FT-IR spectrum of complex **6**.

Synthesis of [Cu$_4$(O^{t}Bu)$_4$] (7)

7

Synthesis of [Cu$_4$(O^{t}Bu)$_4$] was performed based on the previously reported method[5] with modifications (**Method 1**), and by an alternative method to give the analogous product (**Method 2**).

Potassium *tert*-butoxide was purified by sublimation (200 mTorr, 200 °C) and THF was dried over 4 Å molecular sieves prior to use.

Method 1. Copper chloride (500 mg, 5.05 mmol) was suspended in 10 mL of THF, and a solution of potassium *tert*-butoxide (285 mg, 2.54 mmol) was added to the stirred mixture dropwise. The mixture was stirred at room temperature overnight. The solvent was removed under vacuum and the crude product was purified by sublimation (100 mTorr, 200 °C) to give light brown crystalline solid (140.9 mg, 0.258 mmol, 41%)

Method 2. Copper chloride (214 mg, 2.16 mmol) was suspended in 5 mL of THF, and a solution of potassium *tert*-butoxide (240 mg, 2.14 mmol) was added to the stirred mixture dropwise. The mixture was stirred at room temperature for 1 hour, filtered, then the solvent was removed under vacuum to give yellow-white powder, which was used for the following reactions without further purification. 206 mg, 0.377 mmol, 70% yield.

To confirm the structure, the obtained powder was dissolved in benzene and pale yellow crystals were grown by vapor diffusion with ether to the solution at -30 °C. The crystals were confirmed to be identical with the previously reported structure[6] by X-ray diffraction analysis.

^{1}H NMR (400 MHz, 23 °C, C$_6$D$_6$): δ (ppm): 1.30 (s, 9H).

Synthesis of [Cu$_4$(Cbz)$_4$] (8)

8
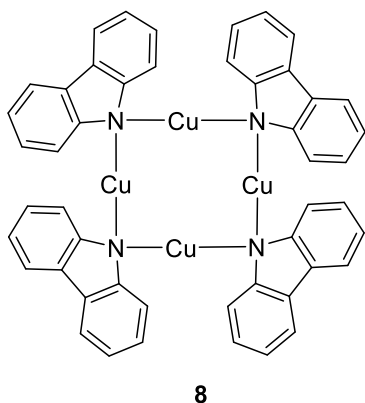
[Cu$_4$(O^{t}Bu)$_4$] (**7**) (64.6 mg, 0.118 mmol) was dissolved in 5 mL of THF, and a solution of carbazole (80.6 mg, 0.482 mmol) in 5 mL of THF was added to the stirred mixture dropwise. The solution was stirred at room temperature 1 h, then the amount of the solvent was under vacuum to ca 3 mL. The

solution was filtered and set for vapor diffusion with diethyl ether to give yellow-white crystalline powder. 67.1 mg, 0.0730 mmol, 61% yield.

Crystals suitable for X-ray analysis were obtained during the initial attempts to obtain **8** by reaction of [Cu(MeCN)$_4$]BF$_4$ and carbazole with base, then vapor diffusion of the acetonitrile solution to ether. Due to the difficulty to grow large crystals, crystals suitable for X-ray analysis further could not be obtained. Therefore, the yellow-white crystalline powder obtained in the reaction starting form compound **7** was characterized by powder XRD analysis, and confirmed to be the desired product.

^{1}H NMR (400 MHz, 23 °C, acetone-d_6), δ (ppm): 8.12 (d, $^3J_{HH}$ = 7.8 Hz, 4H, C^4-H (Cz)), 7.51 (d, $^3J_{HH}$ = 8.0 Hz, 4H, C^1-H (Cz)), 7.38 (t, $^3J_{HH}$ = 7.8 Hz, 4H, C^3-H (Cz)), 7.17 (t, $^3J_{HH}$ = 7.8 Hz, 4H, C^2-H (Cz)).
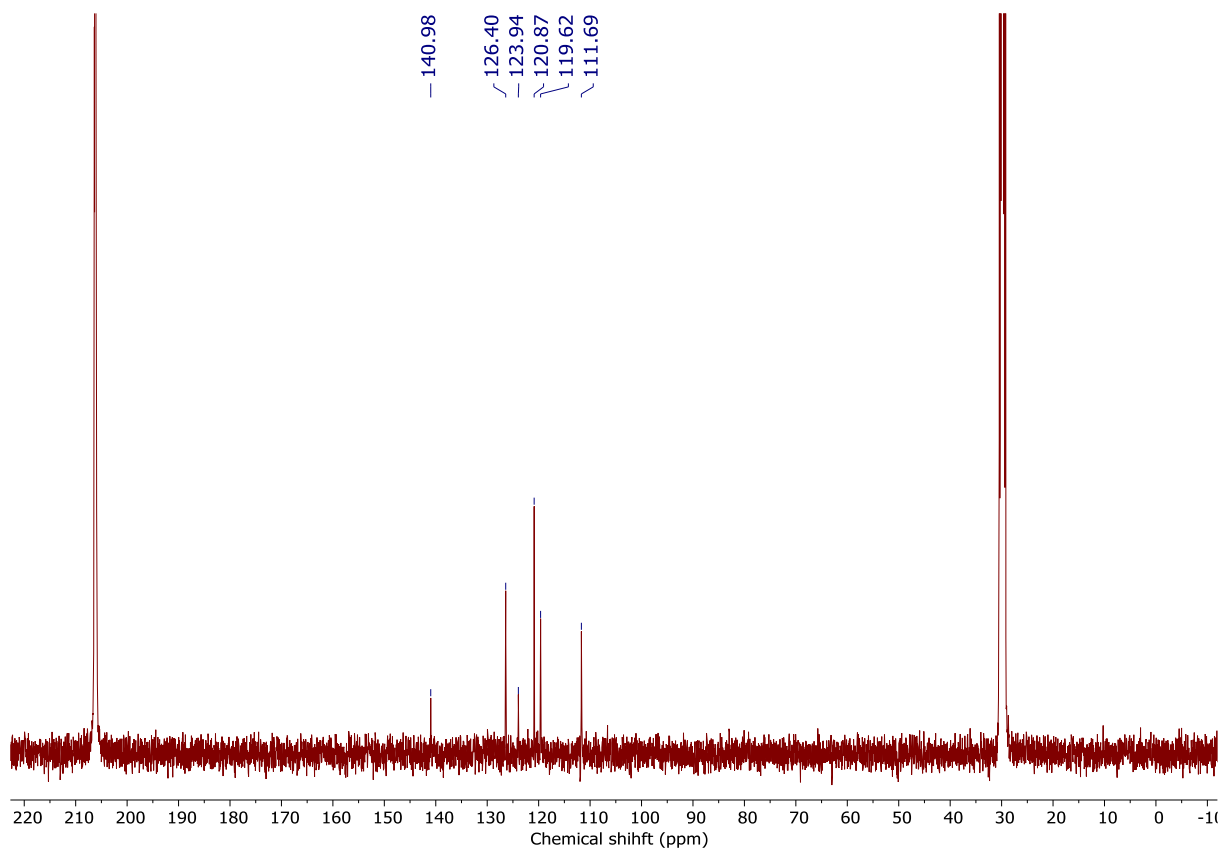
^{13}C{^{1}H} NMR (100 MHz, 23 °C, acetone-d_6), δ (ppm): 140.1, 126.4, 123.9, 120.9, 119.6, 111.7.

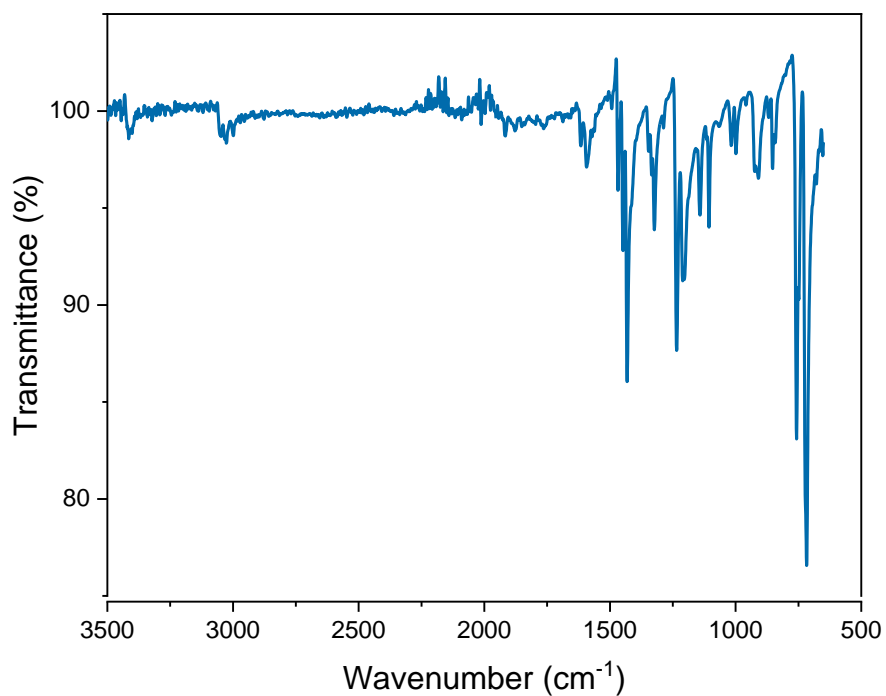Anal. Found (calcd for C$_{42}$H$_{56}$Cu$_1$N$_5$): C, 62.43 (62.73), H, 3.41 (3.51), N, 5.91 (6.10).

FT-IR (ATR, solid): υ 717, 757, 852, 909, 999, 1017, 1067, 1106, 1142, 1211, 1234, 1323, 1432, 1448, 1468, 1493, 1593, 1616, 1878, 1916, 2013, 3026, 3048, 3415.
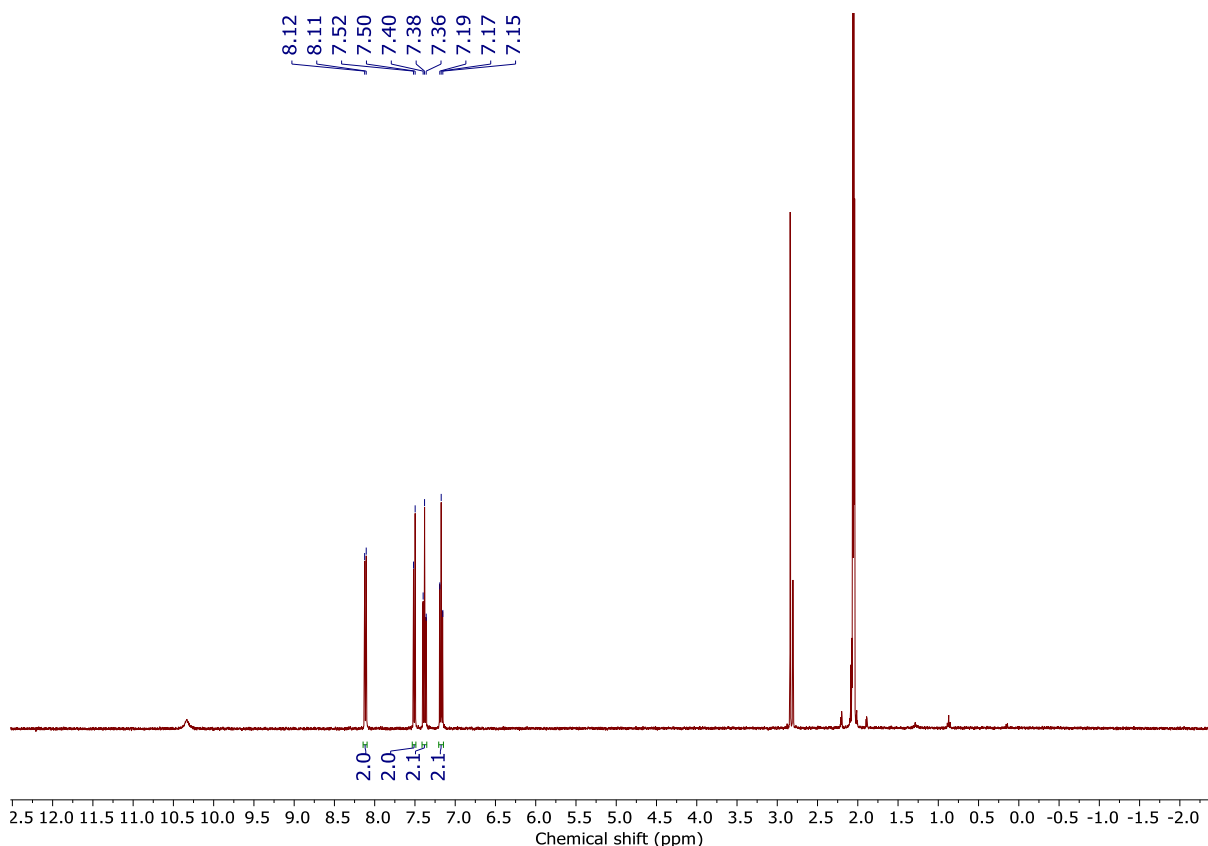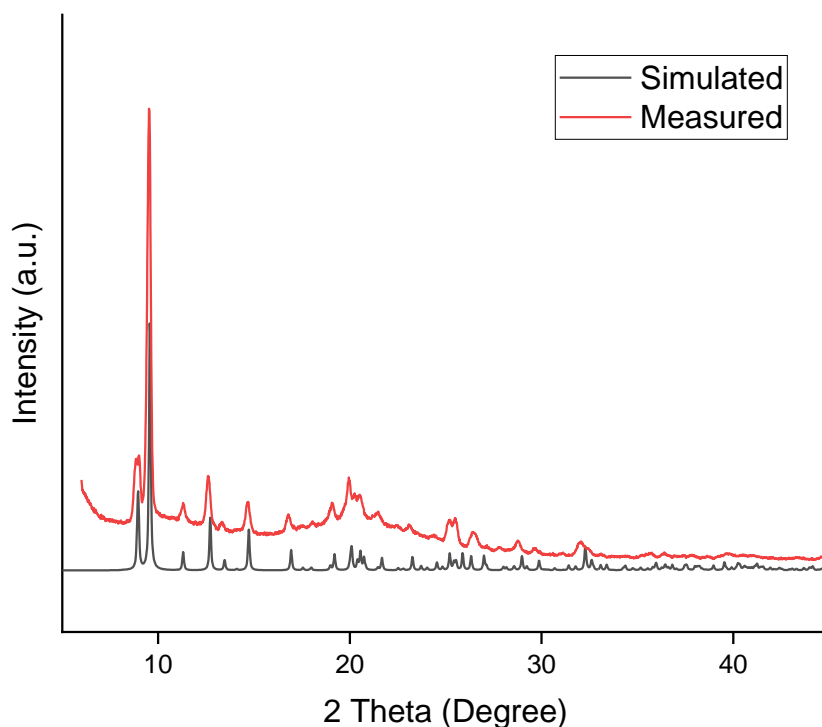

Figure S39. ^{1}H NMR (400 MHz) spectrum of [Cu$_4$(Cbz)$_4$] (**8**) in acetone-d_6 at 23 °C.

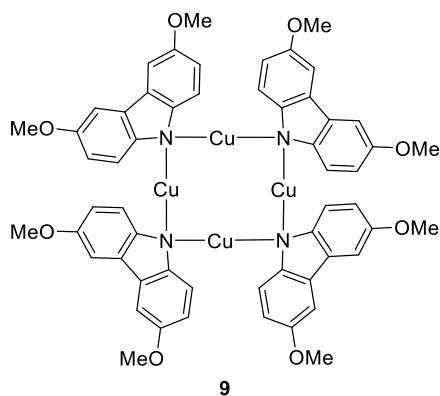**Figure S40**. ^{13}C NMR {1H} (100 MHz) spectrum of [Cu$_4$(Cbz)$_4$] (**8**) in acetone-d_6 at 23 °C.

Figure S41. FT-IR spectrum of compound **8**.

Figure S42. Powder X-ray diffraction patterns of **8**.
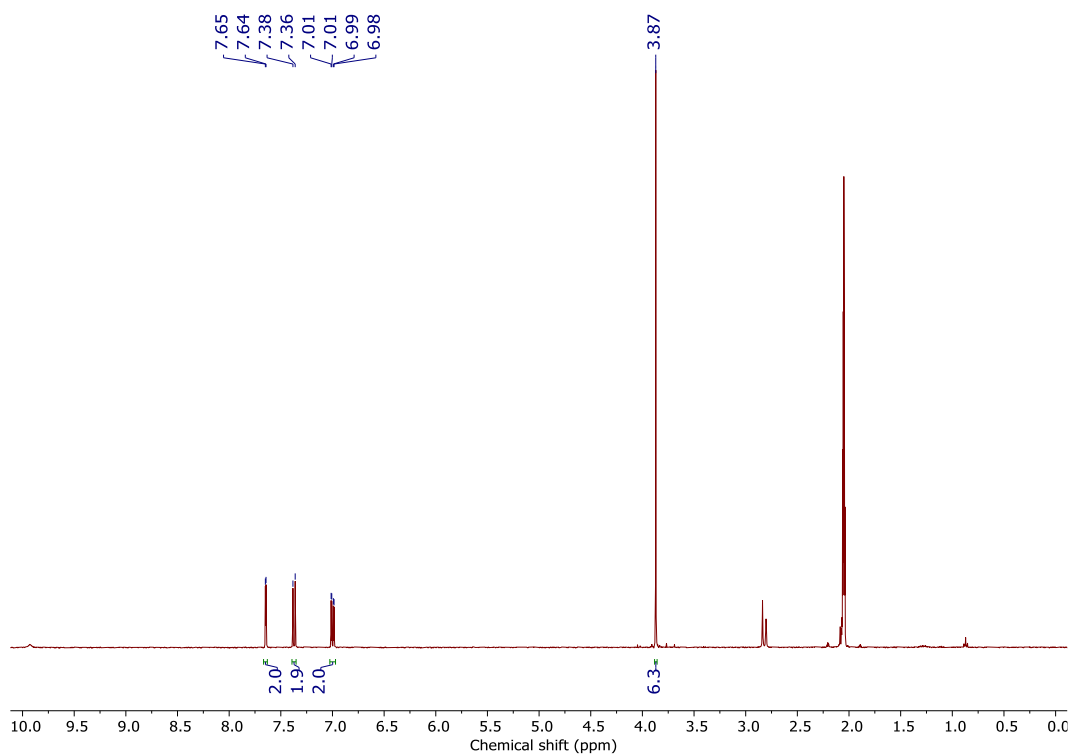
Synthesis of [Cu4($^{\text{MeO2}}$Cbz)4] (9)

9

[Cu₄(OᵗBu)₄] (**7**) (57.0 mg, 0.104 mmol) was dissolved in 3 mL of THF, and a solution of 3,6-dimethoxy-9H-carbazole (94.8 mg, 0.417 mmol) in 3 mL of THF was added to the stirred mixture dropwise. The solution was stirred at room temperature at 2h, then the solvent was removed at reduced pressure. The crude mixture was purified by vapor diffusion with THF/diethyl ether to give the product as pale yellow crystals (66.5 mg, 0.0573 mmol, 55%) Crystals suitable for X-ray diffraction measurement were obtained from vapor diffusion with dichloromethane/diethyl ether.

^{1}H NMR (400 MHz, 23 °C, acetone-d_6), δ (ppm): 7.65 (d, $^{4}J_{\text{HH}}$ = 2.5 Hz, 2H, C^{4}-H (Cz)), 7.37 (d, $^{3}J_{\text{HH}}$ = 8.8 Hz, 2H, C^{1}-H (Cz)), 7.00 (dd, $^{3}J_{\text{HH}}$ = 8.8 Hz, $^{4}J_{\text{HH}}$ = 2.5 Hz, 2H, C^{2}-H (Cz)), 3.87 (s, 6H, CH₃).
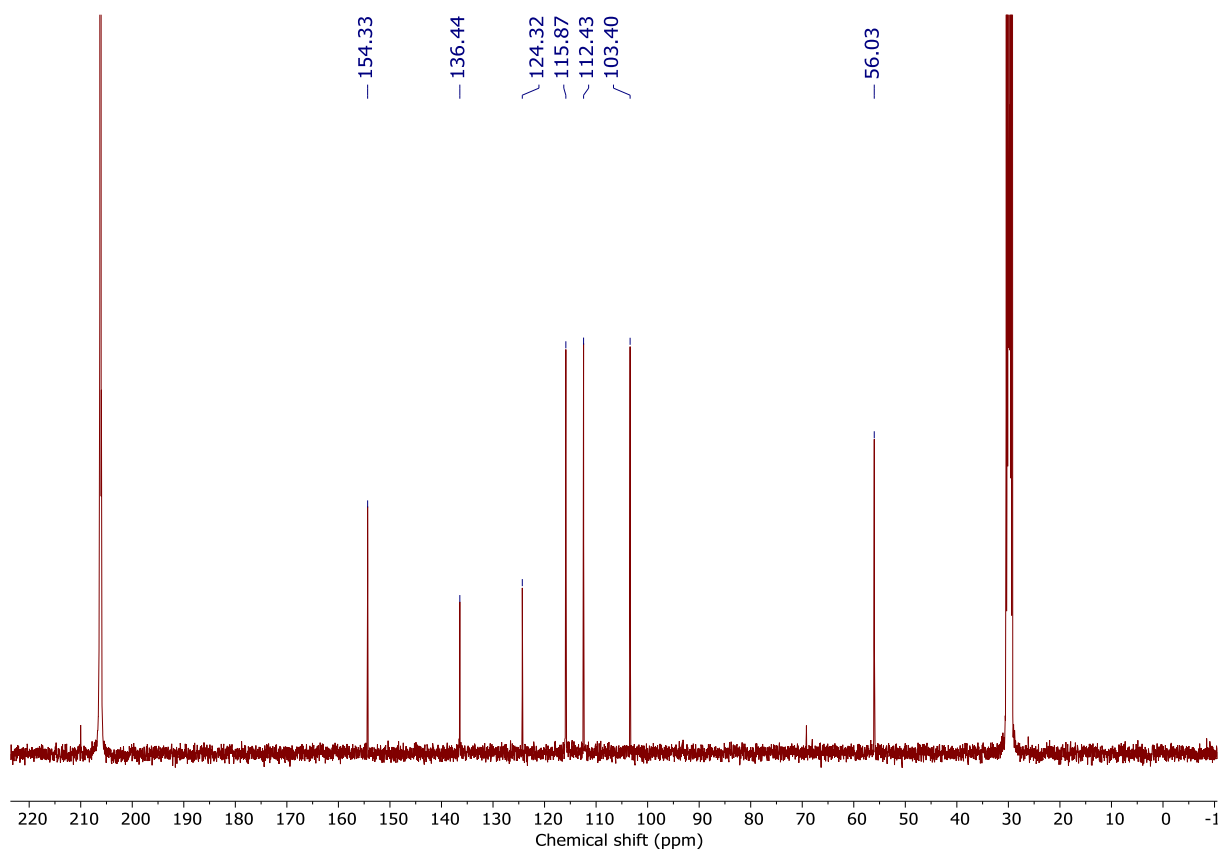
^{13}C{1H} NMR (100 MHz, 23 °C, acetone-d_6), δ (ppm): 154.3, 136.4, 124.3, 115.9, 112.4, 103.4, 56.0.

Anal. Found (calcd for C$_{56}$H$_{48}$Cu$_4$N$_4$O$_8$): C, 57.60 (58.02), H, 4.10 (4.17), N, 4.58 (4.83).

FT-IR (ATR, solid): υ 722, 782, 802, 831, 864, 874, 932, 1026, 1112, 1153, 1172, 1197, 1214, 1249, 1272, 1291, 1313, 1335, 1427, 1452, 1483, 1576, 1603, 2825, 2891, 2928.
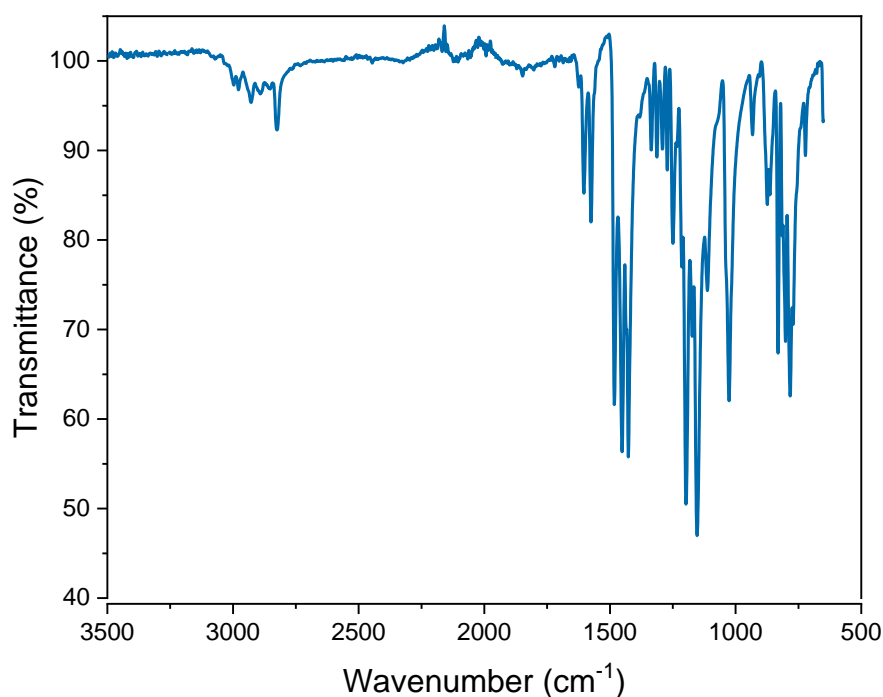

Figure S43. ^{1}H NMR spectrum (400 MHz) of [Cu$_4$(^{MeO2}Cbz)$_4$] (**9**) in acetone-d_6 at 23 °C.
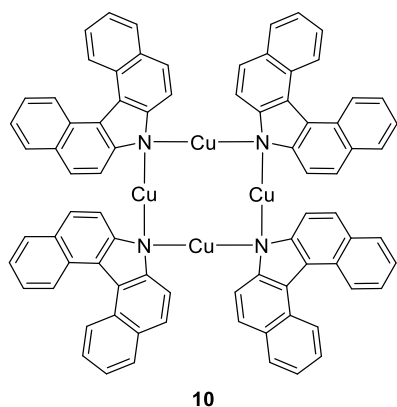
Figure S44. ^{13}C NMR {1H} spectrum (100 MHz) of [Cu$_4$(^{MeO2}Cbz)$_4$] (**9**) in acetone-d_6 at 23 °C.
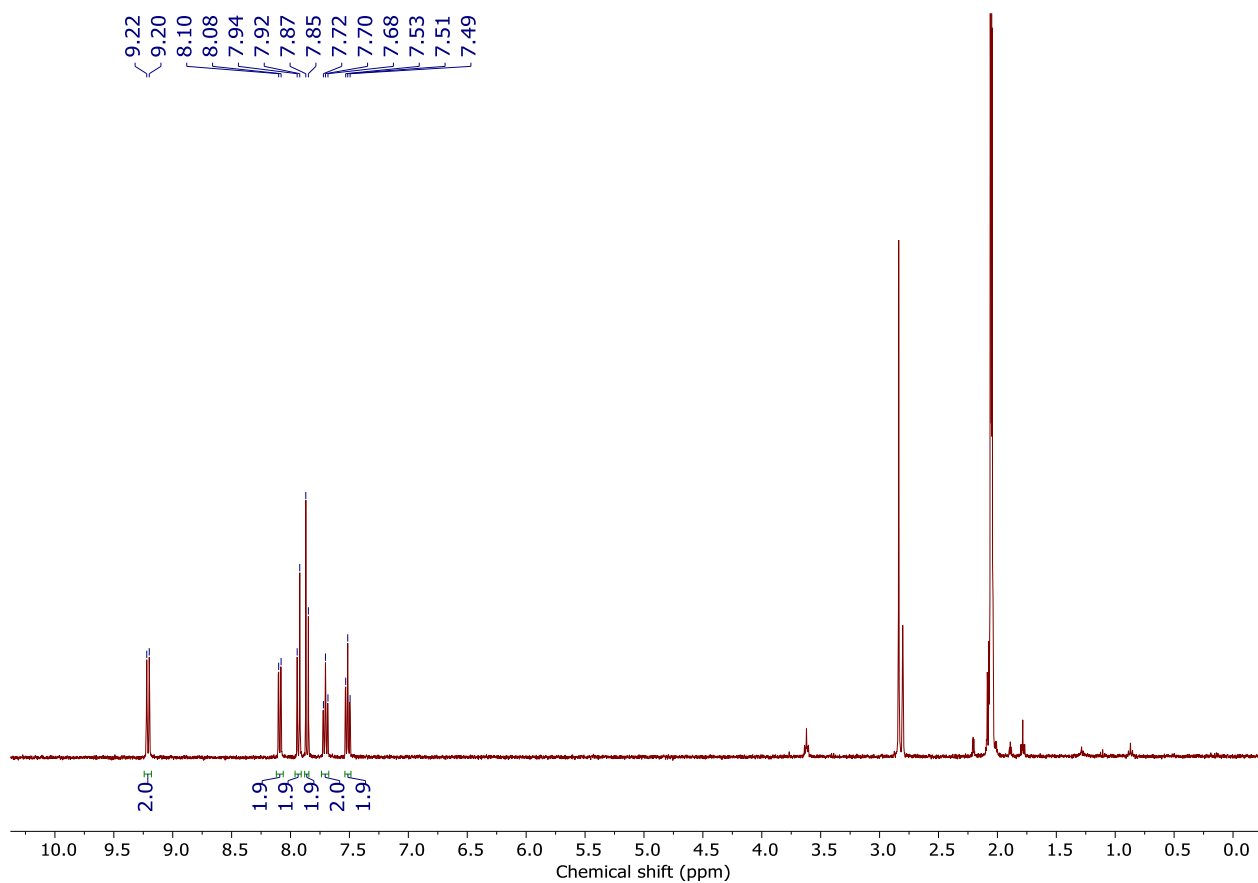

Figure S45. FT-IR spectrum of compound **9**.

Synthesis of [Cu$_4$(^{Bn2}Cbz)$_4$] (10)

10

[Cu$_4$(O^{t}Bu)$_4$] (**7**) (16.0 mg, 0.0293 mmol) was dissolved in 2 mL of THF, and a solution of 7H-dibenzo[c,g]carbazole (32.5 mg, 0.122 mmol) in 3 mL of THF was added to the stirred mixture dropwise. The solution was stirred at room temperature at 2 h. The amount of the solvent was reduced to around 1 mL under reduced pressure. The mixture was filtered purified by vapor diffusion with diethyl ether to give the product as yellow crystals (9.0 mg, 0.0068 mmol, 23%)

^{1}H NMR (400 MHz, 23 °C, acetone-d_6), δ (ppm): 9.21 (d, J_{HH} = 8.5 Hz, 2H, H$_{Ar}$), 8.09 (d, J_{HH} = 8.0 Hz, 2H, H$_{Ar}$), 7.93 (d, J_{HH},= 8.9 Hz, 2H, H$_{Ar}$), 7.86 (d, J_{HH},= 8.7 Hz, 2H, H$_{Ar}$), 7.70 (t, J_{HH},= 7.8 Hz, 2H, H$_{Ar}$), 7.51 (t, J_{HH},= 7.4 Hz, 2H, H$_{Ar}$).

^{13}C{1H} NMR (100 MHz, 23°C, acetone-d_6), δ (ppm): 130.2, 127.4, 126.1, 125.6, 123.9, 114.2.

Figure S46. ^{1}H NMR spectrum (400 MHz) of [Cu$_4$(^{Bn2}Cbz)$_4$] (**10**) in acetone-d_6 at 23 °C.
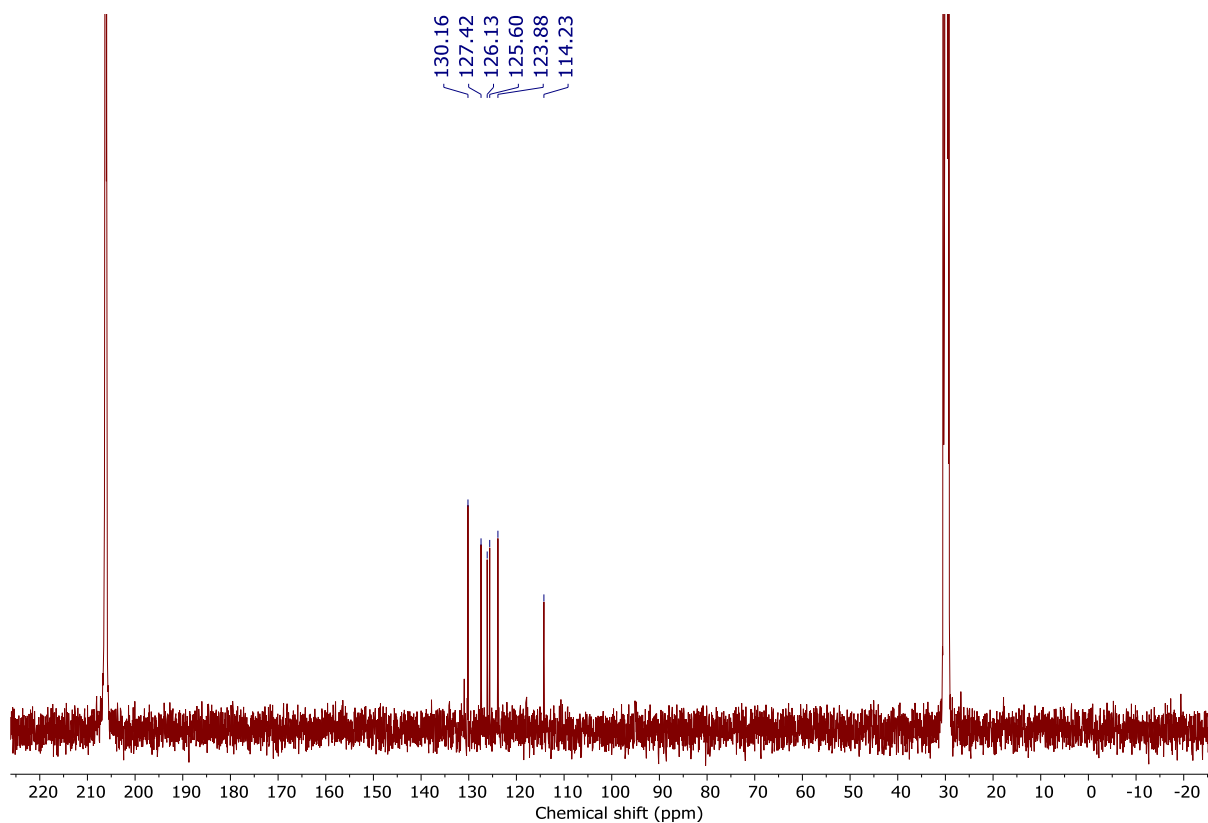
Figure S47. ^{13}C NMR {1H} spectrum (100 MHz) of [Cu$_4$(^{Bn2}Cbz)$_4$] (**9**) in acetone-d_6 at 23 °C.

S38

Synthesis of compound 11
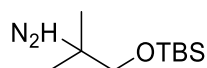
11

In a glove box, sodium hydride (60% in oil, 2.68 g, 67.0 mmol) and THF (150 mL) were placed in 300 mL Schlenk flask. The flask was capped and taken out of glovebox and cooled with an ice bath. 2-Amino-2-methylpropanol (6.0 g, 68 mmol) in dry THF (20 mL) was added slowly over 5 min under argon gas flow with stirring. The reaction mixture was stirred at room temperature for 1 h. A solution of *tert*-butyldimethyl chloride (10.4 g, 69.0 mmol) in dry THF (25 mL) was added to the mixture slowly over 5 min at 0 °C, then the mixture was stirred at room temperature for 3 h. After addition of methanol (5 mL), the reaction mixture was concentrated to *ca.* 25 mL volume under reduced pressure. After addition of hexane (50 mL), the mixture was washed with water (10 mL × 3) and brine (10 mL), dried over magnesium sulfate, filtered off, and concentrated under reduced pressure to give the product as a colorless oil (12.5 g, 61.2 mmol, 91%). This compound was used for the next reaction without further purification.

^{1}H NMR (400 MHz, 23 °C, CDCl$_3$): δ 3.29 (s, 2H, CH$_2$), 1.04 (s, 6H, C-CH$_3$), 0.90 (s, 9H, Si-C-(CH$_3$)$_3$), 0.044 (s, 6H, Si-CH$_3$).

Synthesis of compound 12
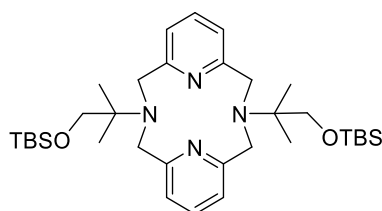
12

The following procedure was performed under air. A solution of 2,6-bis(chloromethyl) pyridine (3.16 g, 18.0 mmol) in acetonitrile (50 mL) was added dropwise over 4 h using a dropping funnel to a mixture of compound **11** (3.69 g, 18.1 mmol), sodium carbonate (11.4 g, 109 mmol), sodium iodide (1.34 g, 8.93 mmol) and acetonitrile (900 mL) with stirring at 80 °C. After stirring at 80 °C for 20h, the hot mixture was filtered off and the amount of solvent was reduced to around 20 mL. The insoluble biproducts were filtered off, and the filtrate was further concentrated under reduced pressure. 30 mL of toluene was added to the mixture, and stirred for 5 min at 110 °C. The insoluble biproducts were filtered off, and the filtrate was kept in the -20 °C freezer to give white crystals (1.6 g). The crystals were dissolved in 40 mL of dichloromethane, then 15.0 g of potassium carbonate was added and the mixture was stirred at room temperature overnight. The mixture was filtered off and the solvent was removed from the filtrate to give the product as white powder (1.30 g, 2.13 mmol, 26%).

^{1}H NMR (400 MHz, 23 °C, CDCl$_3$): δ 7.05 (t, $^3J_{HH}$ = 7.6 Hz, 2H, p-H$_{py}$), 6.72 (d, $^3J_{HH}$ = 7.6 Hz, 4H, m-H$_{py}$), 4.04 (br, 8H, Py-CH$_2$-N), 3.67 (s, 4H, C-CH$_2$-O), 1.28 (s, 12H, N-C-(CH$_3$)$_2$), 0.93 (s, 18H, Si-C(CH$_3$)$_3$), 0.09 (s, 12H, Si-CH$_3$).

Synthesis of compound 13

13
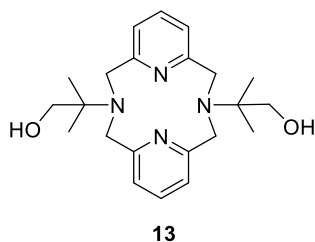
The following procedure was performed under air. Compound **12** (1.30 g, 2.13 mmol) was suspended in 6.6 mL of methanol. After the addition of 35% hydrochloric acid (0.7 mL), the mixture was stirred at room temperature overnight. The solvents were removed under reduced pressure. 10.0 g of potassium carbonate and 15 mL of water were added to the mixture, and the mixture was extracted with dichloromethane (20 mL × 8). The combined organic layers were dried over a mixture of potassium carbonate and magnesium sulfate, filtered off, and concentrated under reduced pressure. 13 mL of toluene was added to the mixture and stirred at 110 ℃ for 5 min. After filtering off the insoluble impurities, the solution was cooled to room temperature then kept in -20 ℃ freezer to give the product as colorless crystals (491 mg, 1.28 mmol, 60%).

^{1}H NMR (400 MHz, 23 °C, CDCl$_3$): δ 7.05 (t, $^3J_{HH}$ = 7.6 Hz, 2H, p-H$_{Py}$), 6.52 (d, $^3J_{HH}$ = 7.6 Hz, 4H, m-H$_{Py}$), 3.94 (s, 8H, Py-CH$_2$-N), 3.56 (s, 4H, C-CH$_2$-O), 1.31 (s, 12H, CH$_3$).


Synthesis of compound L2

L2
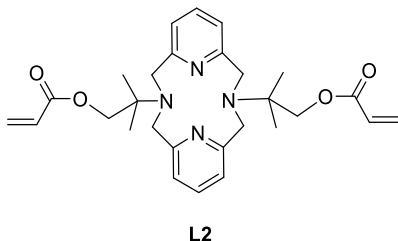
Potassium carbonate (360.8 mg, 2.610 mmol), **L1** (100.4 mg, 0.2613 mmol), and dry dichloromethane (2 mL) were placed in a 25 mL Schlemk flask and stirred at 0 ˚C under inert gas atmosphere. Acrylic anhydride (121 µL, 1.03 mmol) was added to the mixture slowly. The reaction mixture was stirred at room temperature for 3 hours. After the addition of 2.5 mL of methanol at 0 ˚C, the solvents were evaporated under reduced pressure under room temperature. Water (2 mL) and diethyl ether (4 mL) were added to the mixture, and the organic layer was separated. The water layer was extracted by ether (4 mL x3), combined, then dried over magnesium sulfate, and concentrated under reduced pressure to give white powder (83.5 mg, 0.169 mmol, 65%). The obtained product was used immediately for polymerization.

NOTE: The previously reported method described the use of acryloyl chloride for the ligand synthesis. In this modified method, it was replaced with acrylic anhydride to avoid the risks associated with the use of acryloyl chloride related to the possibility of spontaneous decomposition upon prolonged storage and its irritating vapors.

^{1}H NMR (400 MHz, 23 °C, CDCl$_3$): δ 7.07 (t, $^3J_{HH}$ = 7.6 Hz, 2H, *p*-H$_{Py}$), 6.72 (d, $^3J_{HH}$ = 7.8 Hz, 4H, *m*-H$_{Py}$), 6.48 (d, $^3J_{HH}$ = 17.3 Hz, 2H, -C=CH), 6.22 (dd, $^3J_{HH}$ = 17.0 and 10.4 Hz, 2H, -CH=CH), 5.89 (d, $^3J_{HH}$ = 10.3 Hz, 2H, -C=CH), 4.30 (s, 4H, C-CH$_2$-O), 4.07 (br, 8H, Py-CH$_2$-N), 1.39 (s, 12H, C-CH$_3$).

Synthesis of 14
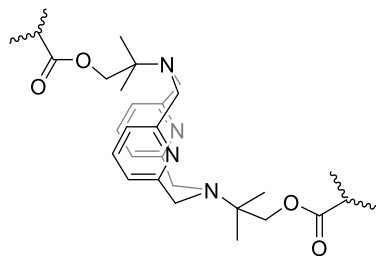
14

〰 : PBA chains with BAB crosslinkers

Toluene (8.2 mL), butyl acrylate (3.8 mL, 27 mmol), **L2** (39.4 mg, 0.0800 mmol) and 1,4-bis(acryloyloxy)butane (BAB) (35 µL, 0.19 mmol) were added to a dried Schlenk tube filled with nitrogen. BAB was added in order to adjust the overall amount of cross-linkers against the monomer. The Schlenk tube was closed and the gases in the solution were removed by three Freeze-Pump-Thaw cycles. Phenylbis(2,4,6-trimethylbenzoyl)phosphine oxide initiator (56.0 mg, 0.134 mmol) was added under a nitrogen gas flow and the solution was transferred to two Teflon molds (40 mm [W] × 50 mm [L] ×10 mm [D], 6 mL each) under inert atmosphere using the purging setup. UV light (395 nm) was irradiated to the molds for 15 min, then the lamp was removed, and the nitrogen flow was kept for additional 1 hour. The molds were left to further polymerize overnight. The films were swollen in hexane, carefully peeled off and taken out from the molds and put inside a hexane-diethyl ether (10:1) solution inside a capped glass bottle. After 2 h, the solvent was replaced. This washing process was repeated three times. The films were further dried in air overnight then under vacuum for 6 h on the Teflon sheet. 2.84 g, 80% (The yield is calculated based on the amount of used starting materials).
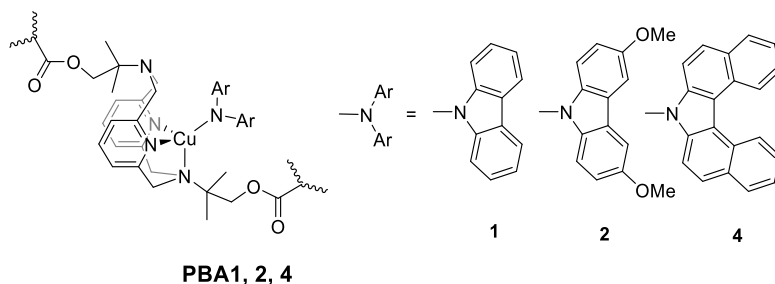
The yield was consistent among multiple batches within 77-81%.

The amount of pyridinophane cross-linkers in **14** (mmol/g) was estimated by;

$$\frac{Amount\ of\ \textbf{\textit{L2}}\ used\ for\ polymerization\ (mmol) \times Yield\ of\ \textbf{14}}{Weight\ of\ obtained\ \textbf{14}\ (g)}$$

The value was consistent among multiple batches within 0.022-0.025 mmol/g.

Preparation of PBA1, 2, 4.
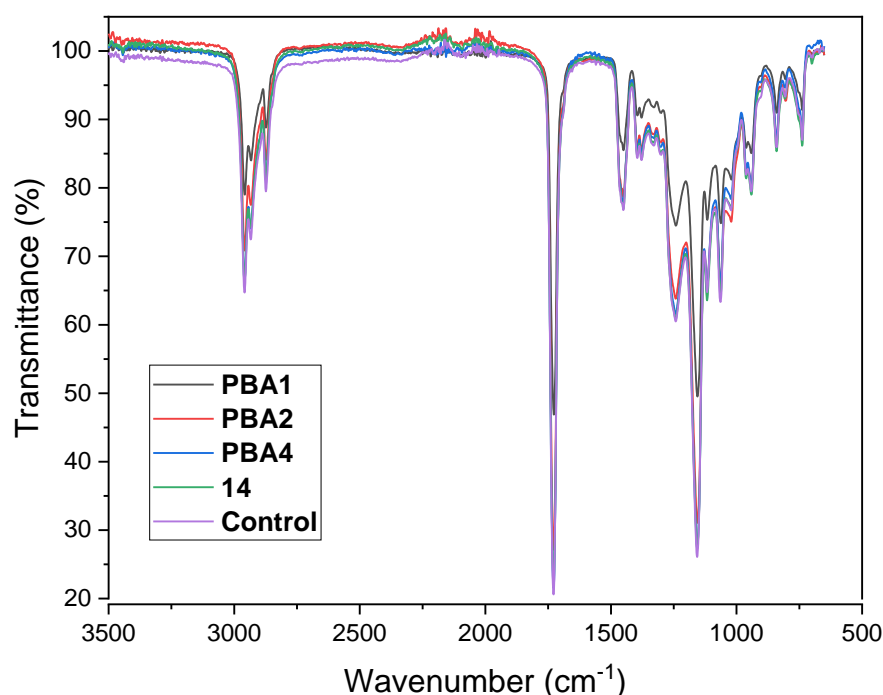

PBA1, 2, 4

1   2   4

Inside a glovebox, PBA films incorporating pyridinophane ligands **L2** as cross-linkers (**14**) (BA:BAB:**L2** = 100 : 0.7 : 0.3) were cut into 25 mm × 10 mm size, weighed out and put in a capped vial. After fully covering the films with THF:pentane 1:10 solution, the films were left to swell for 1 hour. The corresponding copper arylamide precursors (**8**-**10**) were added to the mixture (molar ratio of $Cu_4(NAr_2)_4$: pyridinophane in **14** is 1 : 2 corresponding to molar ratio of one Cu atom per pyridinophane of 2 : 1), and the films were left in the suspension for 2 days. The suspension was removed and fresh THF:pentane 1:10 solution was added, then left for 2 h to wash out the impurities. The washing process was repeated three times. The films were taken out from the solution and dried under vacuum for 2 days on the Teflon sheet.

Preparation of control film (Complex 1 physically blended in PBA film without 14)

The control film physically incorporating complex **1** was prepared to evaluate the effect of the covalent incorporation of copper complex mechanophores.

Cross-linked PBA films without **L2** (BA:BAB = 100 : 1) were prepared using the same procedure as for **14**, without adding **L2**. (87% Yield).

Complex **1** (10.3 mg, 0.0177 mmol) was dissolved in 6 mL of MeCN, then the solution was put on top of the BAB cross-linked PBA film (0.772 g) and let to permeate inside. The process was repeated until all of the solution was absorbed in the film. The film was dried in vacuum for several hours, then rinsed quickly with THF:pentane 1:10 solution to remove the powder of **1** generated on the surface, and further dried in vacuum to give an orange film.

Figure S48. FT-IR spectra of complex films **14, PBA1, 2, 4** and control film.

For all film samples, only peaks related to the poly(butyl-acrylate) matrix were observed due to the low concentration of the Cu cross-linkers.

As an initial attempt to prepare films incorporating the Cu(I) arylamide complexes, the method to first incorporate copper iodide, thus produce films incorporating copper-pyridinophane-iodide complexes as crosslinkers, then exchange the iodide ligand by adding the corresponding substituted carbazolate salts was performed. However, there were issues that films produced by this method often show highly non-uniform distribution of emission, and the emission wavelength varied over multiple samples. This might be due to the non-complete exchange of iodide to the carbazole ligand, as well as the effect of generated biproducts. Therefore, this method was discarded and the method directly using copper-carbazolate clusters was developed.
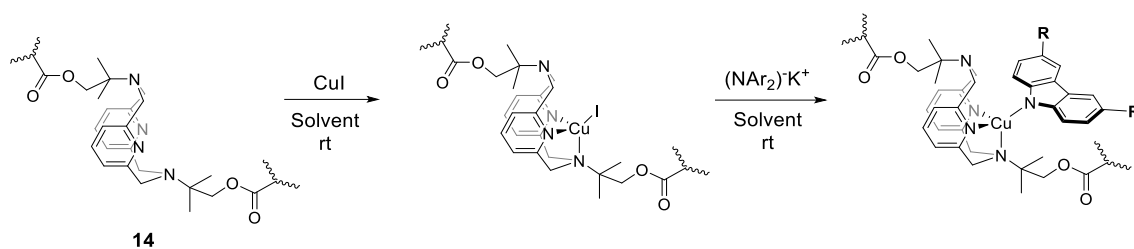
III. Cyclic voltammetry
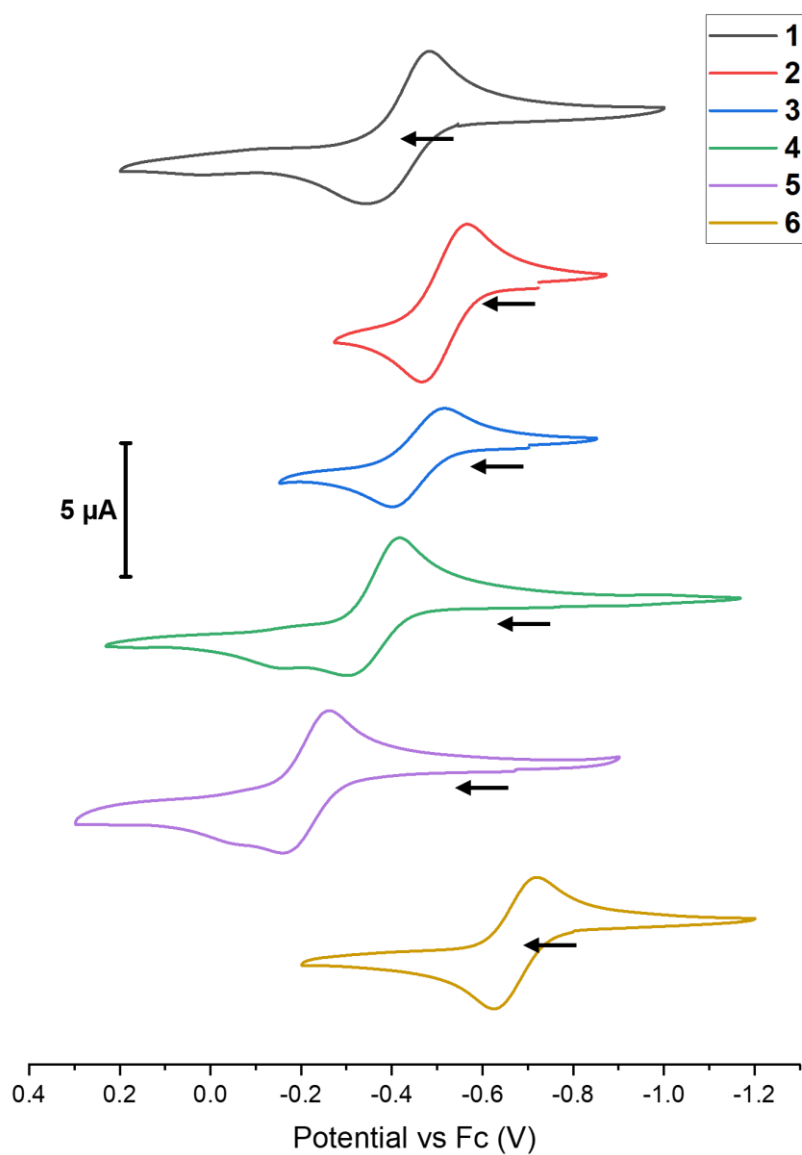
Figure S49. Cyclic voltammograms of complexes **1**-**6** (1 mM) in 0.3 M $^{n}Bu_4NBF_4$/THF at 23 °C (scan rate 100 mV s^{-1} ; 1.6 mm Pt disk working electrode; the arrow indicates the initial scan direction).

Table S1. Electrochemical properties of complexes **1-6**.[a]

Complex	E_{pf}[b] (V vs. Fc)	E_{pr}[c] (V vs. Fc)	$E_{1/2}$[d]	ΔE_p (mV)[e]
1	-0.35	-0.48	-0.41	135
2	-0.47	-0.57	-0.52	98
3	-0.40	-0.52	-0.46	115
4	-0.30[f], -0.15[g]	-0.42	-0.36[f]	112[f]
5	-0.63	-0.72	-0.67	94
6	-0.17	-0.26	-0.21	93

[a] 1 mM solution of complex in 0.3 M solution of $^nBu_4NBF_4$ as a supporting electrolyte in THF at 23 °C, Pt disk electrode (d = 1.6 mm), all potentials were referenced vs. ferrocene. [b] Forward peak potential. [c] Reverse peak potential. [e] $E_{1/2}$ was estimated as $1/2(E_{pf} + E_{pr})$.[e] The peak-to-peak separation was calculated as $|E_{pf} - E_{pr}|$. [f] For $(\kappa^4\text{-}N4)Cu^I(\text{dibenzocarbazolate})$. [g] For $(\kappa^3\text{-}N4)Cu^I(\text{dibenzocarbazolate})$.

The cyclic voltammetry of **4** showed two anodic peaks assigned to isomers with κ^4 and κ^3-coordinated N4 ligands, with κ^4-**4** showing E_{pf} shifted negatively compared to κ^3-**4**; this is consistent with the previous studies.[1, 7, 8] Variable scan rate CV measurements showed that the peak current assigned to a minor, but more easily oxidized κ^4-**4**, decreases at high scan rates when the conformational equilibrium cannot reestablish efficiently on CV timescale, and the oxidation peak corresponding to the major by less easily oxidized κ^4-**4** becomes predominant.
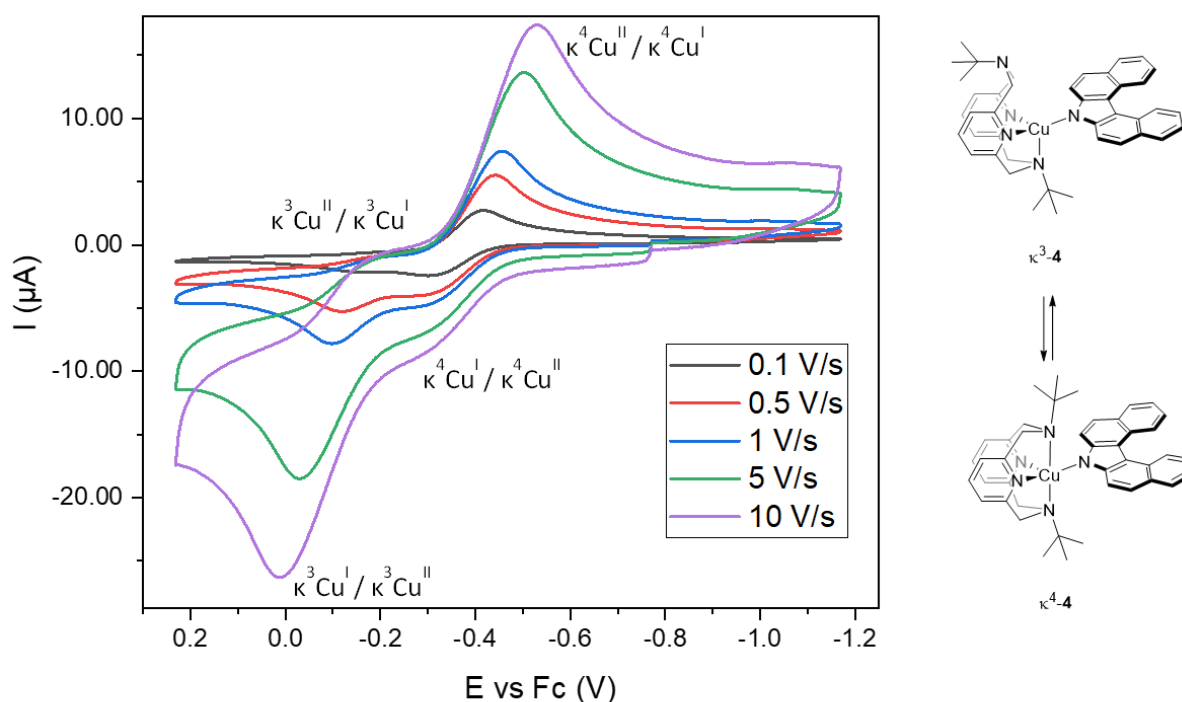
Figure S50. Cyclic voltammograms of complex **4** (1 mM) in 0.3 M $^nBu_4NBF_4$/THF at 23 °C at different scan rates.

IV. Photophysical properties of complexes and polymer films

Table S2. Photoluminescence properties of complexes **1**-**6** in crystalline state.[a]

Complex	Φ^b	λ_{max}^c (nm)	τ^d (µs)	$k_r(s^{-1})^e$	$k_{nr}(s^{-1})^f$
1	0.22	615	6.3[g]	3.5 × 10⁴	1.2 × 10⁵
2	0.44	627	2.5[g]	1.8 × 10⁵	2.3 × 10⁵
3	0.03	678	0.60[g]	6.7 × 10⁴	1.6 × 10⁶
κ³-4	0.59	598	5.9[g]	9.7 × 10⁴	6.7 × 10⁴
κ⁴-4	0.04	745	3.2[h]	1.2 × 10⁴	3.0 × 10⁵
5	<0.01	-	-	-	-
6	0.11	684	1.2[h]	9.6 × 10⁴	7.4 × 10⁵

[a]Excitation at 380 nm. [b] Photoluminescence quantum yield [c] Photoluminescence maximum. [d] Photoluminescence lifetime. [e]Radiative decay rate constant (determined as Φ/τ). [f] Non-radiative decay rate constant (Determined as $k_r(1-\Phi)/\Phi$). [g] Intensity-weighted average value based on a biexponential fit (calculated from $\alpha_1\tau_1 + \alpha_2\tau_2/(\alpha_1 + \alpha_2)$). [h] Single exponential fit.
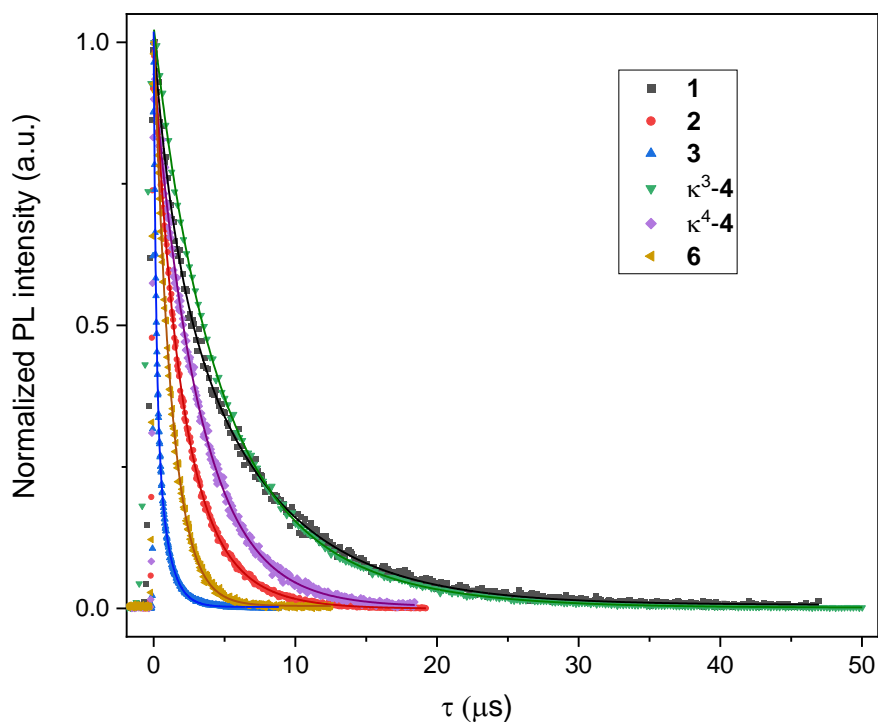
Figure S51. Normalized photoluminescence decay profile of complexes **1-4,** and **6** in crystalline state. Solid lines are fitting lines.
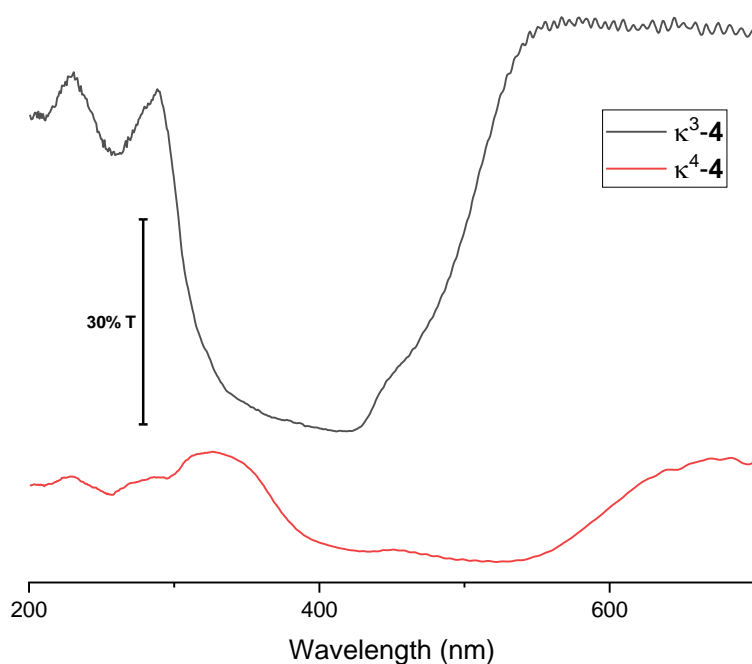
Figure S52. Transmittance of crystalline of κ^3-**4** and κ^4-**4** Curves are translated in the vertical direction for clarity, scale bar corresponding to 30% transmittance is placed on the graph.

Table S3. Photoluminescence properties of complexes **1**-**6** in 1wt% physically blended polystyrene films.[a]

Complex	Φ^b	λ_{max}^c (nm)	$\tau^{d,g}$ (μs)	k_r (s^{-1})^e	k_{nr} (s^{-1})^f
1	0.10	659	3.1^g	3.2 × 10^4	2.9 × 10^5
2	0.13	682	1.6^g	8.3 × 10^4	5.6 × 10^5
3	0.10	674	1.7^g	6.0 × 10^4	5.4 × 10^5
4	0.28	635	5.9^g	4.7 × 10^4	1.2 × 10^5
5	0.08	624	4.8^g	1.7 × 10^4	1.9 × 10^5
6	<0.01	-	-	-	-

[a] Excitation at 380 nm. [b] Photoluminescence quantum yield [c] Photoluminescence maximum. [d] Photoluminescence lifetime. [e] Radiative decay rate constant (determined as Φ/τ). [f] Non-radiative decay rate constant (Determined as $k_r(1-\Phi)/\Phi$). [g] Intensity-weighted average value based on a biexponential fit (calculated from $\alpha_1\tau_1 + \alpha_2\tau_2/(\alpha_1 + \alpha_2)$).
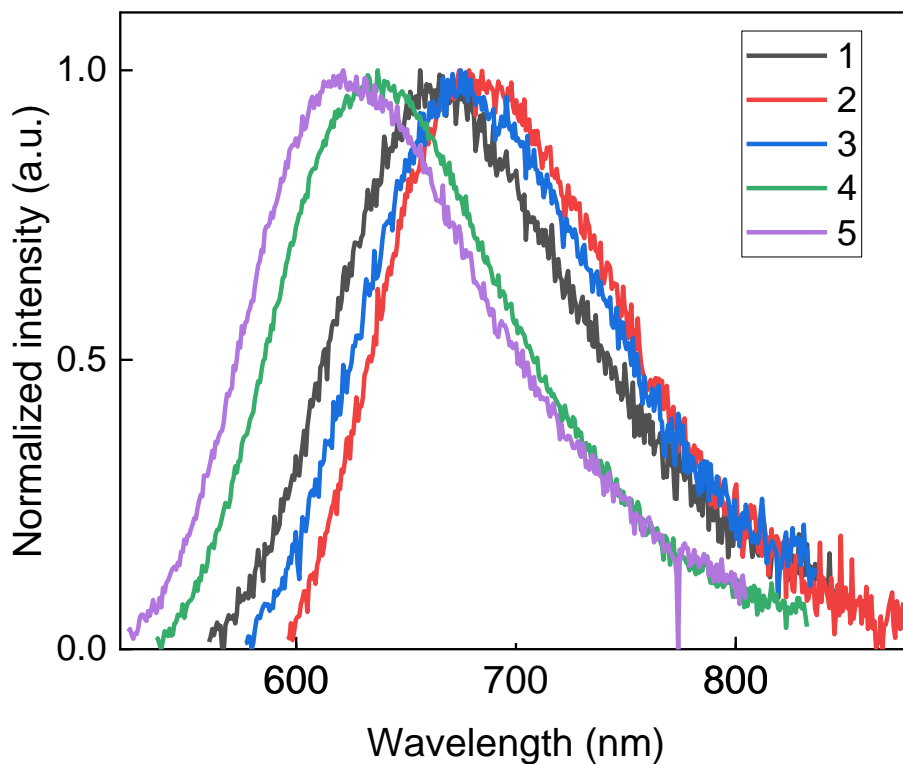
Figure S53. Normalized photoluminescence spectra of complexes **1**-**5** in 1 wt% physically blended polystyrene films.
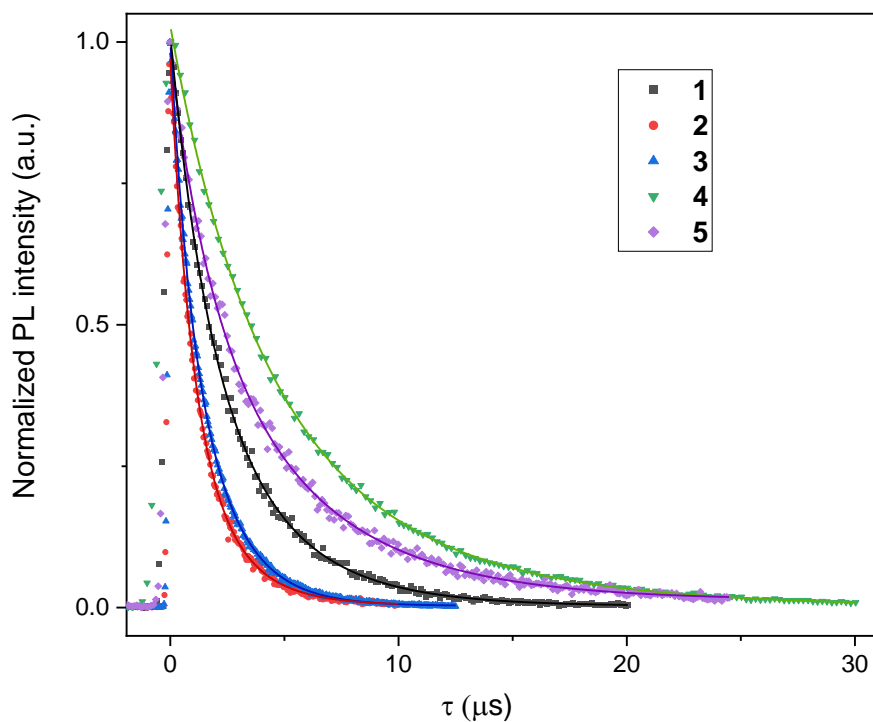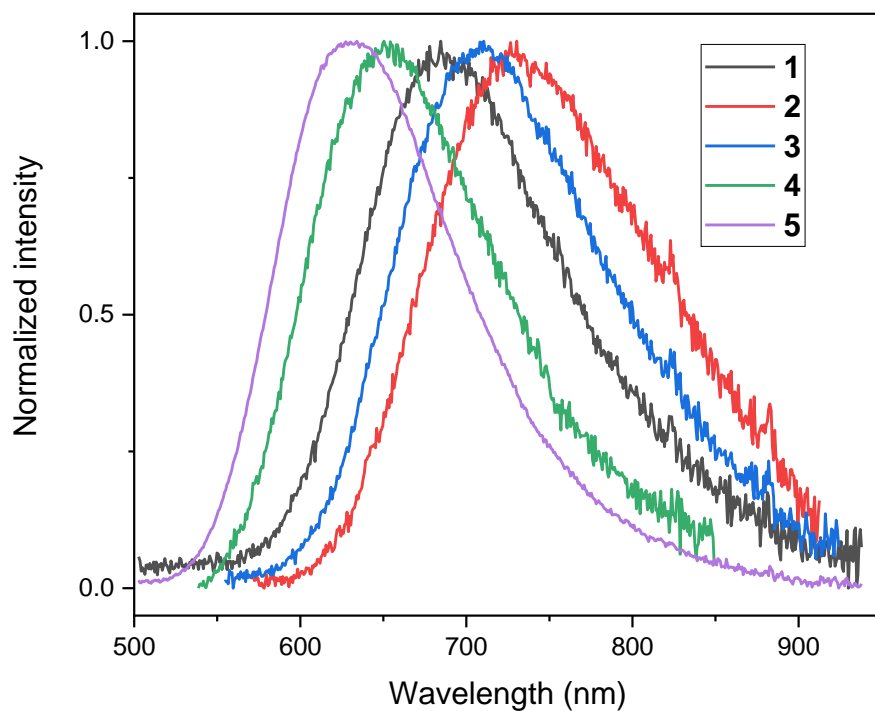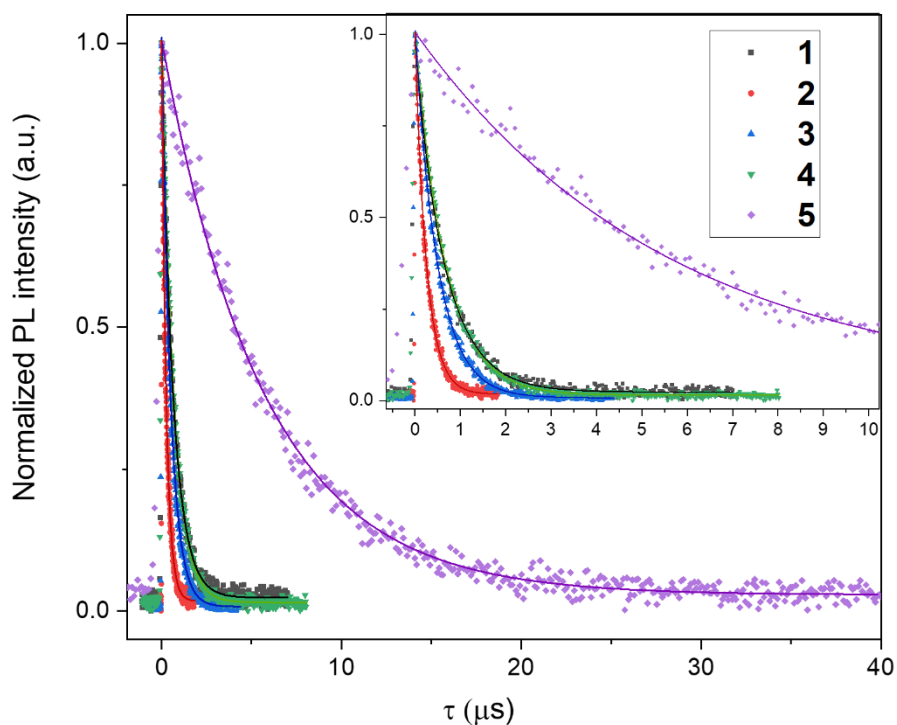

Figure S54. Normalized photoluminescence decay profile of complexes **1**-**5** in 1wt% physically blended polystyrene films. Solid lines are fitting lines.

Table S4. Photoluminescence properties of complexes **1-6** in THF solution (10^{-5} M).[a]

Complex	Φ^b	$\lambda_{max}{}^c$ (nm)	τ^d (μs)	k_r (s^{-1})^e	k_{nr} (s^{-1})^f
1	0.04	688	0.7^g	6.0×10^4	1.4×10^6
2	0.02	736	0.3^g	7.5×10^4	3.7×10^6
3	0.04	708	0.5^g	8.0×10^4	1.9×10^6
4	0.04	653	0.7^g	6.1×10^4	1.5×10^6
5	0.17	631	5.6^h	3.0×10^4	1.5×10^5
6	0.01>	-	-	-	-

[a] Excitation at 380 nm. [b] Photoluminescence quantum yield [c] Photoluminescence maximum. [d] Photoluminescence lifetime. [e] Radiative decay rate constant (determined as Φ/τ). [f] Non-radiative decay rate constant (Determined as $k_r(1-\Phi)/\Phi$). [g] Intensity-weighted average value based on a biexponential fit (calculated from $\alpha_1\tau_1 + \alpha_2\tau_2/(\alpha_1 + \alpha_2)$. [h] Single exponential fit.

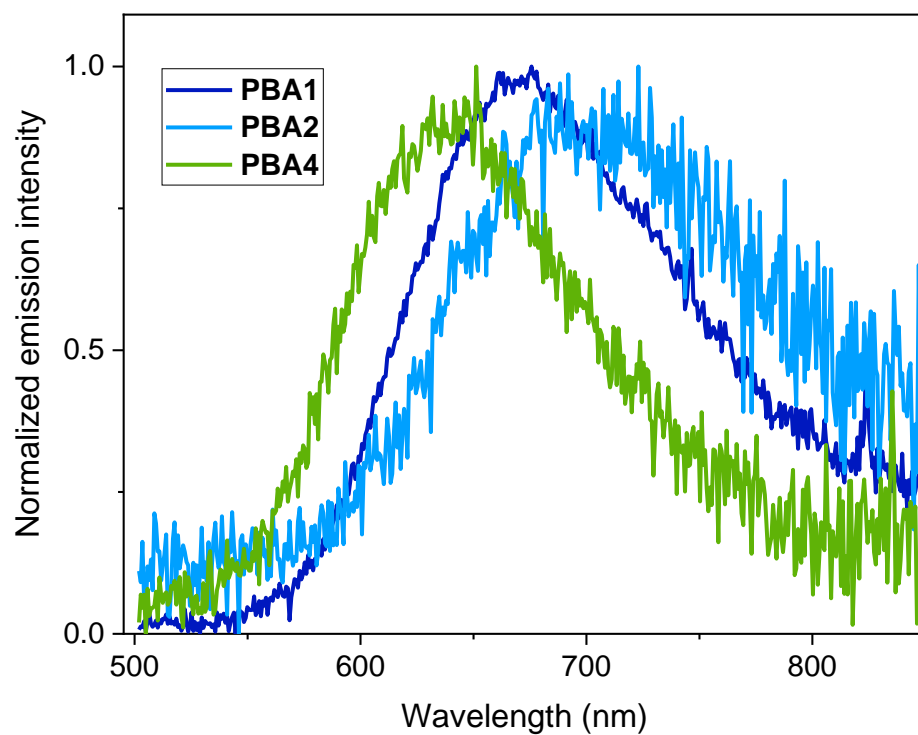**Figure S55.** Normalized photoluminescence spectra of complexes **1-5** in THF solution (10^{-5} M).

Figure S56. Normalized photoluminescence decay profile of complexes **1**-**5** in THF solution (10^{-5} M). Solid lines are fitting lines.

Table S5. Photoluminescence properties of films **PBA1, 2, 4**.[a]

| Film	Φ^b	$\lambda_{max}{}^c$ (nm)	τ^d (μs)	k_r $(s^{-1})^e$	k_{nr} $(s^{-1})^f$
PBA1	0.02	666	0.7^g	3.0×10^4	1.5×10^6
PBA2	0.01	694	0.6^g	1.6×10^4	1.6×10^6
PBA4	0.02	641	4.1^g	0.5×10^4	2.6×10^5

[a] Excitation at 380 nm. [b] Photoluminescence quantum yield (average of three different batches). [c] Photoluminescence maximum. [d] Photoluminescence lifetime. [e] Radiative decay rate constant (determined as Φ/τ). [f] Non-radiative decay rate constant (Determined as $k_r(1-\Phi)/\Phi$). [g] Intensity-weighted average value based on a biexponential fit (calculated from $\alpha_1\tau_1 + \alpha_2\tau_2/(\alpha_1 + \alpha_2)$).
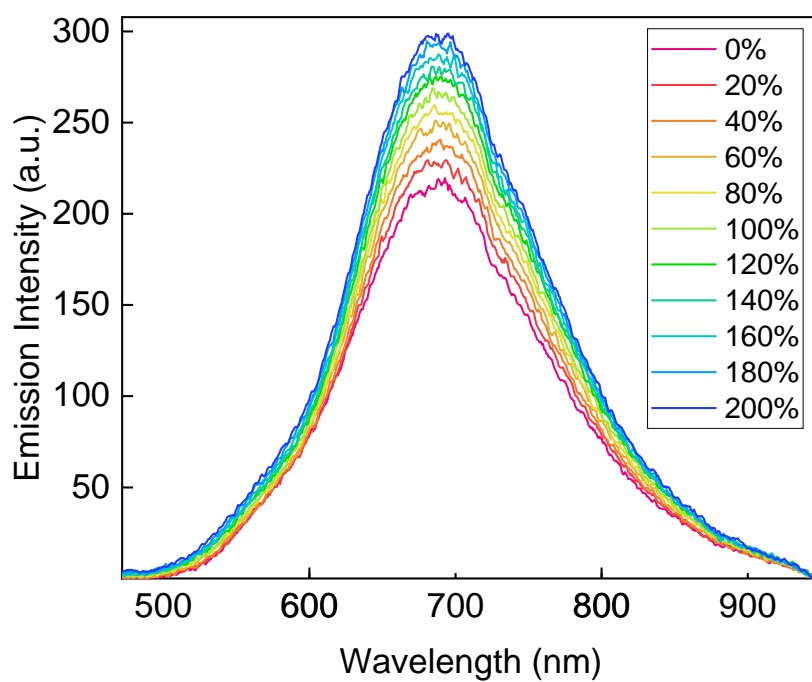
Figure S57. Normalized photoluminescence spectra of **PBA1, 2, 4**.
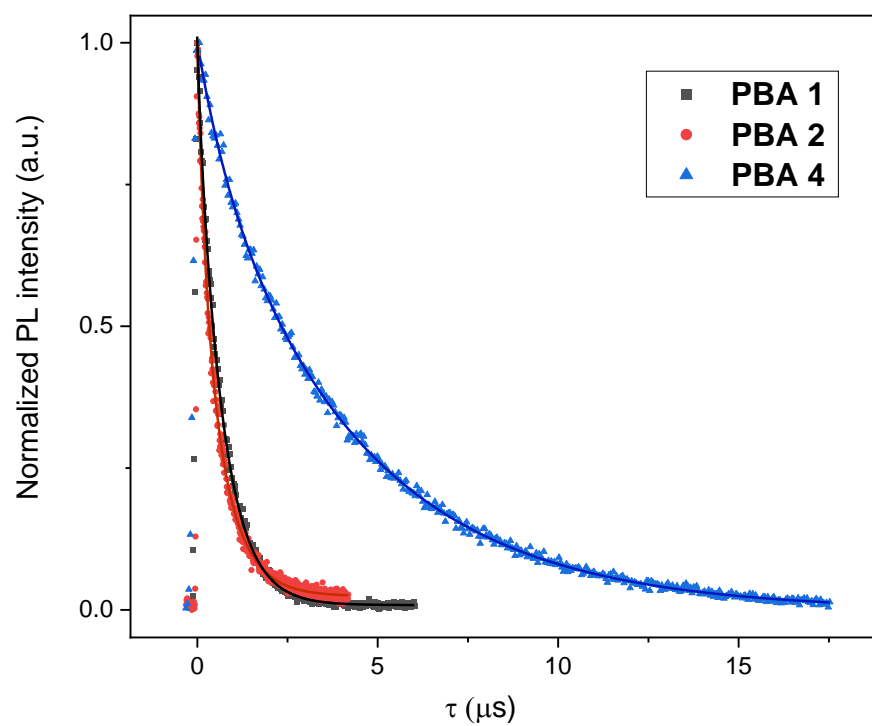
Figure S58. Normalized photoluminescence decay profile of films **PBA1**, **2**, **4**. Solid lines are fitting lines.
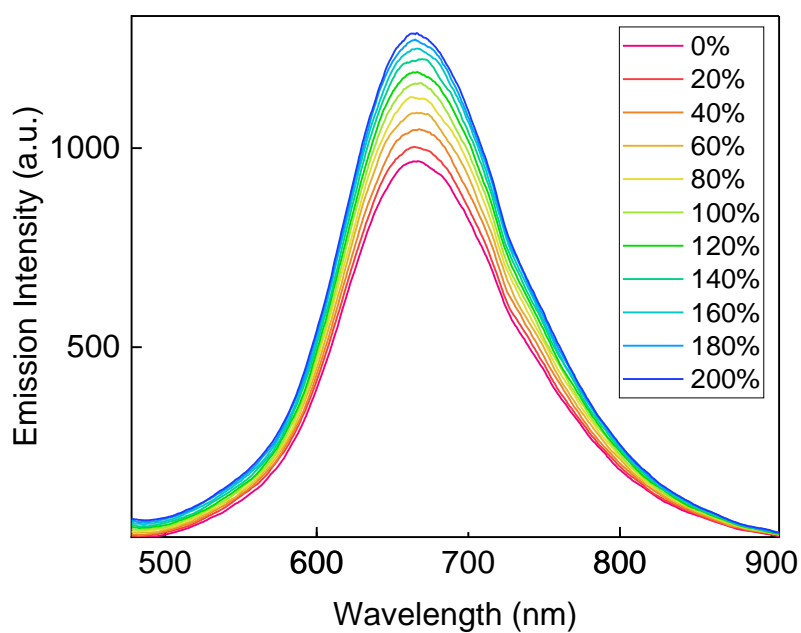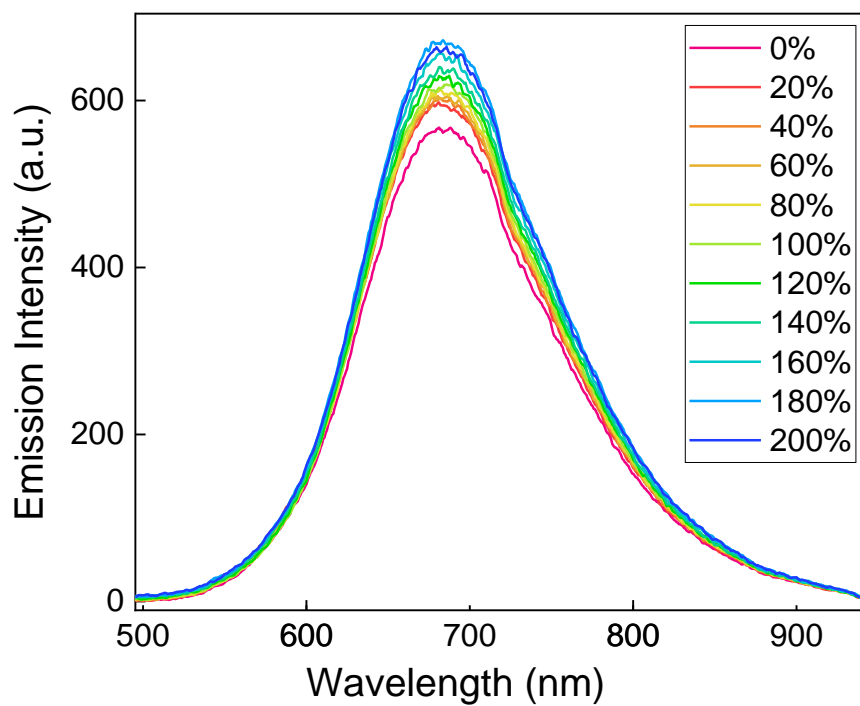
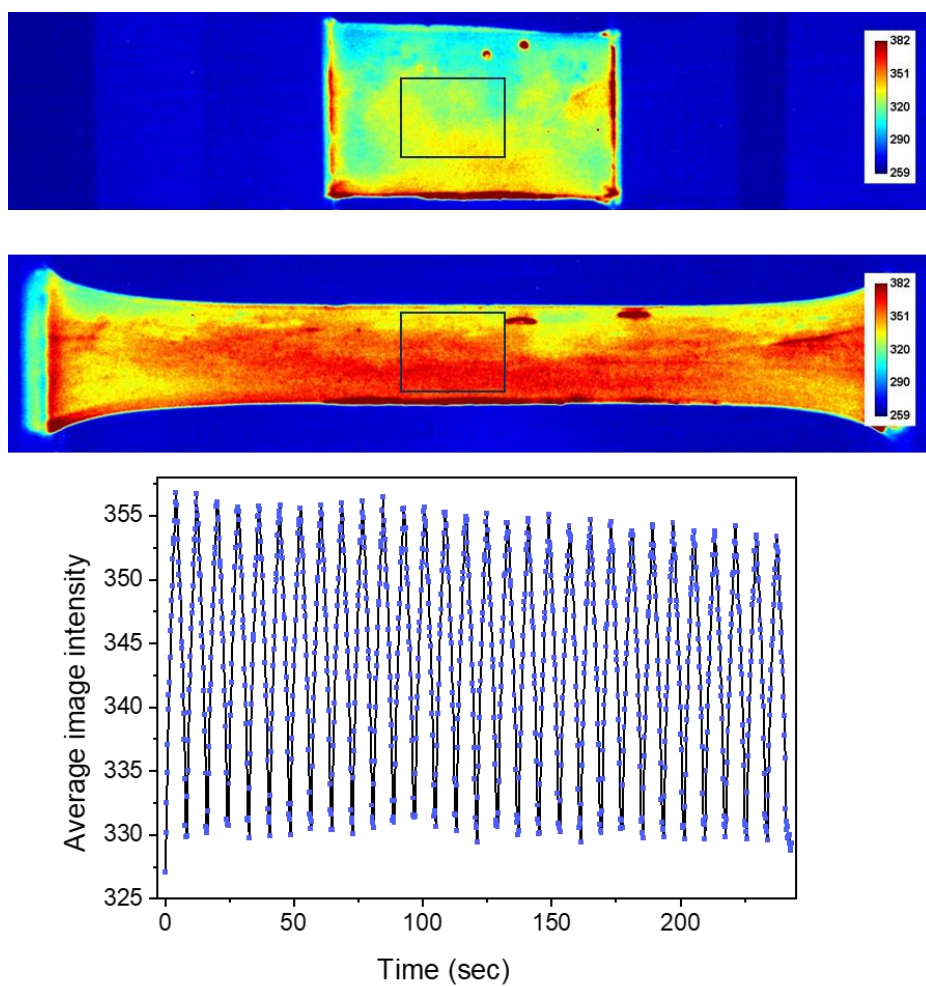**Figure S59**. Change of photoluminescence intensity of **PBA1** at variable strain. (Excitation = 395 nm)

Figure S60. Change of photoluminescence intensity of **PBA2** at variable strain. (Excitation = 395 nm)

Figure S61. Photoluminescence spectra of the control film physically incorporating complex **1** during stretching. (Excitation = 395 nm)
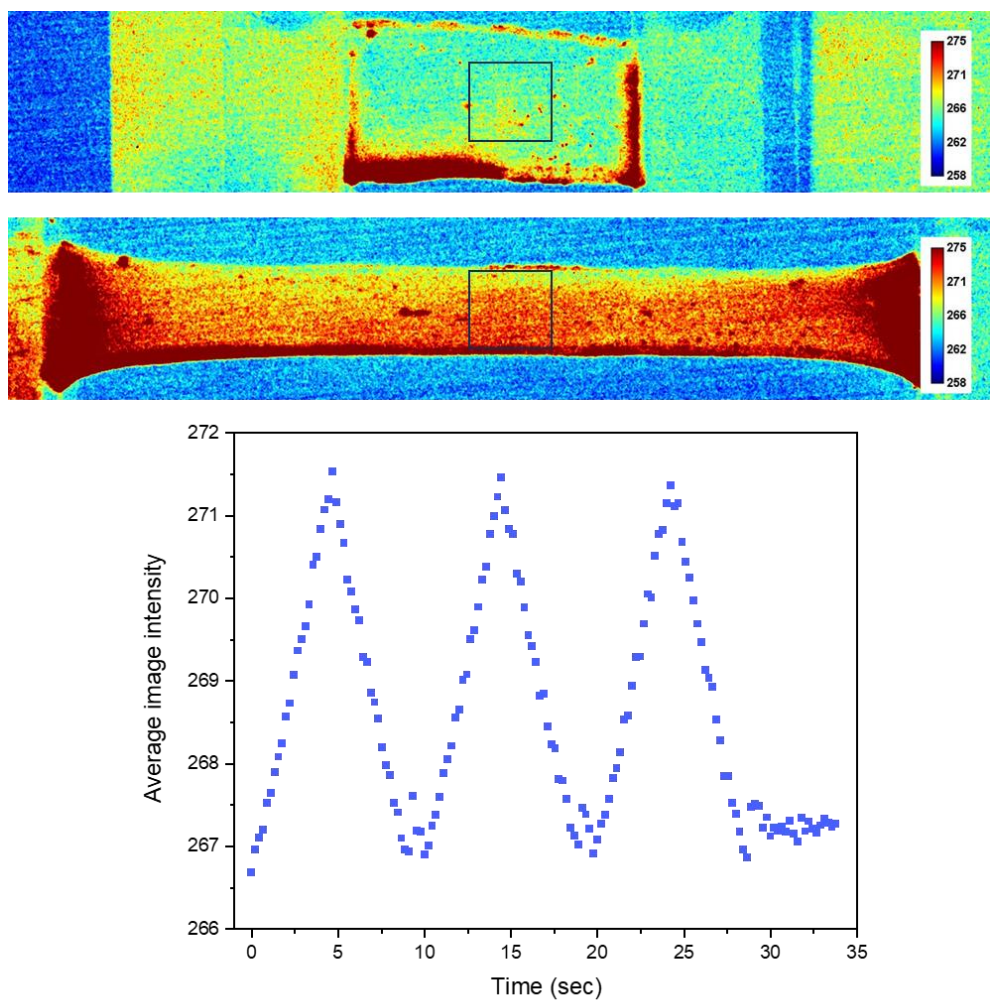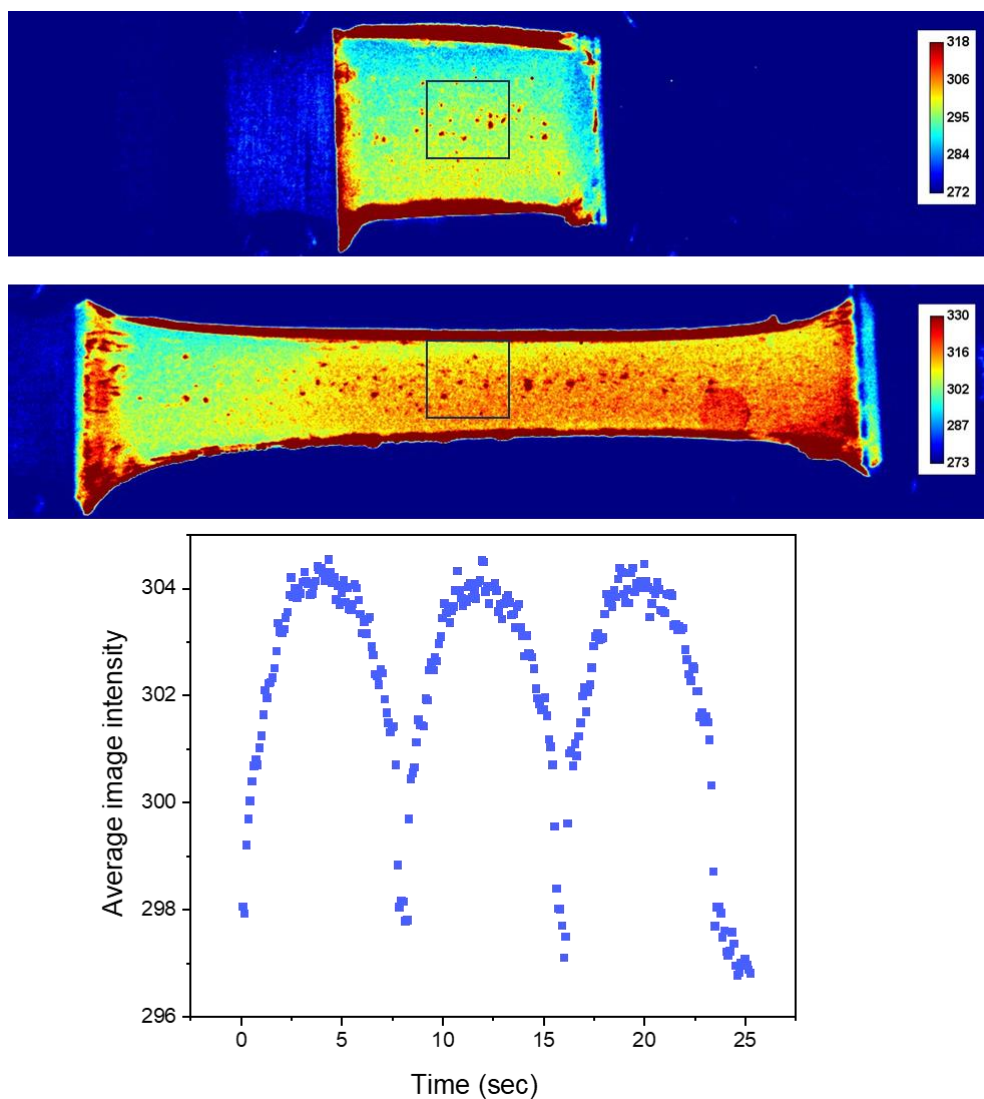
VI. Imaging analysis

Figure S62. Top: Grayscale images of **PBA1** at 0% and 200% strain. Bottom: Change of the image intensity at the selected area (black square) of **PBA1** during 30 cycles of continuous stretching and releasing (0% → 200% → 0%). (Excitation = 365 nm, speed = 10 mm per second, camera : 4.5 fps. Stretching cycle of 0% → 200% → 0% corresponds to 8 s.)
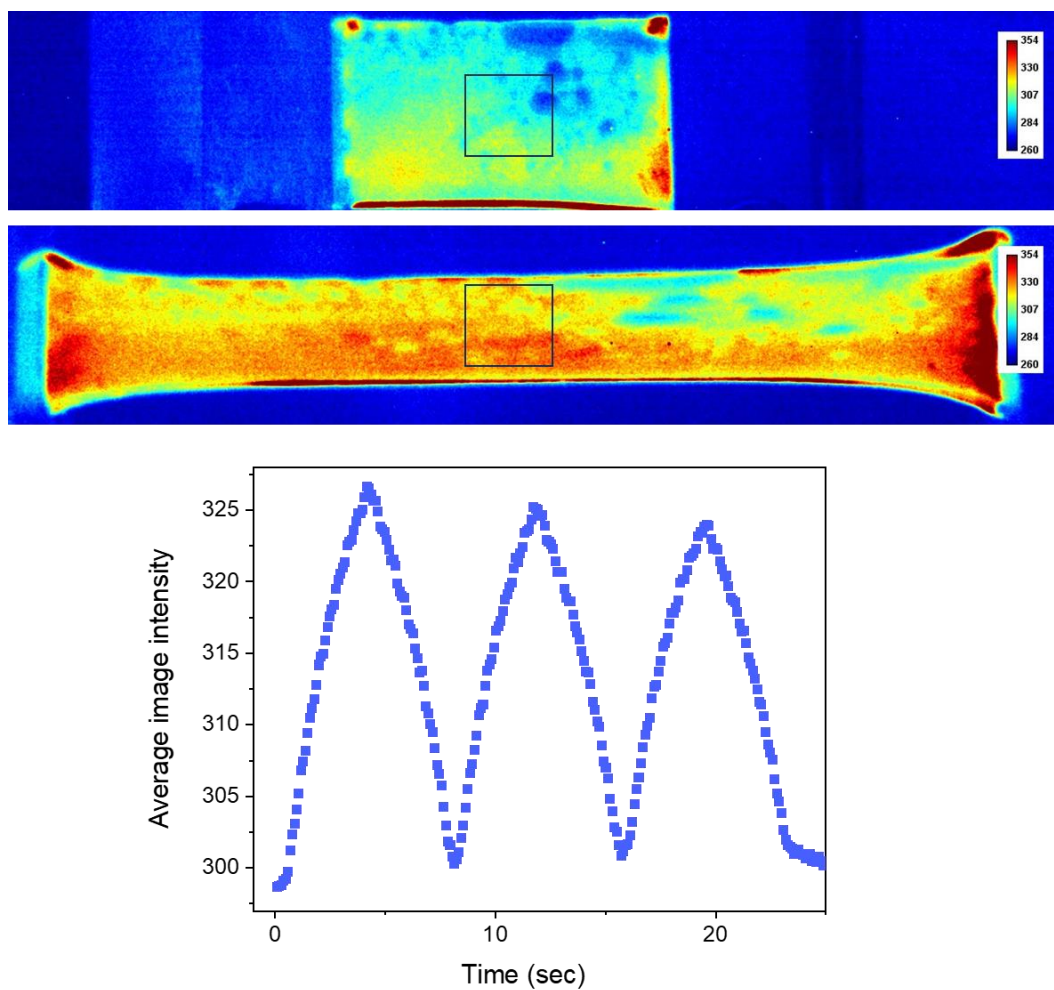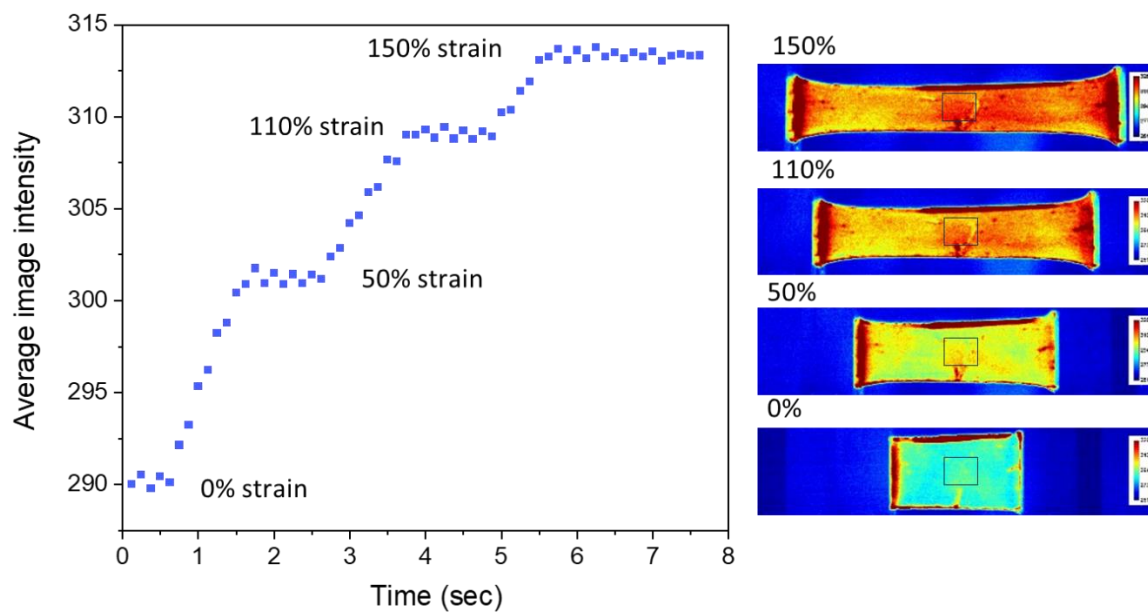
Figure S63. Top: Grayscale images of **PBA2** at 0% and 200% strain. Bottom: Change of the image intensity at the selected area (black square) of **PBA2** during 3 cycles of continuous stretching and releasing (0% → 200% → 0%). (Excitation = 365 nm, speed = 10 mm per second camera : 10 fps)

Figure S64. Top: Grayscale images of **PBA4** at 0% and 200% strain. Bottom: Change of the image intensity at the selected area (black square) of **PBA4** during 3 cycles of continuous stretching and releasing (0% → 200% → 0%). (Excitation = 365 nm, speed = 10 mm per second, camera : 4.5 fps)
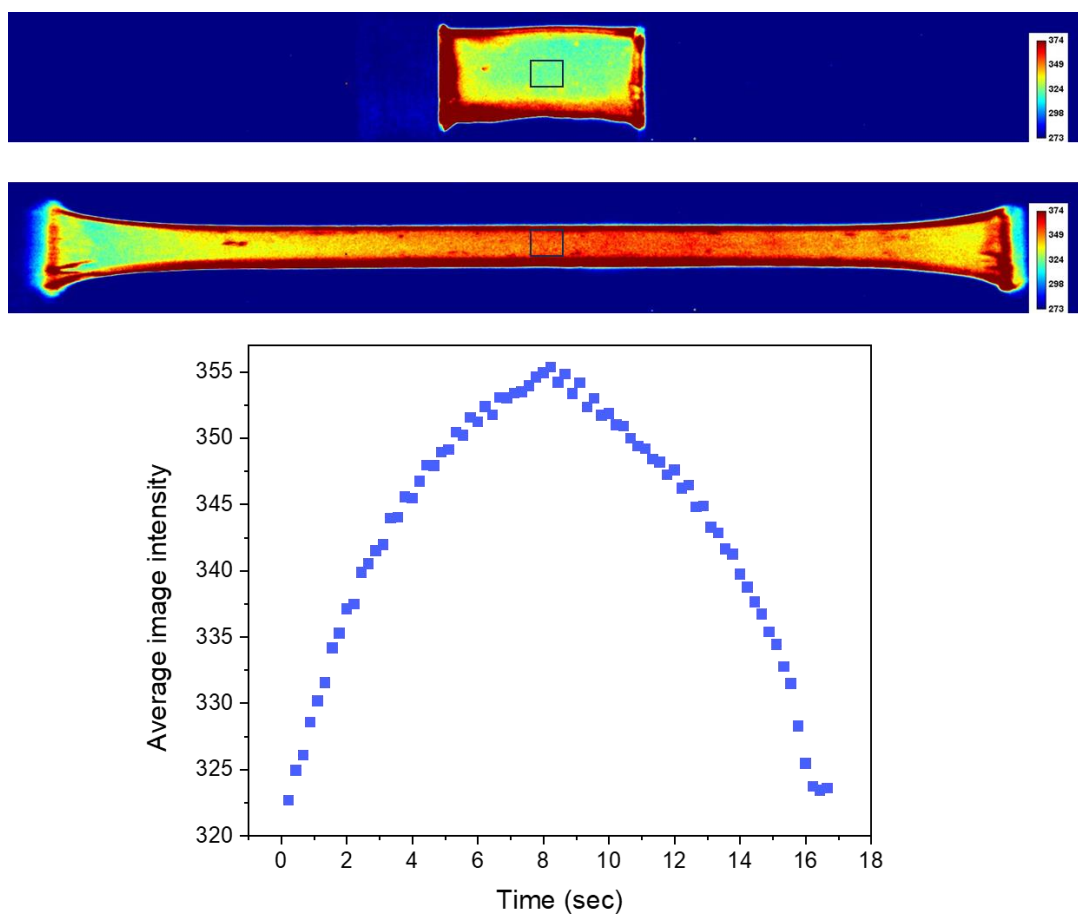
Figure S65. Top: Grayscale images of of the control film physically incorporating complex **1** at 0% and 200% strain. Bottom: Change of the image intensity at the selected area (black square) of the control film physically incorporating complex **1** during 3 cycles of continuous stretching and releasing (0% → 200% → 0%). (Excitation = 365 nm, speed = 10 mm per second, camera : 10.8 fps)

Stretching with delay

Figure S66. Left: Change of the image intensity at the selected area (black square) of film **PBA1** during stepwise stretching and pausing up to 150% strain (stretching to a fixed length for ca. 1 sec then pause for ca. 1 sec). Right: Grayscale images of **PBA1** at each pausing point. (Excitation = 365 nm, speed = 10 mm per second, camera : 8 fps)

Reversiblity at high strain

Figure S67. Top: Grayscale images of **PBA1** at 0% and 400% strain. Bottom: Change of the image intensity at the selected area (black square) of **PBA1** during 1 cycle of continuous stretching and releasing (0% → 400% → 0%). (Excitation = 365 nm, speed = 10 mm per second camera : 4.5 fps)

This experiment shows that the reversible change in the emission intensity is observed even at high strain close to the breaking limit of the film.

V. Mechanical Properties
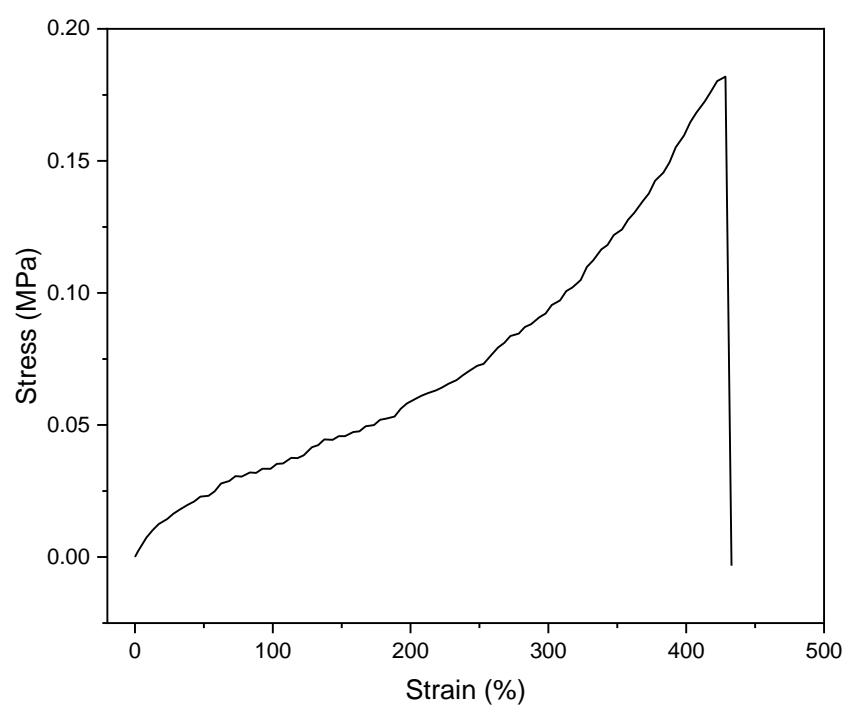
Figure S68. Representative Stress-Strain curve of film **PBA1** (stretching speed: 10mm/s).

Table S6. Mechanical properties of film **PBA1** (average of 4 samples; the standard deviations are shown in parentheses)

	Stress at break (MPa)	Strain at break (%)
PBA1	0.179 (0.024)	441 (25)

VI. Computational studies

The density functional theory (DFT) and time-dependent density functional theory (TD-DFT) calculations were performed with the program package Gaussian 16.[9] Geometry optimizations, and frequency analyses were carried out using the ωB97XD functional[10] and def2tzvp basis set[11, 12] for all elements. For orbital analysis and analysis of vertical transitions of crystalline samples, the geometries were optimized in gas phase. The frontier molecular orbitals (MOs) were analyzed by the program Chemissian version 4.67,[13] and the atomic contributions to MOs were calculated using the program GaussSum 3.0.[14]

For the comparison of relative stabilities of different isomers and the mechanisms of their interconversion, all geometries were optimized in solvent (dichloromethane) using the SMD solvation model.[15] All ground states corresponded to the absence of imaginary frequencies, and all optimized transition state structures contained one imaginary frequency.

All geometries are provided as a combined XYZ file. Animations corresponding to imaginary frequencies from vibrational analysis are provided as GIF files. Animations for transition states and IRC calculations are also supplied as supporting information files.

TD-DFT calculations and frontier orbital analysis

The contribution of atomic groups to the selected MOs and the properties of the calculated five lowest vertical transitions (oscillator strength larger than 0.005, contributions over 10%) were analyzed for complex **1,** complex κ^3-**4** and complex κ^4-**4** . The atomic groups were defined as Cu atom, NAr_2 ligand, and ^{tBu}**N4** ligand.
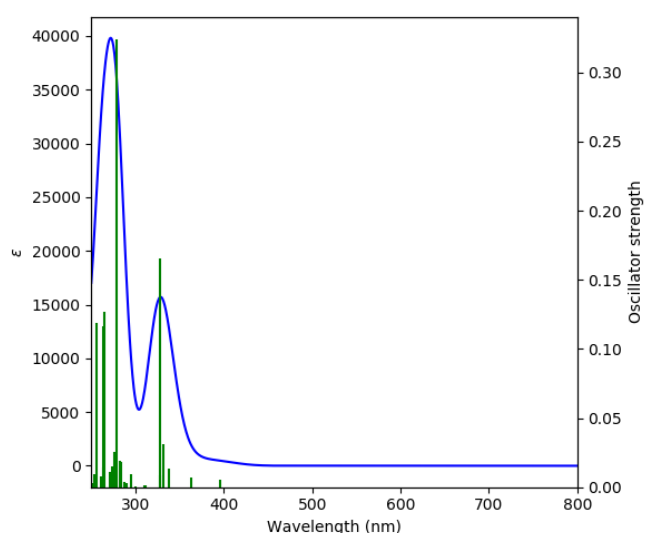
Table S7. Contribution(%) of atomic groups to the selected MOs of complex **1**.

Orbital	Cu	NAr_2	^{tBu}**N4**
LUMO+4	0	98	2
LUMO+2	0	0	100
LUMO+1	0	0	100
LUMO	2	0	97
HOMO	12	85	2
HOMO-2	74	13	13
HOMO-3	71	9	20
HOMO-4	71	10	19
HOMO-6	61	6	33

Table S8. Calculated five lowest vertical transitions of complex **1**. (oscillator strength larger than 0.005, contributions over 10%)

Wavelength (nm)	Oscillator strength	Major contributions	Character
417	0.0062	HOMO->LUMO (66%)	NAr_2-> ^{tBu}**N4**
		HOMO-3->LUMO (14%)	Cu-> ^{tBu}**N4**

		HOMO-2->LUMO (10%)	Cu->^{tBu}**N4**
375	0.0090	HOMO-2->LUMO (53%)	Cu->^{tBu}**N4**
		HOMO-3->LUMO (38%)	Cu->^{tBu}**N4**
341	0.1720	HOMO-4->LUMO (42%)	Cu->^{tBu}**N4**
		HOMO-2->LUMO (29%)	Cu->^{tBu}**N4**
		HOMO-3->LUMO (19%)	Cu->^{tBu}**N4**
321	0.3040	HOMO->LUMO+4 (90%)	NAr$_2$->NAr$_2$
280	0.0250	HOMO-2->LUMO+2 (39%)	Cu->^{tBu}**N4**
		HOMO-6->LUMO (22%)	Cu->^{tBu}**N4**
		HOMO-6->LUMO (22%)	Cu->^{tBu}**N4**

Figure S69. Calculated UV/Vis absorption spectrum of complex κ^3-**4**.

Table S9. Contribution(%) of atomic groups to the selected MOs of complex κ^3-**4**.

Orbital	Cu	NAr$_2$	^{tBu}**N4**
LUMO+3	0	98	2
LUMO+1	0	0	99
LUMO	2	0	97
HOMO	0	99	0
HOMO-1	14	83	3
HOMO-2	74	12	14
HOMO-3	63	18	18
HOMO-4	68	14	18

Table S10. Calculated five lowest vertical transitions of complex κ^3-**4** (oscillator strength larger than 0.005, contributions over 10%).

Wavelength (nm)	Oscillator strength	Major contributions	Character
395	0.0051	HOMO-1->LUMO (59%)	NAr$_2$-> ^{tBu}**N4**
		HOMO-3->LUMO (23%)	Cu-> ^{tBu}**N4**
363	0.0070	HOMO-2->LUMO (57%)	Cu-> ^{tBu}**N4**
		HOMO-3->LUMO (26%)	Cu-> ^{tBu}**N4**
337	0.136	HOMO-1->LUMO+1 (60%)	NAr$_2$-> ^{tBu}**N4**
		HOMO-3->LUMO+1 (17%)	Cu-> ^{tBu}**N4**
332	0.0315	HOMO-4->LUMO (33%)	Cu->NAr$_2$
		HOMO-1->LUMO+3 (24%)	NAr$_2$-> NAr$_2$
		HOMO-2->LUMO (18%)	Cu-> ^{tBu}**N4**
328	0.0085	HOMO-1->LUMO+3 (44%)	NAr$_2$-> NAr$_2$
		HOMO-4->LUMO (24%)	Cu-> ^{tBu}**N4**
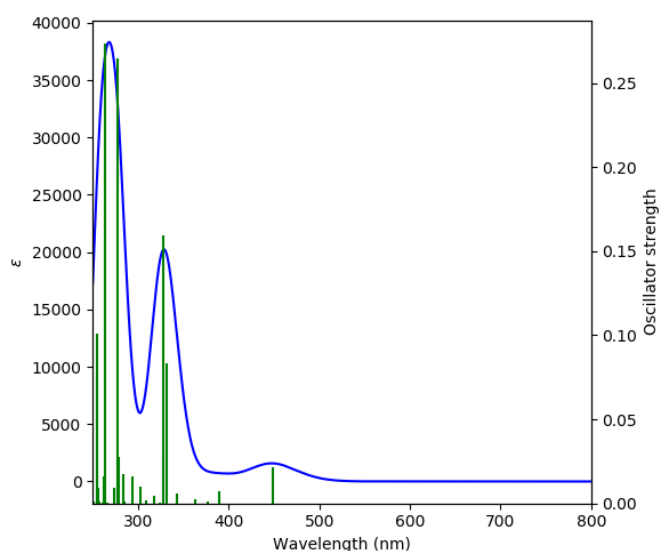
Figure S70. Calculated UV/Vis absorption spectrum of complex κ^4-**4**.

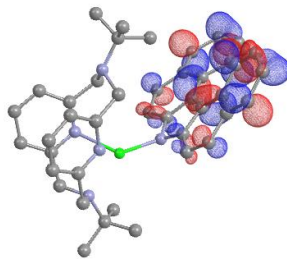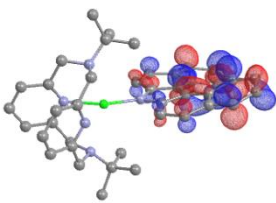**Table S11**. Contribution(%) of atomic groups to the selected MOs of complex κ^4-**4**.

Orbital	Cu	NAr$_2$	^{tBu}**N4**
LUMO+5	1	99	1
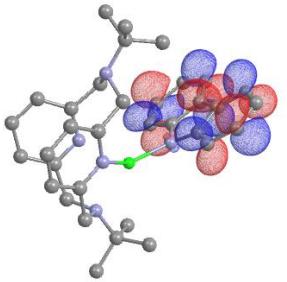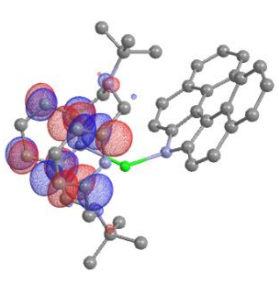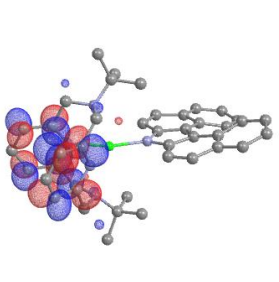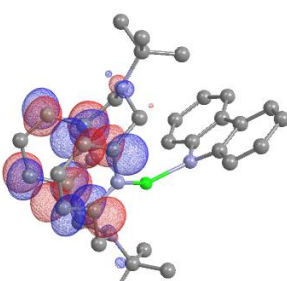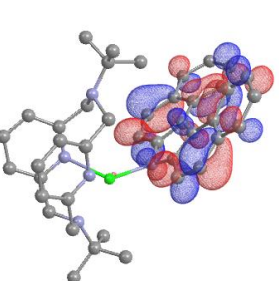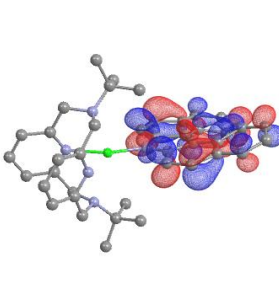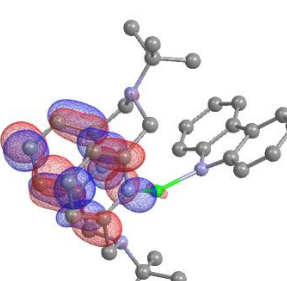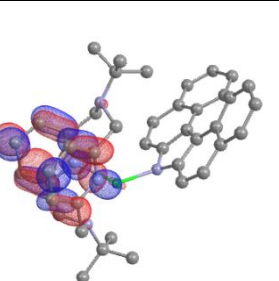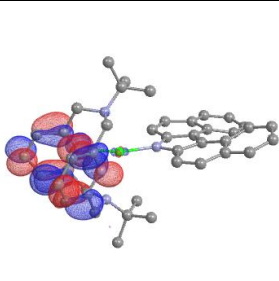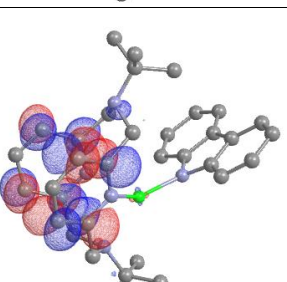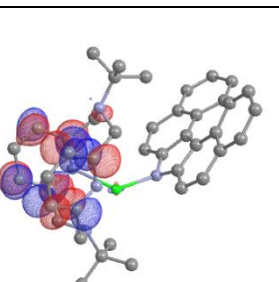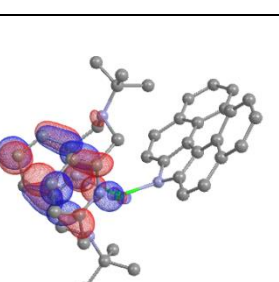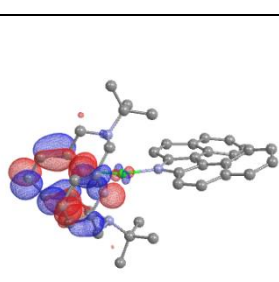
LUMO+3	0	98	1
LUMO+2	0	1	99
LUMO	3	0	96
HOMO	0	100	0
HOMO-1	8	90	1
HOMO-2	68	8	24
HOMO-3	76	3	21
HOMO-5	85	6	9
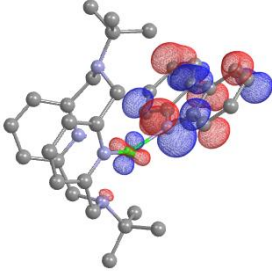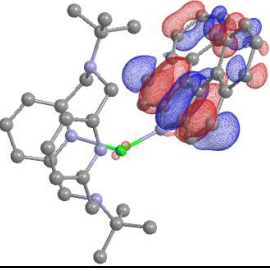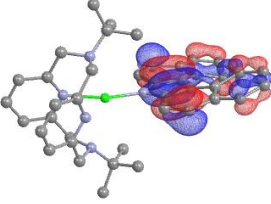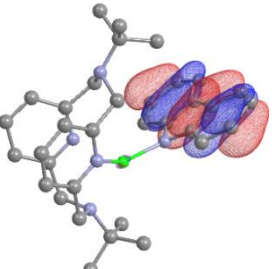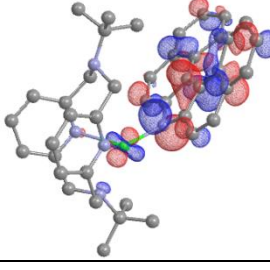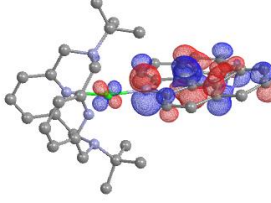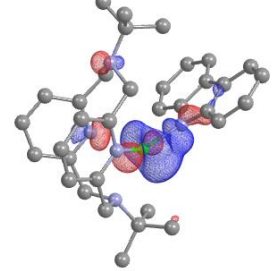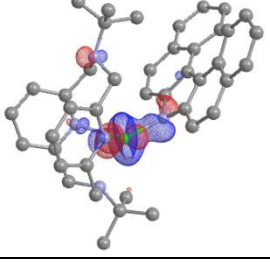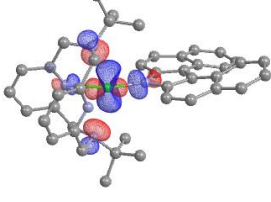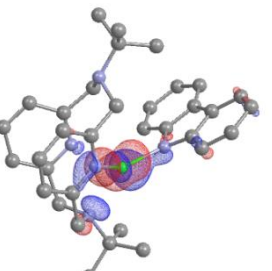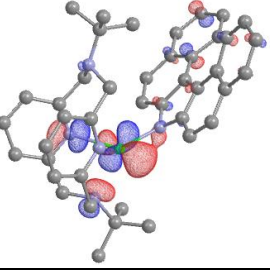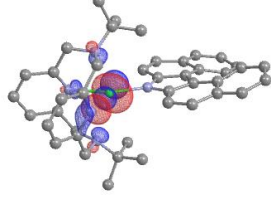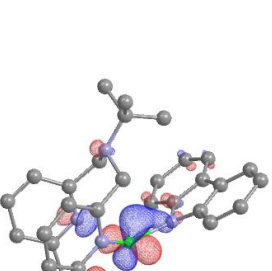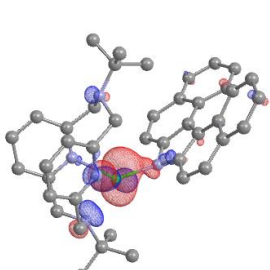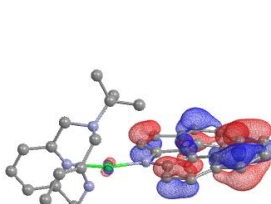
Table S12. Calculated five lowest vertical transitions of complex κ^4-**4**.(oscillator strength larger than 0.005, contributions over 10%).

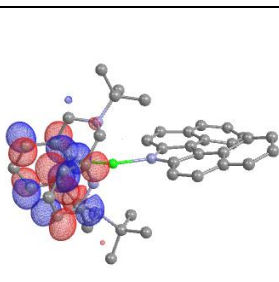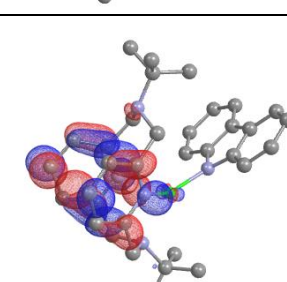| Wavelength (nm)	Oscillator strength	Major contributions	Character
448	0.0216	HOMO-2->LUMO (91%)	Cu-> ^{tBu}**N4**
390	0.0071	HOMO-3->LUMO (73%)	Cu-> ^{tBu}**N4**
		HOMO-1->LUMO (16%)	NAr$_2$-> ^{tBu}**N4**
332	0.0834	HOMO-1->LUMO+3 (60%)	NAr$_2$-> NAr$_2$
		HOMO-5->LUMO (15%)	Cu-> ^{tBu}**N4**
328	0.0296	HOMO-5->LUMO (39%)	Cu-> ^{tBu}**N4**
		HOMO-2->LUMO+2 (15%)	Cu-> ^{tBu}**N4**
		HOMO->LUMO+3 (14%)	NAr$_2$-> NAr$_2$
		HOMO-1->LUMO+3 (13%)	NAr$_2$-> NAr$_2$
327	0.1592	HOMO->LUMO+3 (64%)	NAr$_2$-> NAr$_2$
		HOMO-1->LUMO+5 (24%)	NAr$_2$-> NAr$_2$

Table S13. Calculated frontier orbitals of complexes 1, κ^3-4, and κ^4-4 (isovalue = 0.04).

	1	**4(κ^3)**	**4(κ^4)**
LUMO+5			

LUMO+4			
LUMO+3			
LUMO+2			
LUMO+1			
LUMO			

HOMO			
HOMO-1			
HOMO-2			
HOMO-3			
HOMO-4			

HOMO-5			
HOMO-6			
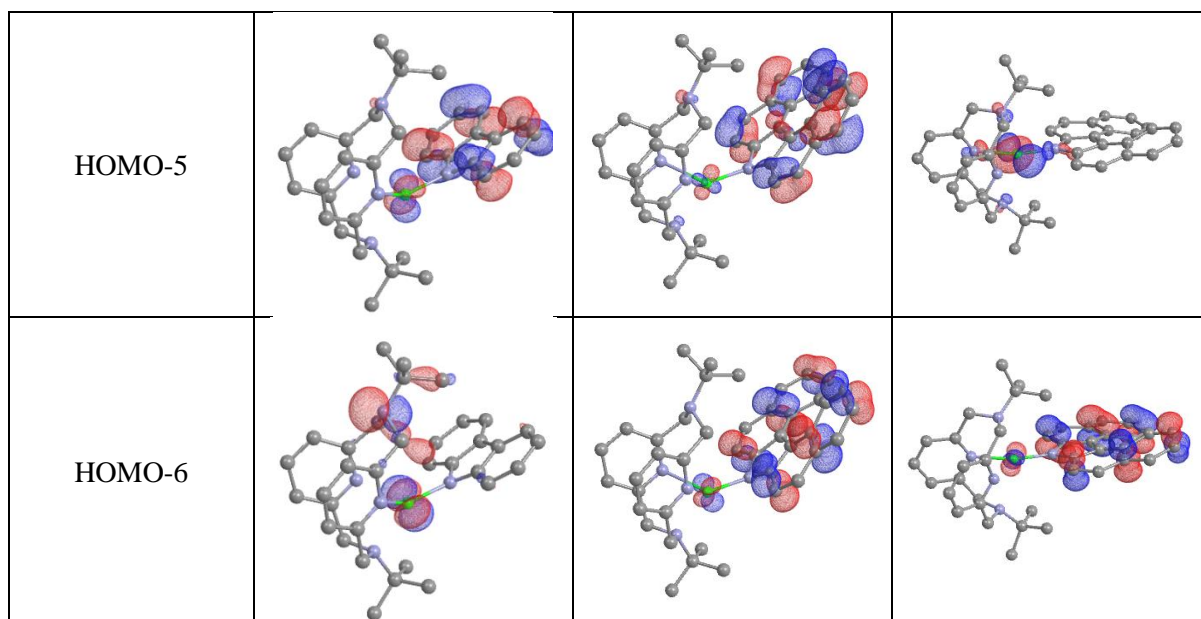
Computational analysis of isomerization behavior and conformational lability

The geometries of isomers of **1** with κ^3, κ^4 and κ^2-coordinated N4 ligands were optimized using the ωB97XD functional and def2tzvp basis set in solvent (dichloromethane) using the SMD solvation model. The mechanism of their isomerization was analyzed and transition states were identified for the $\kappa^3 \leftrightarrows \kappa^4$ isomerization (**TS4-3**) and the $\kappa^3 \leftrightarrows \kappa^2$ isomerization (**TS3-2**) of complex **1**. The nature of transition states was confirmed by IRC calculations. The results are summarized below.

For complex **4**, relative stabilities of two isomers were compared, κ^3-**4** and κ^4-**4**, using the same method.
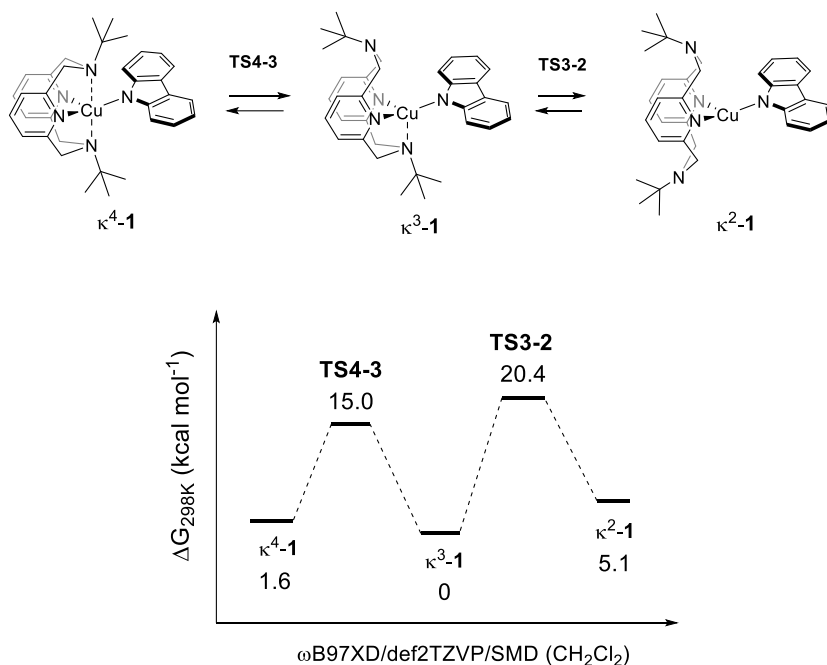
Scheme S5. Energy profile of the isomerization of complex **1**. Energies ΔG in kcal mol^{-1} are relative to the κ^3-**1** isomer.

Table S13. Gibbs free energies of the geometry-optimized structures for complex **1**.

	ΔG (Hartree)	Relative ΔG (kcal mol^{-1})
κ^3-**1**	-3233.62328	0.0
κ^4-**1**	-3233.62075	1.6
κ^2-**1**	-3233.61515	5.1
TS4-3	-3233.59932	15.0
TS3-2	-3233.59083	20.4

Table S14. Gibbs free energies of the geometry-optimized structures for complex **4**.

	ΔG (Hartree)	Relative ΔG (kcal mol^{-1})
κ^3-**4**	-3540.82	0.0
κ^4-**4**	-3540.82	0.7

VII. X-ray structure determination details

For compounds **1-3**, **5-6** and **8-9**

The X-ray diffraction data for the single crystals were collected on a Rigaku XtaLab PRO instrument (κ-goniometer) with a PILATUS3 R 200K hybrid pixel array detector using Cu $K\alpha$ (1.54184 Å) or $K\alpha$ (0.71073 Å) radiation monochromated by means of multilayer optics. The performance mode of MicroMax™-003 microfocus sealed X-ray tubes was 50 kV, 0.60 mA. The diffractometer was equipped with a Rigaku GN2 system for low temperature experiments. Images were indexed and integrated and data were corrected using the *CrysAlisPro* data reduction package (Rigaku Oxford Diffraction).

The structures were solved by *intrinsic* phasing approach using *SHELXT*-2018/2[16] and refined by the full-matrix least-squares on F^2 using *SHELXL*-2018/3.[17] Calculations were mainly performed using *WinGX*-2021.3.[18] Non-hydrogen atoms were refined anisotropically. The positions of hydrogen atoms of methyl groups were found using rotating group refinement with idealized tetrahedral angles. The other hydrogen atoms were inserted at the calculated positions and refined as riding atoms. The disorder, if present, was resolved using free variables and reasonable restraints on geometry and anisotropic displacement parameters.

For compound **κ³-4** (containing diethyl ether solvent)

Single orange plate-shaped crystals of **BJK1451_auto** were used as supplied. A suitable crystal with dimensions $0.15 \times 0.10 \times 0.04$ mm³ was selected and mounted on a XtaLAB AFC12 (RINC): Kappa dual home/near diffractometer. The crystal was kept at a steady $T = 93.15$ K during data collection. The structure was solved with the **ShelXT**[16] solution program using dual methods and by using **Olex2** 1.5[19] as the graphical interface. The model was refined with **ShelXL** 2014/7[17] using full matrix least squares minimization on F^2.

For compound **κ³-4-2** (not containing diethyl ether solvent)

Single yellow needle-shaped crystals of **RJK1465_auto** were used as supplied. A suitable crystal with dimensions $0.29 \times 0.06 \times 0.04$ mm³ was selected and mounted on a XtaLAB AFC12 (RINC): Kappa dual home/near diffractometer. The crystal was kept at a steady $T = 100$ K during data collection. The structure was solved with the **ShelXT**[16] solution program using dual methods and by using **Olex2** 1.5[19]

as the graphical interface. The model was refined with **ShelXL** 2016/6[17] using full matrix least squares minimization on F^2.

<u>For compound κ^4-4</u>

Experimental. Single red plate-shaped crystals of **RJK1461_auto** were used as supplied. A suitable crystal with dimensions $0.24 \times 0.12 \times 0.09$ mm^3 was selected and mounted on a XtaLAB AFC12 (RINC): Kappa dual home/near diffractometer. The crystal was kept at a steady $T = 100$ K during data collection. The structure was solved with the **ShelXT**[16] solution program using dual methods and by using **Olex2** 1.5[19] as the graphical interface. The model was refined with **ShelXL** 2016/6[17] using full matrix least squares minimization on F^2.

<u>For compound **10**</u>

Single orange block-shaped crystals of **rjk1526_auto_pl** were used as supplied. A suitable crystal with dimensions $0.10 \times 0.06 \times 0.06$ mm^3 was selected and mounted on a XtaLAB AFC12 (RINC): Kappa dual home/near diffractometer. The crystal was kept at a steady $T = 100$ K during data collection. The structure was solved with the **ShelXT**[16] solution program using dual methods and by using **Olex2** 1.5[19] as the graphical interface. The model was refined with **ShelXL** 2019/3[17] using full matrix least squares minimization on F^2.

Crystallographic data for 1.

C$_{35}$H$_{41.5}$CuN$_{5.5}$, orange plank ($0.137 \times 0.101 \times 0.039$ mm^3), formula weight 602.77 g mol^{-1}; orthorhombic, *Pbcn* (No. 60), $a = 14.32746(7)$ Å, $b = 12.45283(5)$ Å, $c = 34.81445(13)$ Å, $V = 6211.50(5)$ Å^3, $Z = 8$, $Z' = 1$, $T = 100(2)$ K, $d_{calc} = 1.289$ g cm^{-3}, μ(Cu $K\alpha$) = 1.236 mm^{-1}, $F(000) = 2552$; T$_{max}$/T$_{min}$ = 1.000/0.558; 118176 reflections were collected ($3.996° \leq \theta \leq 80.026°$, index ranges: $-18 \leq h \leq 18$, $-15 \leq k \leq 15$, and $-44 \leq l \leq 44$), 6760 of which were unique, $R_{int} = 0.0346$, $R_\sigma = 0.0144$; completeness to θ of 80.026° 99.6 %. The refinement of 383 parameters with no restraints converged to $R1 = 0.0311$ and $wR2 = 0.0836$ for 6518 reflections with $I > 2\sigma(I)$ and $R1 = 0.0319$ and $wR2 = 0.0843$ for all data with goodness-of-fit $S = 1.039$ and residual electron density $\rho_{max}/\rho_{min} = 0.298/-0.445$ e Å^{-3}, rms 0.046 e Å^{-3}; max shift/e.s.d. in the last cycle 0.001.

Crystallographic data for 2.

$C_{36}H_{44}CuN_5O_2$, orange plank ($0.070 \times 0.060 \times 0.044$ mm^3), formula weight 642.30 g mol^{-1}; triclinic, $P\bar{1}$ (No. 2), $a = 12.71940(11)$ Å, $b = 13.23166(17)$ Å, $c = 20.6802(2)$ Å, $\alpha = 106.7219(10)°$, $\beta = 106.8077(8)°$, $\gamma = 90.6783(9)°$, $V = 3173.69(6)$ Å^3, $Z = 4$, $Z' = 2$, $T = 100(2)$ K, $d_{calc} = 1.344$ g cm^{-3}, $\mu(Cu\ K\alpha) = 1.287$ mm^{-1}, $F(000) = 1360$; $T_{max}/T_{min} = 1.000/0.876$; 68602 reflections were collected ($3.507° \leq \theta \leq 80.687°$, index ranges: $-16 \leq h \leq 16$, $-16 \leq k \leq 11$, and $-26 \leq l \leq 26$), 13173 of which were unique, $R_{int} = 0.0500$, $R_\sigma = 0.0330$; completeness to θ of 80.687° 94.4 %. The refinement of 820 parameters with 43 restraints converged to $R1 = 0.0376$ and $wR2 = 0.1023$ for 12255 reflections with $I > 2\sigma(I)$ and $R1 = 0.0397$ and $wR2 = 0.1041$ for all data with goodness-of-fit $S = 1.101$ and residual electron density $\rho_{max}/\rho_{min} = 0.670/-0.594$ e Å^{-3}, rms 0.060 e Å^{-3}; max shift/e.s.d. in the last cycle 0.002.

Crystallographic data for 3.

$C_{50}H_{72}CuN_5O_2$, orange prism ($0.319 \times 0.163 \times 0.129$ mm^3), formula weight 838.66 g mol^{-1}; orthorhombic, $Pnma$ (No. 62), $a = 17.1539(4)$ Å, $b = 20.3189(5)$ Å, $c = 13.4474(3)$ Å, $V = 4687.1(2)$ Å^3, $Z = 4$, $Z' = 0.5$, $T = 100(2)$ K, $d_{calc} = 1.188$ g cm^{-3}, $\mu(Mo\ K\alpha) = 0.509$ mm^{-1}, $F(000) = 1808$; $T_{max}/T_{min} = 1.000/0.485$; 66690 reflections were collected ($2.578° \leq \theta \leq 32.059°$, index ranges: $-25 \leq h \leq 24$, $-30 \leq k \leq 26$, and $-20 \leq l \leq 20$), 8366 of which were unique, $R_{int} = 0.0355$, $R_\sigma = 0.0247$; completeness to θ of 32.059° 99.8 %. The refinement of 379 parameters with 462 restraints converged to $R1 = 0.0660$ and $wR2 = 0.1807$ for 7005 reflections with $I > 2\sigma(I)$ and $R1 = 0.0771$ and $wR2 = 0.1880$ for all data with goodness-of-fit $S = 1.072$ and residual electron density $\rho_{max}/\rho_{min} = 2.186/-0.670$ e Å^{-3}, rms 0.093 e Å^{-3}; max shift/e.s.d. in the last cycle 0.001.

Crystallographic data for $\underline{\kappa^3\text{-}4}$ (with diethyl ether).

$C_{46}H_{54}CuN_5O$, $M_r = 756.48$, monoclinic, $P2_1/c$ (No. 14), $a = 13.72164(7)$ Å, $b = 14.80305(6)$ Å, $c = 18.99296(9)$ Å, $\beta = 95.9445(4)°$, $\alpha = \gamma = 90°$, $V = 3837.15(3)$ Å^3, $T = 93.15$ K, $Z = 4$, $Z' = 1$, μ (Cu K$_a$) = 1.127, 36043 reflections measured, 8266 unique (R$_{int} = 0.0192$) which were used in all calculations. The final wR_2 was 0.0789 (all data) and R_1 was 0.0299 (I≥2 σ(I)).

Crystallographic data for $\underline{\kappa^3\text{-}4\text{-}2}$ (without diethyl ether).

$C_{42}H_{44}CuN_5$, $M_r = 682.36$, monoclinic, $P2_1/n$ (No. 14), $a = 15.29636(14)$ Å, $b = 13.67332(10)$ Å, $c = 17.78811(18)$ Å, $\beta = 114.7214(12)°$, $\alpha = \gamma = 90°$, $V = 3379.45(6)$ Å^3, $T = 100$ K, $Z = 4$, $Z' = 1$, μ(Cu

K_a) = 1.200, 21482 reflections measured, 7010 unique (R_{int} = 0.0280) which were used in all calculations. The final wR_2 was 0.0880 (all data) and R_1 was 0.0321 (I≥2 σ(I)).

Crystallographic data for <u>κ⁴-4.</u>

$C_{42}H_{44}CuN_5$, M_r = 682.36, orthorhombic, *Pbca* (No. 61), a = 18.82101(12) Å, b = 16.82525(12) Å, c = 21.49677(17) Å, α = β = γ = 90°, V = 6807.34(8) Å³, T = 100 K, Z = 8, Z' = 1, μ(Cu K_a) = 1.192, 29274 reflections measured, 7262 unique (R_{int} = 0.0299) which were used in all calculations. The final wR_2 was 0.1112 (all data) and R_1 was 0.0379 (I≥2 σ(I)).

The maximum and minimum residual electron density values of +0.31/-0.52 e Å⁻³ are within acceptable limits. Indeed, the negative residual density is observed around the copper atom. The Hirshfeld atom refinement, which accounts for interatomic charge transfer and valence shell deformation, has allowed us to increase the negative residual density up to –0.3 e Å⁻³, but the skewness to negative density at the copper atom still remains. All other metrics for assessing the quality of the model and the refinement are very good. We did not find any errors in the data processing; absorption correction was performed. The molecular structure is consistent with expectations based on spectral methods. We exclude the possibility of substitution of the copper atom by other metals in the complex based on other experimental data. In particular, complex **4** was characterized by NMR spectroscopy and powder XRD. During the synthesis, no other metals were used except potassium ion; however, potassium does not show any appreciable ability to competitively coordinate to the ligand, especially in this geometry.
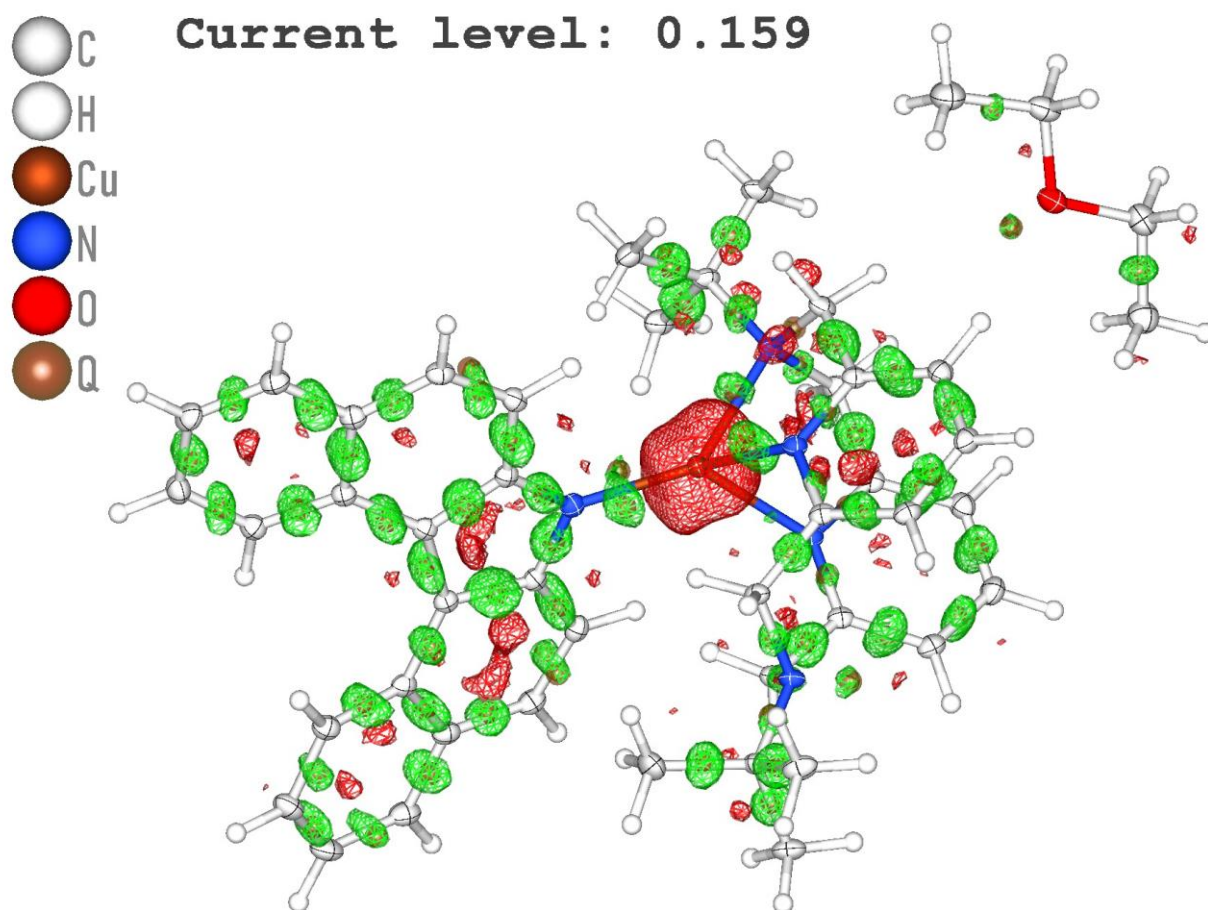
Figure S71. Positive (green) and negative (red) isosurfaces of residual electron density in the crystal of **κ³-4**.

Crystallographic data for 5.

$C_{35}H_{40}CuN_5O$, orange prism ($0.118 \times 0.053 \times 0.036$ mm³), formula weight 610.26 g mol⁻¹; monoclinic, $P2_1/n$ (No. 14), $a = 11.89392(7)$ Å, $b = 15.29071(8)$ Å, $c = 17.47129(10)$ Å, $\beta = 100.8255(6)°$, $V = 3120.89(3)$ Å³, $Z = 4$, $Z' = 1$, $T = 100(2)$ K, $d_{calc} = 1.299$ g cm⁻³, $\mu(Cu\ K\alpha) = 1.258$ mm⁻¹, $F(000) = 1288$; $T_{max}/T_{min} = 1.000/0.784$; 61537 reflections were collected ($3.872° \leq \theta \leq 79.764°$, index ranges: $-15 \leq h \leq 15$, $-19 \leq k \leq 19$, and $-22 \leq l \leq 21$), 6721 of which were unique, $R_{int} = 0.0466$, $R_\sigma = 0.0233$; completeness to θ of 79.764° 98.7 %. The refinement of 385 parameters with no restraints converged to $R1 = 0.0459$ and $wR2 = 0.1120$ for 6383 reflections with $I > 2\sigma(I)$ and $R1 = 0.0475$ and $wR2 = 0.1128$ for all data with goodness-of-fit $S = 1.093$ and residual electron density $\rho_{max}/\rho_{min} = 0.321/-0.906$ e Å⁻³, rms 0.064 e Å⁻³; max shift/e.s.d. in the last cycle 0.000.

Crystallographic data for 6.

$C_{34}H_{42}CuN_5$, red prism ($0.180 \times 0.158 \times 0.074$ mm³), formula weight 584.26 g mol⁻¹; orthorhombic, *Pbca* (No. 61), $a = 15.10177(5)$ Å, $b = 19.65119(7)$ Å, $c = 20.19471(9)$ Å, $V = 5993.14(4)$ Å³, $Z = 8$, $Z' = 1$, $T = 100(2)$ K, $d_{calc} = 1.295$ g cm⁻³, μ(Cu $K\alpha$) = 1.257 mm⁻¹, $F(000) = 2480$; $T_{max}/T_{min} = 1.000/0.580$; 93569 reflections were collected ($4.292° \leq \theta \leq 80.074°$, index ranges: $-19 \leq h \leq 19$, $-24 \leq k \leq 25$, and $-19 \leq l \leq 24$), 6463 of which were unique, $R_{int} = 0.0420$, $R_\sigma = 0.0179$; completeness to θ of 80.074° 98.7 %. The refinement of 367 parameters with no restraints converged to $R1 = 0.0335$ and $wR2 = 0.0896$ for 6281 reflections with $I > 2\sigma(I)$ and $R1 = 0.0344$ and $wR2 = 0.0902$ for all data with goodness-of-fit $S = 1.076$ and residual electron density $\rho_{max}/\rho_{min} = 0.358/{-}0.459$ e Å⁻³, rms 0.050 e Å⁻³; max shift/e.s.d. in the last cycle 0.000.

Crystallographic data for 8.

$C_{48}H_{32}Cu_4N_4$, yellow prism ($0.124 \times 0.108 \times 0.059$ mm³), formula weight 918.93 g mol⁻¹; triclinic, $P\overline{1}$ (No. 2), $a = 9.5755(2)$ Å, $b = 9.91553(16)$ Å, $c = 10.19785(18)$ Å, $\alpha = 89.3747(13)°$, $\beta = 75.0262(17)°$, $\gamma = 86.6760(15)°$, $V = 933.79(3)$ Å³, $Z = 1$, $Z' = 0.5$, $T = 100(2)$ K, $d_{calc} = 1.634$ g cm⁻³, μ(Cu $K\alpha$) = 2.882 mm⁻¹, $F(000) = 464$; $T_{max}/T_{min} = 1.000/0.828$; 16400 reflections were collected ($4.467° \leq \theta \leq 79.862°$, index ranges: $-12 \leq h \leq 12$, $-12 \leq k \leq 12$, and $-12 \leq l \leq 10$), 3941 of which were unique, $R_{int} = 0.0355$, $R_\sigma = 0.0292$; completeness to θ of 79.862° 96.9 %. The refinement of 253 parameters with no restraints converged to $R1 = 0.0343$ and $wR2 = 0.0952$ for 3745 reflections with $I > 2\sigma(I)$ and $R1 = 0.0355$ and $wR2 = 0.0962$ for all data with goodness-of-fit $S = 1.073$ and residual electron density $\rho_{max}/\rho_{min} = 0.563/{-}0.709$ e Å⁻³, rms 0.092 e Å⁻³; max shift/e.s.d. in the last cycle 0.001.

Crystallographic data for 9.

$C_{58}H_{52}Cl_4Cu_4N_4O_8$, colorless plank ($0.112 \times 0.048 \times 0.041$ mm³), formula weight 1328.99 g mol⁻¹; triclinic, $P\overline{1}$ (No. 2), $a = 10.2104(2)$ Å, $b = 10.7550(5)$ Å, $c = 13.3061(6)$ Å, $\alpha = 70.726(4)°$, $\beta = 79.185(3)°$, $\gamma = 79.171(3)°$, $V = 1342.23(10)$ Å³, $Z = 1$, $Z' = 0.5$, $T = 100(2)$ K, $d_{calc} = 1.644$ g cm⁻³, μ(Cu $K\alpha$) = 4.113 mm⁻¹, $F(000) = 676$; $T_{max}/T_{min} = 1.000/0.687$; 20416 reflections were collected ($3.552° \leq \theta \leq 79.928°$, index ranges: $-12 \leq h \leq 12$, $-10 \leq k \leq 13$, and $-16 \leq l \leq 16$), 5520 of which were unique, $R_{int} = 0.0355$, $R_\sigma = 0.0305$; completeness to θ of 79.928° 94.5 %. The refinement of 356

parameters with no restraints converged to $R1 = 0.0330$ and $wR2 = 0.0917$ for 5187 reflections with $I >$ $2\sigma(I)$ and $R1 = 0.0345$ and $wR2 = 0.0926$ for all data with goodness-of-fit $S = 1.116$ and residual electron density $\rho_{max}/\rho_{min} = 0.429/-0.743$ e Å^{-3}, rms 0.071 e Å^{-3}; max shift/e.s.d. in the last cycle 0.001.

Crystallographic data for 10.

Crystal Data. $C_{100}H_{88}Cu_4N_4O_5$, $M_r = 1679.90$, triclinic, P-1 (No. 2), a = 11.9543(4) Å, b = 12.2544(4) Å, c = 15.0509(5) Å, $\alpha = 99.545(3)^{\circ}$, $\beta = 104.493(3)^{\circ}$, $\gamma = 110.466(3)^{\circ}$, $V = 1920.36(12)$ Å^3, $T = 100$ K, $Z = 1$, $Z' = 0.5$, $\mu(CuK_\alpha) = 1.726$, 26828 reflections measured, 7989 unique ($R_{int} = 0.0831$) which were used in all calculations. The final wR_2 was 0.1773 (all data) and R_1 was 0.0728 (I≥2 σ(I)).

Detailed information about crystal structure determination can be accessed via supplementary cif files. Deposition numbers CCDC 2281130-2281133, 2283243-2283245 and 2295159-2295161 contain the supplementary crystallographic data for this paper. These data are provided free of charge by the joint Cambridge Crystallographic Data Centre and Fachinformationszentrum Karlsruhe Access Structures service www.ccdc.cam.ac.uk/structures.
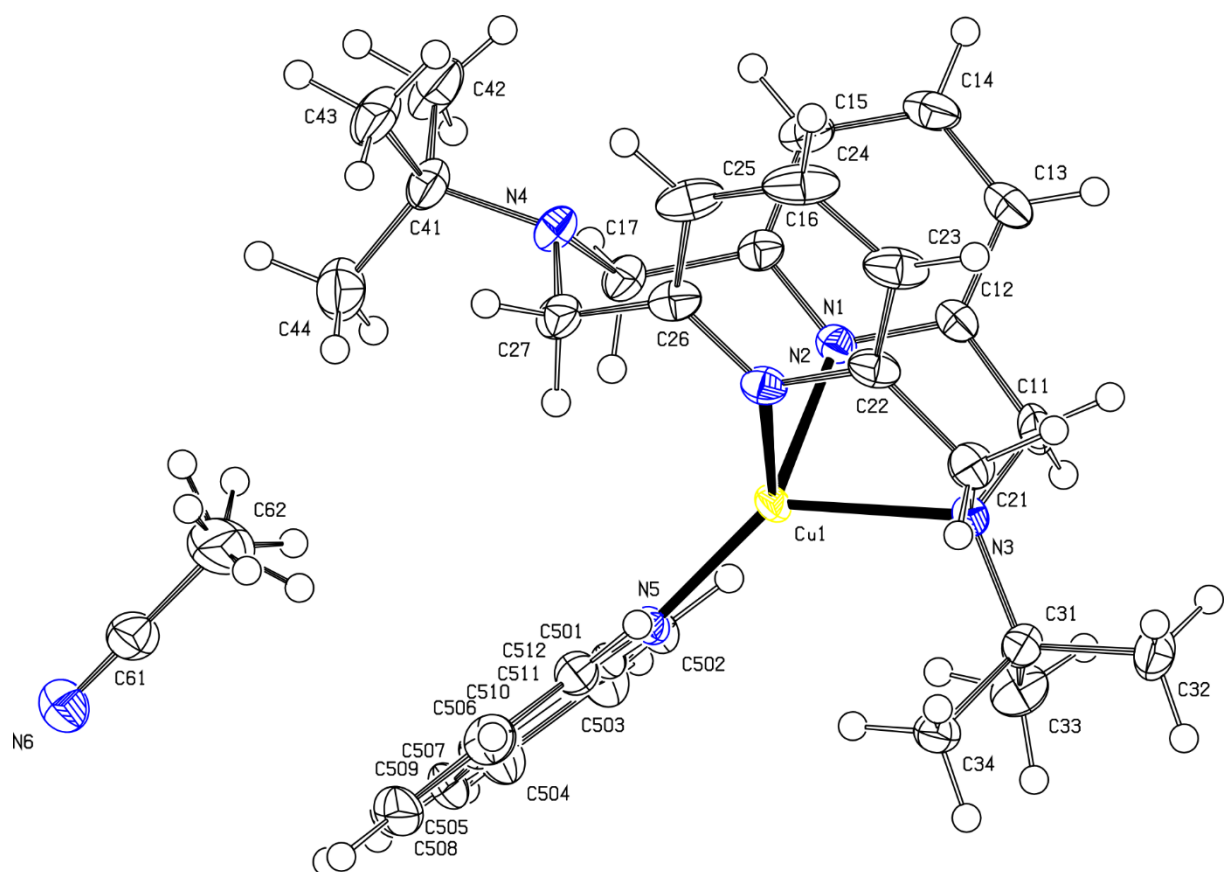
Figure S72. ORTEP at 50 % probability level of anisotropic displacement ellipsoids of non-hydrogen atoms for compound **1** according to SC-XRD data. Selected interatomic distances [Å]: Cu1–N1 2.0545(11), Cu1–N2 2.1071(11), Cu1–N3 2.2350(10), Cu1–N5 1.9103(10).
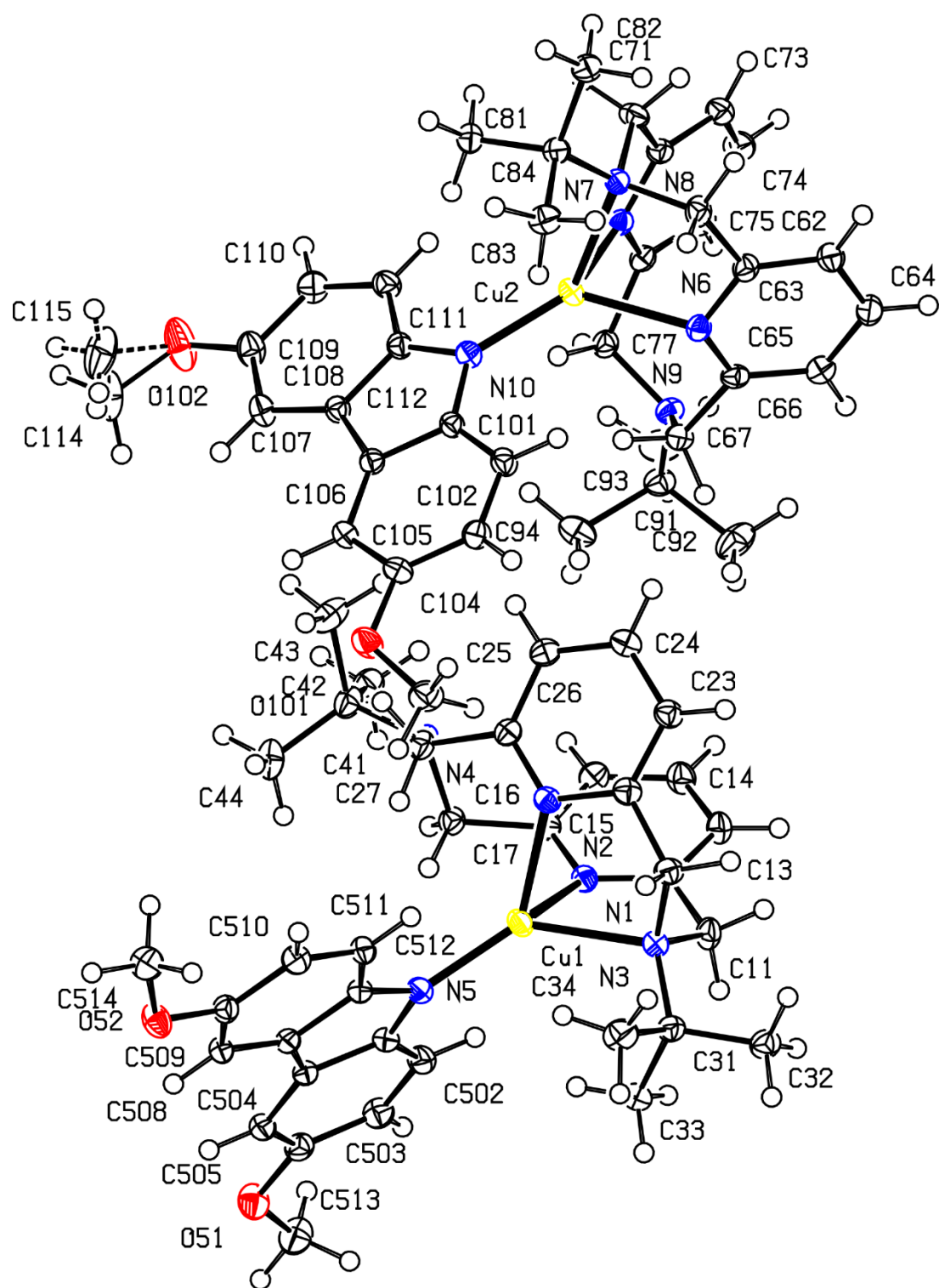
Figure S73. ORTEP at 50 % probability level of anisotropic displacement ellipsoids of non-hydrogen atoms for compound **2** according to SC-XRD data. Selected interatomic distances [Å]: Cu1–N1 2.1010(13), Cu1–N2 2.0952(13), Cu1–N3 2.2746(14), Cu1–N5 1.9150(13).
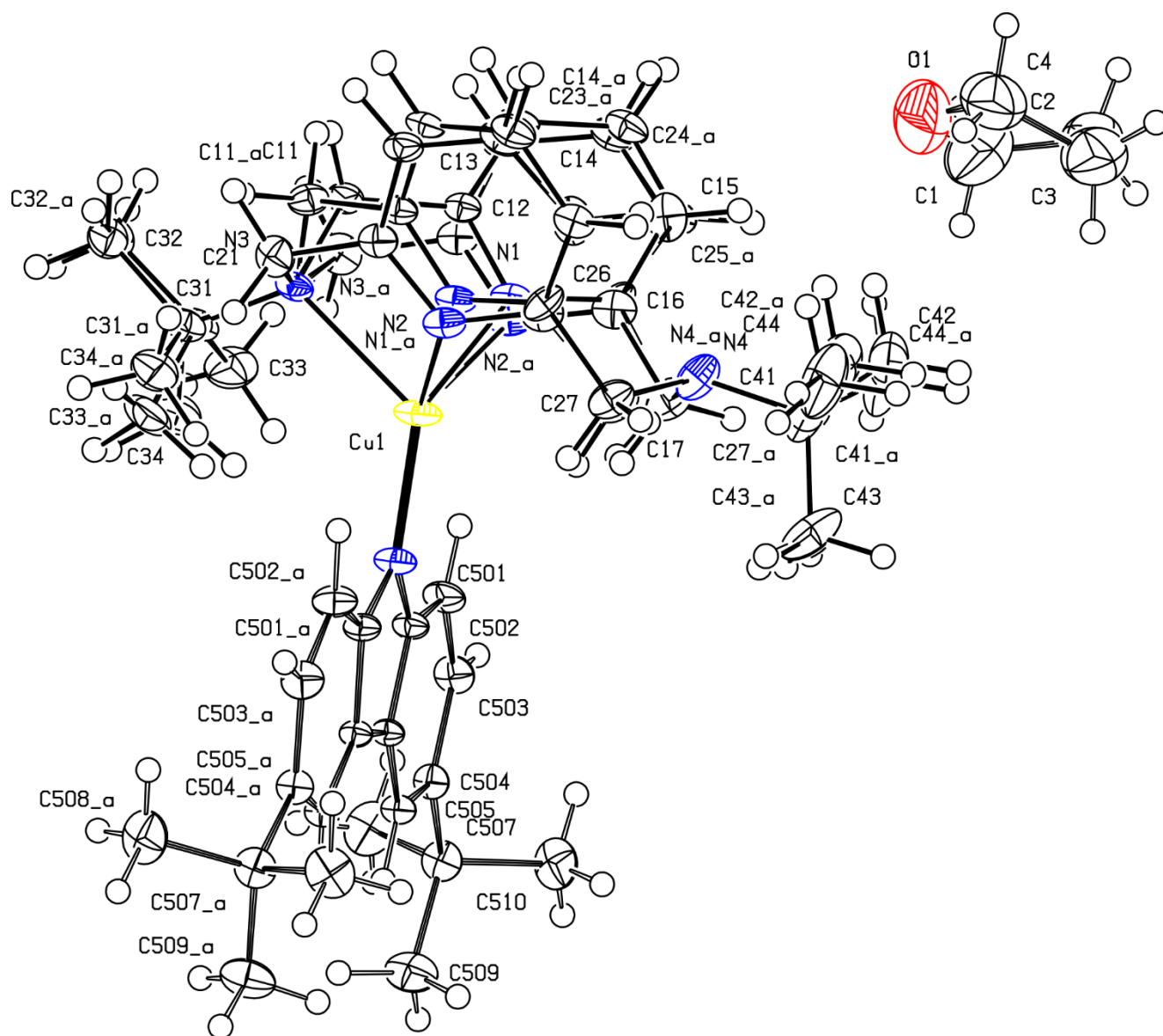
Figure S74. ORTEP at 50 % probability level of anisotropic displacement ellipsoids of non-hydrogen atoms for compound **3** according to SC-XRD data. Selected interatomic distances [Å]: Cu1–N1 2.112(5), Cu1–N2 2.059(6), Cu1–N3 2.290(3), Cu1–N5 1.9097(19).

Figure S75. ORTEP at 50 % probability level of anisotropic displacement ellipsoids of non-hydrogen atoms for compound κ^3-**4** according to SC-XRD data.

Figure S76. ORTEP at 50 % probability level of anisotropic displacement ellipsoids of non-hydrogen atoms for compound κ ^{3}-**4**-2 according to SC-XRD data. Hydrogen atoms are omitted for clarity.

Figure S77. ORTEP at 50 % probability level of anisotropic displacement ellipsoids of non-hydrogen atoms for compound κ^4-**4** according to SC-XRD data. Hydrogen atoms are omitted for clarity.
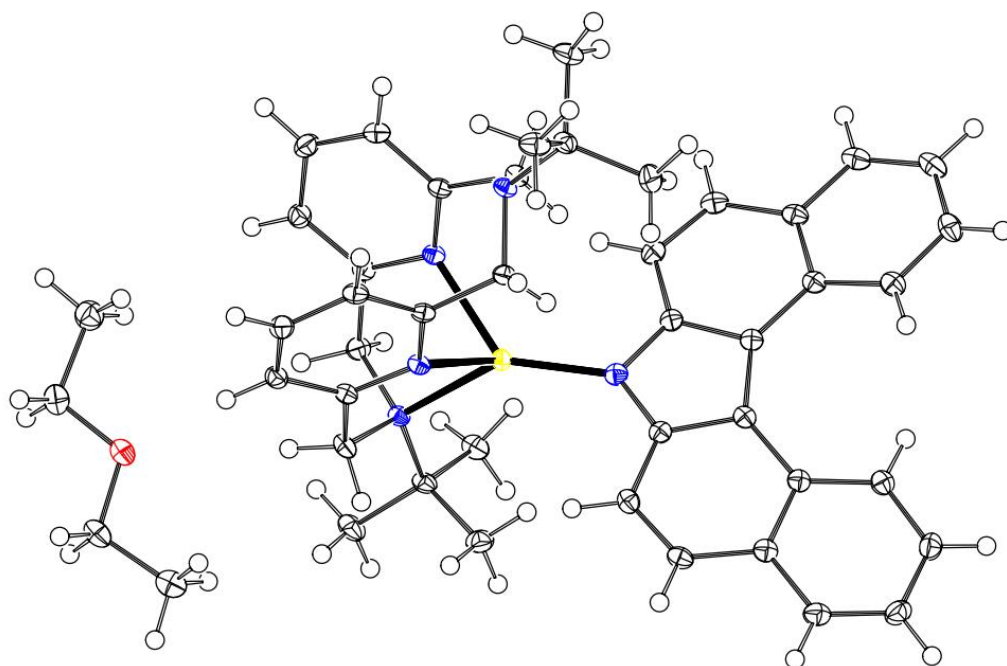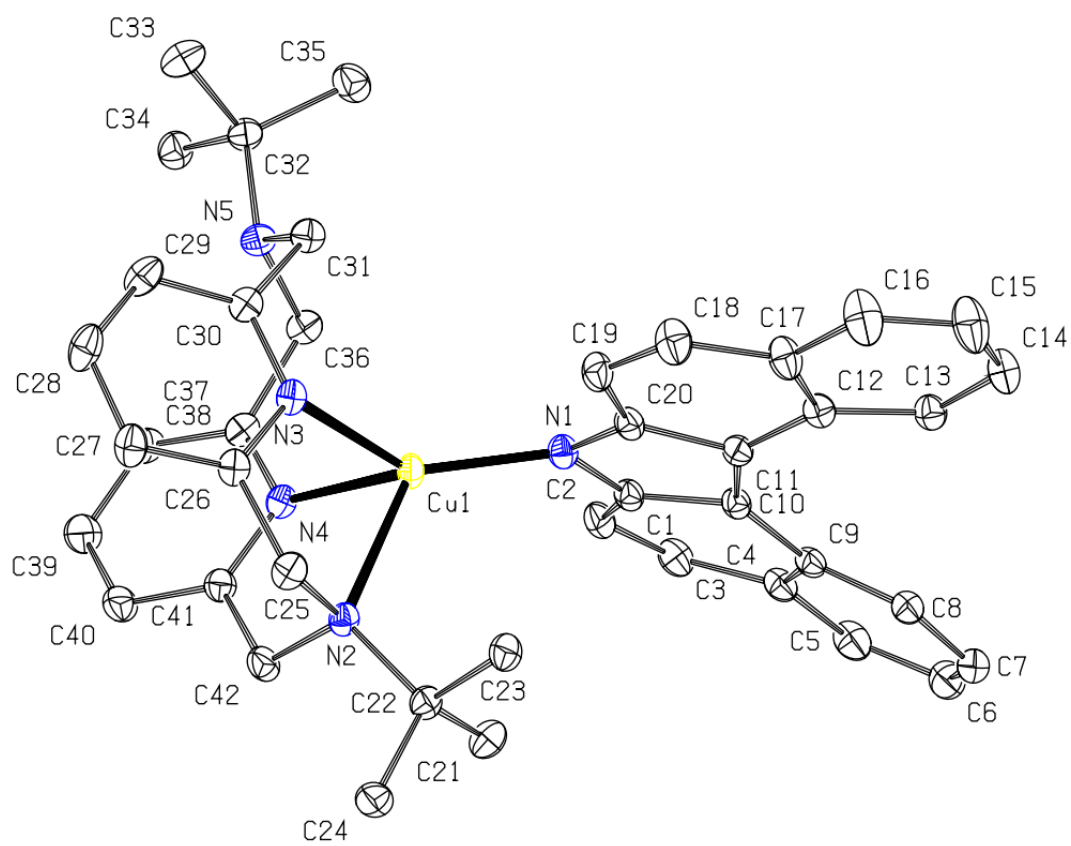
Figure S78. ORTEP at 50 % probability level of anisotropic displacement ellipsoids of non-hydrogen atoms for compound **5** according to SC-XRD data. Selected interatomic distances [Å]: Cu1–N1 2.1201(17), Cu1–N2 2.1462(18), Cu1–N3 2.1752(16), Cu1–N5 1.9532(16).
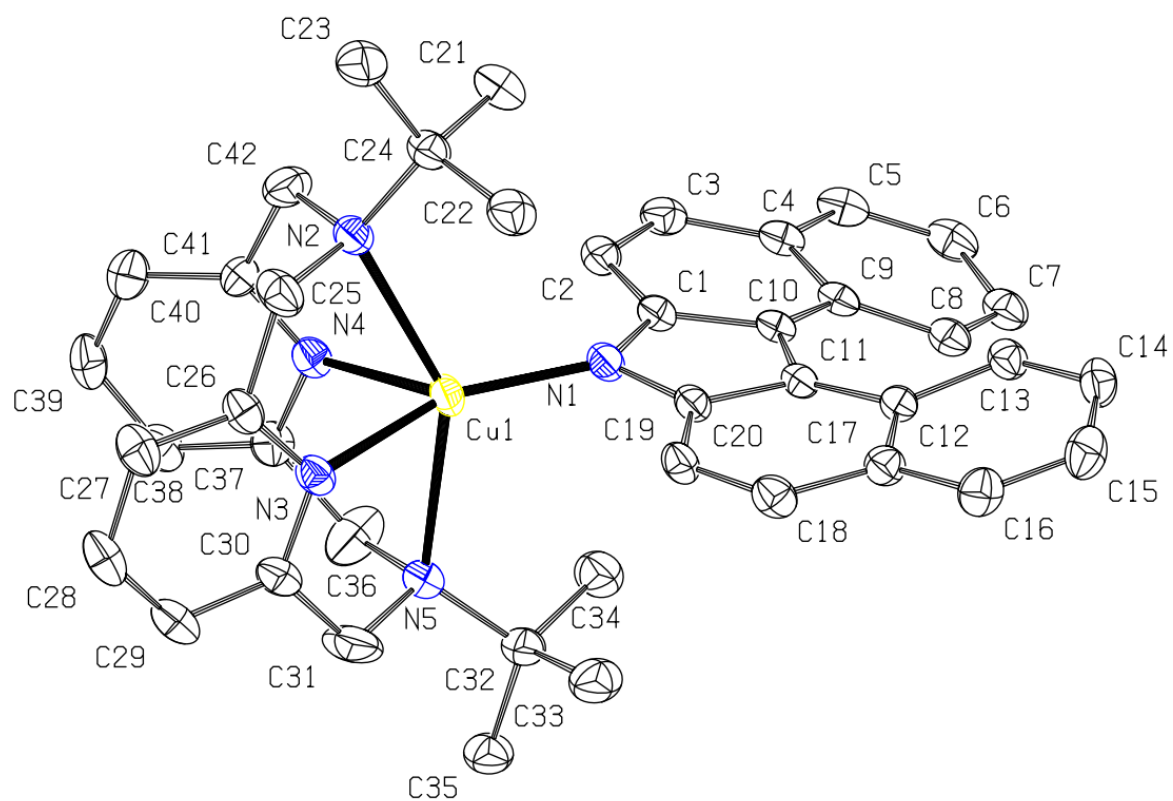
Figure S79. ORTEP at 50 % probability level of anisotropic displacement ellipsoids of non-hydrogen atoms for compound **6** according to SC-XRD data. Selected interatomic distances [Å]: Cu1–N1 2.1426(11), Cu1–N2 2.0827(11), Cu1–N3 2.2516(11), Cu1–N5 1.9373(11).
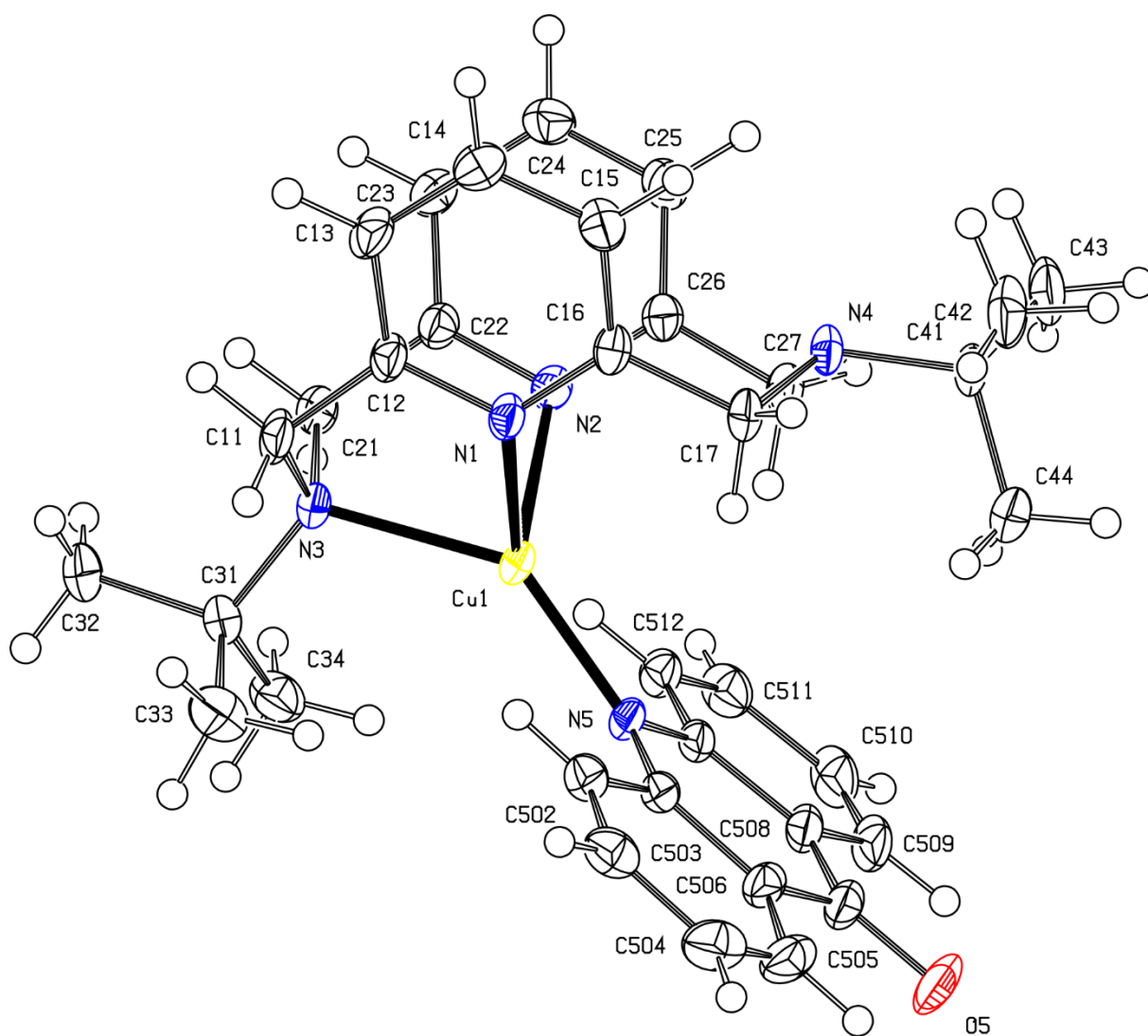
Figure S80. ORTEP at 50 % probability level of anisotropic displacement ellipsoids of non-hydrogen atoms for compound **8** according to SC-XRD data. Selected inte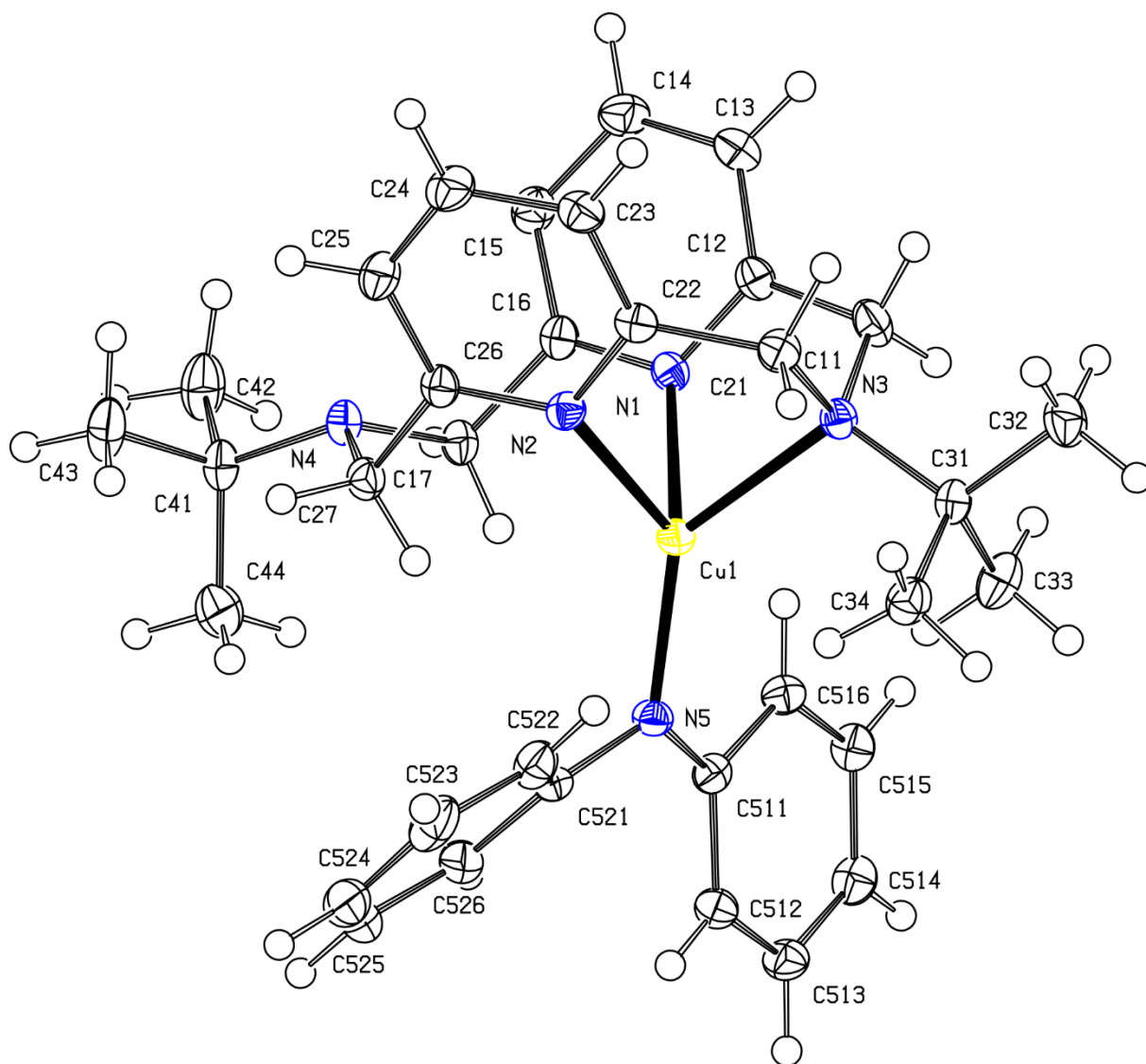ratomic distances [Å]: Cu1–Cu2 2.6643(4), Cu1–Cu2_a 2.6325(4), Cu1–N1 1.8899(17), Cu1–N2_a 1.9177(16), Cu2–N1 1.9141(17), Cu2–N2 1.8865(17).

Figure S81. ORTEP at 50 % probability level of anisotropic displacement ellipsoids of non-hydrogen atoms for compound **9** according to SC-XRD data. Selected interatomic distances [Å]: Cu1–Cu2 2.6831(4), Cu1–Cu2_a 2.6334(4), Cu1–N1 1.9032(17), Cu1–N2_a 1.9220(16), Cu2–N1 1.9062(17), Cu2– N2 1.8945(17).
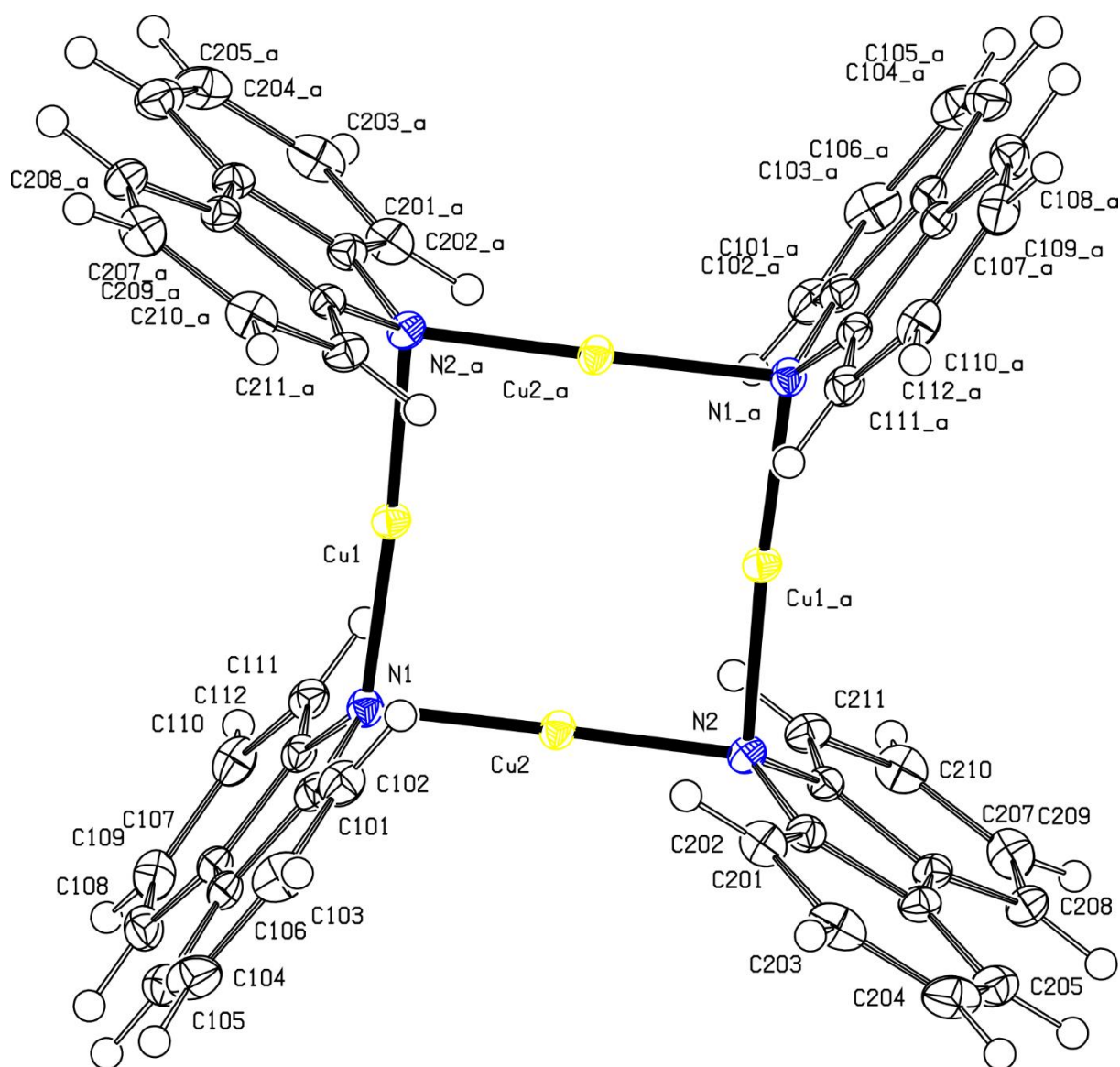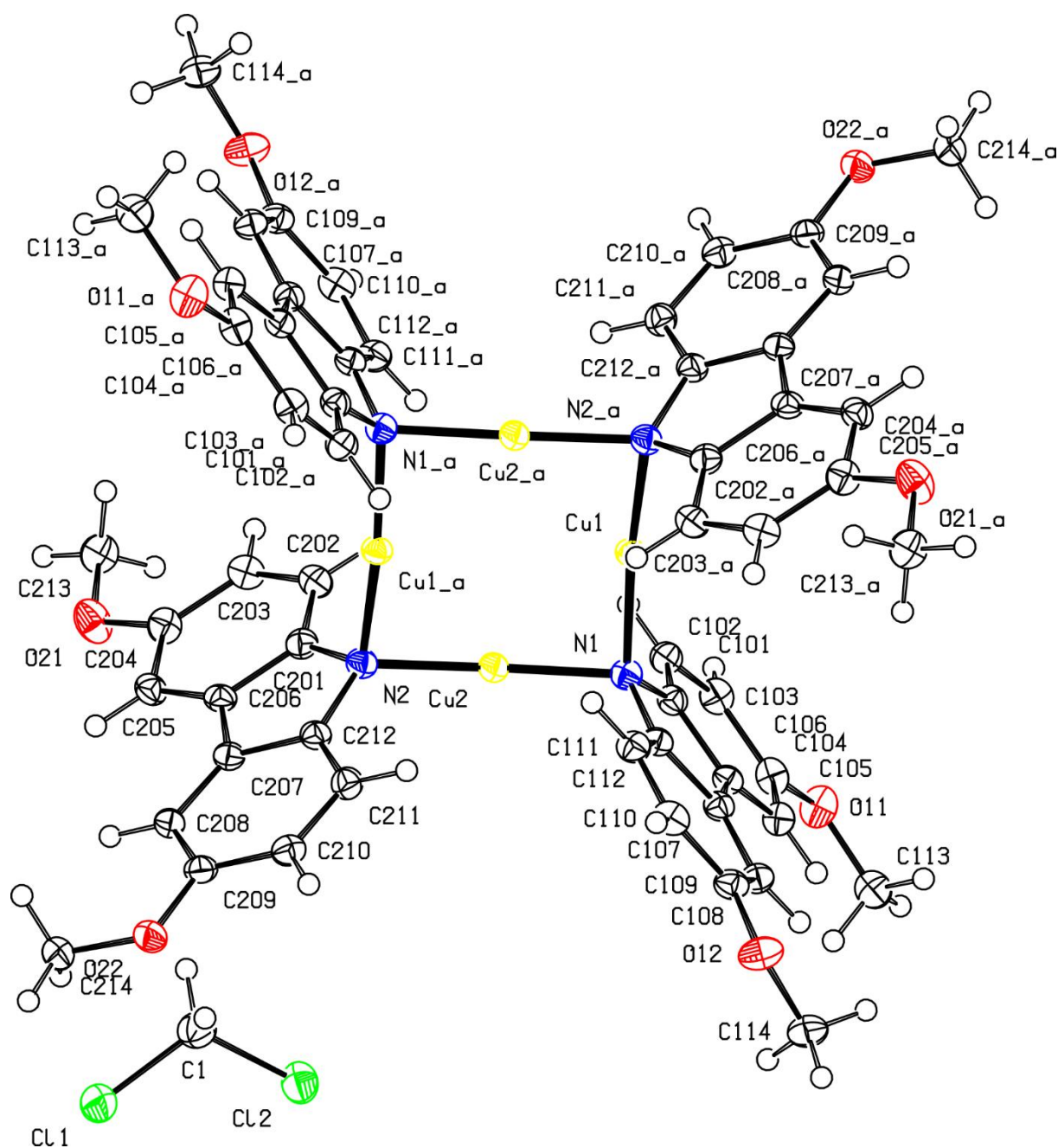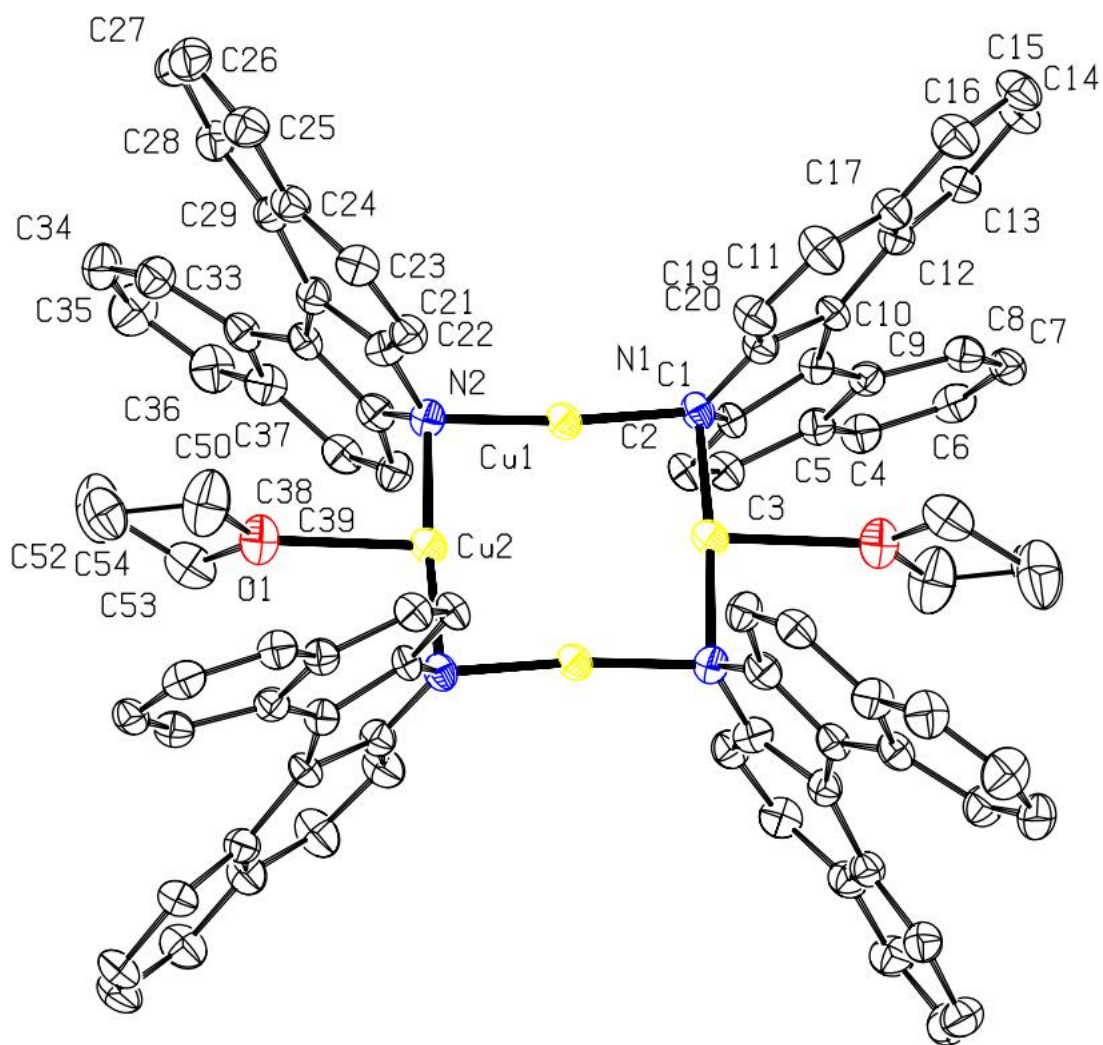
Figure S82. ORTEP at 50 % probability level of anisotropic displacement ellipsoids of non-hydrogen atoms for compound **10** according to SC-XRD data. Hydrogen atoms and non-coordinating THF molecules are omitted for clarity.

VIII. References

1.	A. Karimata, P. H. Patil, E. Khaskin, S. Lapointe, R. R. Fayzullin, P. Stampoulis and J. R. Khusnutdinova, *Chem Commun*, 2020, **56**, 50-53.
2.	C. A. Schneider, W. S. Rasband and K. W. Eliceiri, *Nat. Methods*, 2012, **9**, 671-675.
3.	A. Karimata, T. Gridneva, P. H. Patil, R. R. Fayzullin, E. Khaskin, S. Lapointe, A. Garcia-Roca and J. R. Khusnutdinova, *Dalton Trans.*, 2022, **51**, 13426-13434.
4.	P. H. Patil, G. A. Filonenko, S. Lapointe, R. R. Fayzullin and J. R. Khusnutdinova, *Inorg. Chem.*, 2018, **57**, 10009-10027.
5.	K.-A. Green and J. M. Hoover, *ACS Catal.*, 2020, **10**, 1769-1782.
6.	M. Håkansson, C. Lopes and S. Jagner, *Inorganica Chim. Acta*, 2000, **304**, 178-183.
7.	G. A. Filonenko, R. R. Fayzullin and J. R. Khusnutdinova, *J. Mat. Chem. C*, 2017, **5**, 1638-1645.
8.	J. R. Khusnutdinova, N. P. Rath and L. M. Mirica, *Inorg. Chem.*, 2014, **53**, 13112-13129.
9.	M. J. Frisch, G. W. Trucks, H. B. Schlegel, G. E. Scuseria, M. A. Robb, J. R. Cheeseman, G. Scalmani, V. Barone, G. A. Petersson, H. Nakatsuji, X. Li, M. Caricato, A. V. Marenich, J. Bloino, B. G. Janesko, R. Gomperts, B. Mennucci, H. P. Hratchian, J. V. Ortiz, A. F. Izmaylov, J. L. Sonnenberg, Williams, F. Ding, F. Lipparini, F. Egidi, J. Goings, B. Peng, A. Petrone, T. Henderson, D. Ranasinghe, V. G. Zakrzewski, J. Gao, N. Rega, G. Zheng, W. Liang, M. Hada, M. Ehara, K. Toyota, R. Fukuda, J. Hasegawa, M. Ishida, T. Nakajima, Y. Honda, O. Kitao, H. Nakai, T. Vreven, K. Throssell, J. A. Montgomery Jr., J. E. Peralta, F. Ogliaro, M. J. Bearpark, J. J. Heyd, E. N. Brothers, K. N. Kudin, V. N. Staroverov, T. A. Keith, R. Kobayashi, J. Normand, K. Raghavachari, A. P. Rendell, J. C. Burant, S. S. Iyengar, J. Tomasi, M. Cossi, J. M. Millam, M. Klene, C. Adamo, R. Cammi, J. W. Ochterski, R. L. Martin, K. Morokuma, O. Farkas, J. B. Foresman and D. J. Fox, Gaussian, Inc., Wallingford CT, 2016.
10.	J.-D. Chai and M. Head-Gordon, *Phys. Chem. Chem. Phys.*, 2008, **10**, 6615-6620.
11.	F. Weigend and R. Ahlrichs, *Chem. Chem. Phys.*, 2005, **7**, 3297-3305.
12.	F. Weigend, M. Häser, H. Patzelt and R. Ahlrichs, *Chem. Phys. Lett.*, 1998, **294**, 143-152.
13.	L. Skripnikov, Chemissian 4.67, 2020, https://www.chemissian.com.
14.	N. M. O'Boyle, A. L. Tenderholt and K. M. Langner, *J. Comp. Chem.*, 2008, **29**, 839-845.
15.	A. V. Marenich, C. J. Cramer and D. G. Truhlar, *J. Phys. Chem. B*, 2009, **113**, 6378-6396.
16.	G. M. Sheldrick, *Acta Crystallogr. A Found. Adv.*, 2015, **71**, 3-8.
17.	G. M. Sheldrick, *Acta Crystallogr. C Struct. Chem.*, 2015, **71**, 3-8.
18.	L. J. Farrugia, *J. Appl. Crystallogr.*, 2012, **45**, 849-854.
19.	O. V. Dolomanov, L. J. Bourhis, R. J. Gildea, J. A. K. Howard and H. Puschmann, *J. Appl. Crystallogr.*, 2009, **42**, 339-341.